

4. Superficial Clustering

4. Superficial Clustering	165
4.1 Introduction	167
4.2 Experimental Details	169
4.3 Structure and Morphology of the Platinum loaded on Titania nanopowders	172
4.3.1 General Approach to Sample Characterization	173
4.3.2 Morphology and Structure of TiO ₂ nanoparticles	175
4.3.3 Morphology and Structure of Pt nanoclusters	180
4.3.3.1 Grain Size related Cluster Morphology	180
4.3.3.2 Minority Structural Phases	197
4.3.3.3 Orientation Relationship between Pt clusters and Titania support	199
4.3.3.4 Platinum Macro-Agglomeration	207
4.3.4 Discussion about Nanostructural Results	209
4.3.4.1 Presence of the TiO ₂ Rutile Stable Phase	209

4.3.4.2 Effects of Grinding to Samples Structure _____	210
4.3.4.3 Platinum Clusters Morphology _____	211
4.3.4.4 Epitaxy in the Pt/TiO ₂ system _____	213
4.3.3.5 Metal Nanoclusters versus Macro-Agglomerated Clusters _____	215
4.4 Platinum Dispersion in Titania Samples _____	217
4.4.1 Mathematical Models and Statistical Parameters _____	217
4.4.1.1 Cuboctahedral Model Expressions _____	217
4.4.1.2 Spherical Model Expressions _____	222
4.4.1.3 Platinum Nanoclusters Mass Ratio Expressions _____	223
4.4.1.4 Cluster Dispersion Distribution Curves _____	225
4.4.2 Statistics on Experimental Results _____	227
4.4.2.1 Metal Cluster Dispersion with Thermal Treatment Temperature _____	227
4.4.2.2 Metal Cluster Dispersion with Platinum Loading Percentage _____	239
4.4.3 Discussion on Dispersion Analysis _____	247
4.4.3.1 Influence of the Thermal Treatment _____	247
4.4.3.2 Influence of the Metal Loading Percentage _____	248
4.4.3.3 Noble Metal Growing Modes on Semiconductor Oxide Support _____	251
4.4.3.4 Decrease of Platinum Mass Concentration vs. Nominal Value _____	253
4.5. Conclusions _____	255
References _____	258

4.1 Introduction

As commented in *Chapter 1*, another of the possible ways of metal distribution in SGS materials is the superficial clustering. In the present *Chapter* an extensively study of this phenomena is achieved.

In order to obtain the best knowledge on superficial metal clustering, it is necessary to analyze different aspects of the loading. The different characteristics can be divided in two main parts: On one hand the characteristics related to the nanostructure and morphology of the sample, such as the grain and cluster size, shape, epitaxial relations, structural phases, etc. Moreover, on the other hand, it will be also necessary to study those characteristics related with metal loading distribution, such as metal dispersion, nanocluster size distribution, superficial metal density. Furthermore, we will analyze the influence of the technological parameters in all these characteristics.

The *Chapter* is divided in three main parts. In the first one (*Section 4.3*), we take as a typical example of superficial metal clustering the platinum loaded on TiO₂ nanopowders. As we showed in recent works [1, 2], and as it will be described in the following, good Pt dispersions on TiO₂ surface have been obtained in a wide set of samples using the impregnation method. This part will become the nucleus of the *Chapter* being an extensive report of the Pt structure and morphology. In this way, we will carry out a rigorous *transmission electron microscopy* structural analysis of the samples.

The second part of the chapter (*Section 4.4*) has been devoted to achieve a complete statistical study of noble metal dispersion. We will use the experimental information obtained from HRTEM micrographs and ICP

in order to analyze the platinum distribution on titania nanopowders. Several statistical plots have been built up to describe samples distribution. Moreover, a semi-quantitative method has been used to obtain the platinum mass percent included in surface clusters with respect to TiO_2 total mass.

Finally in *Section 4.5* we will provide the main conclusions concerning the discussions performed in the precedent *Sections*.

4.2 Experimental Details

Two different methods have been followed to obtain our samples. Every method is a variation of so-called *impregnation method*, depending if the metal is introduced before or after stabilization of base material. The two methods will be briefly described in the following. In the schema showed below, we schematically present both method variations (*figure 4.1*),

In the first method (*set A*), Pt has been directly introduced to the nanostructured titanium oxide commercially available (Nanophase). Pt is introduced by means of platinum chloride impregnation, with nominal Pt/TiO₂ weight concentration ranging from 0.58 % to 5.80 % (1 to 10 % PtCl₄/TiO₂ weight concentration). After noble metal introduction, samples are treated thermally at different temperatures depending on the sample (700, 900 and 1100 °C) during 4 hours in synthetic air. As the obtained material is in an agglomerated state, a grinding process has been made to give homogeneity and uniformity to the layer, in order to have a good diffusion of gas molecules through the sensing layer. In our case, a Fristch Pulverisette 7 machine has been used.

The second set of samples (*set B*) has been obtained following the second variation of the impregnation method. In this case, the nanostructured titanium dioxide commercially available (Nanophase) is annealed at 900 °C during 4 hours to reach rutile stable phase. A grinding process is also applied to samples in order to obtain non-agglomerated material. At this point, a noble metal, Pt, is introduced by means of platinum chloride impregnation, with nominal Pt/TiO₂ weight concentration ranging from 0.58 % to 5.80 % (1 to 10 % PtCl₄/TiO₂ weight concentration). The resulting solution is dried to obtain the Pt-TiO₂ nanopowders. This Pt-modified titanium dioxide is then submitted to a thermal treatment ranging from 700 to 1100 °C, during 4 hours to get chemical stabilization in N₂ atmosphere.

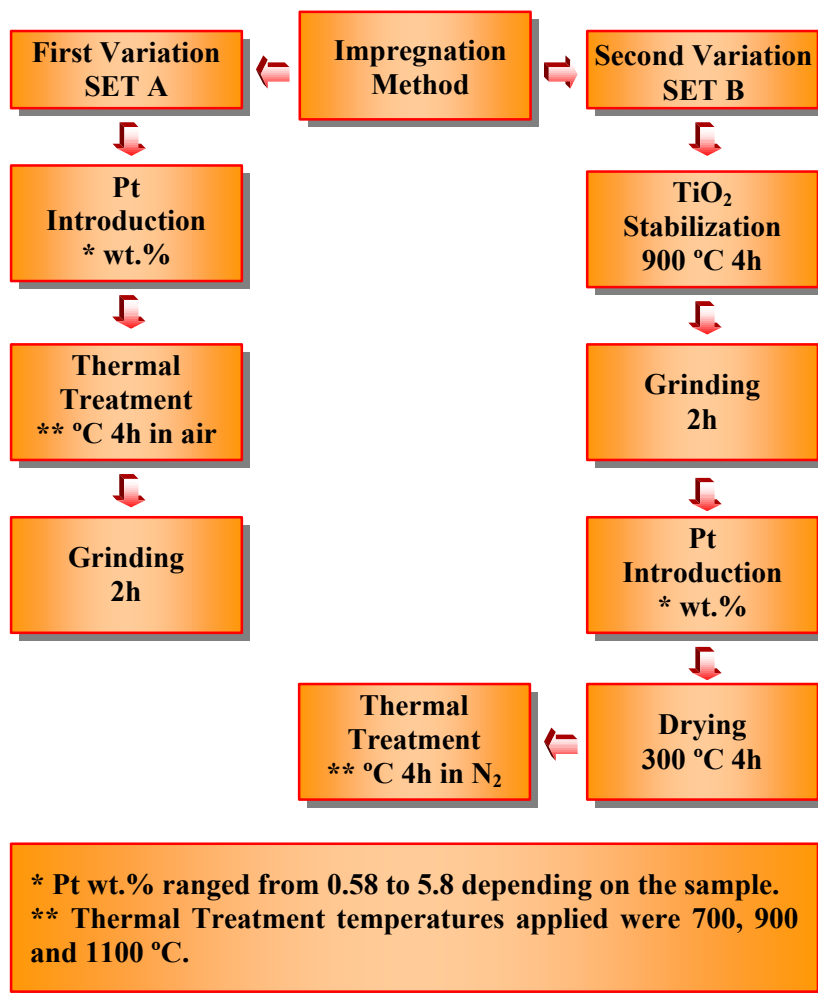


Figure 4.1. Schematic representation of the steps involved in sample preparation.

After this preparation we obtained two sets of samples. In every set we have studied the influence of Pt weight % concentration on material structure and the influence of the calcination temperature as well. Sample characteristics of both sets of samples are reported below (tables 4.1 and 4.2, respectively).

4. Superficial Clustering

Samples SET A	Pt wt. %	T _{treat} (°C)
A1	0.58	900
A2	2.90	900
A3	5.80	700
A4	5.80	900
A5	5.80	1100

Table 4.1 Sample characteristics *set A*

Samples SET B	Pt wt. %	T _{treat} (°C)
B1	0.58	900
B2	2.90	900
B3	5.80	700
B4	5.80	900
B5	5.80	1100

Table 4.2 Sample characteristics *set B*

Both structural (HRTEM and TEM) and chemical characterization techniques (ICP and EDS) have been used to analyze the sensing powders. A description of these techniques has been carried out in *Chapter 2*.

4.3 Structure and Morphology of the Platinum loaded on Titania nanopowders

The introduction of platinum as catalytic additive to the TiO₂ semiconductor support in order to improve its sensitivity and selectivity, and reduce the response time and its operating temperature has been reported in literature by several authors [3, 4, 5]. However, the sensing performance depends strongly on the additive dispersion characteristics: grain size, homogeneity of distribution and localization (superficial or volumic) [6, 7]. Although there exist many works in literature devoted to the electrical and general analytical characterization of these SGS materials just few works have been dedicated to the nanostructural characterization of Pt cluster's morphology in this SGS systems.

The aim of this section (4.3) was to make an extensive study of Pt nanoclusters morphology as well as of their dispersion on TiO₂ nanoparticles surface. First of all, we have analyzed our samples with spectroscopic techniques such as XRD or EDS in order to obtain a general characterization of the samples. Secondly, we have determined the TiO₂ structural characteristics, and afterwards, we have focussed our efforts in Pt nanoclusters morphology and possible phases. Digital image processing and Computer Image Simulation techniques (as described in *Chapter 2*) have been also applied in this section to facilitate results interpretation.

We will also report the influence of calcination temperature and Pt weight % concentration on material structure, catalytic metal distribution and mean size of both TiO₂ nanopowders and Pt nanoclusters after Pt introduction by impregnation method in TiO₂.

4.3.1 General Approach to Sample Characterization

In a first approach, XRD analysis has allowed us to obtain the structural composition of the nanopowders. In all our samples, we have found that XRD peaks show that TiO_2 is mainly in rutile phase while almost all Pt existing in the samples has metallic structure after the thermal treatment (see *figure 4.2* as an example of XRD spectra obtained in our samples).

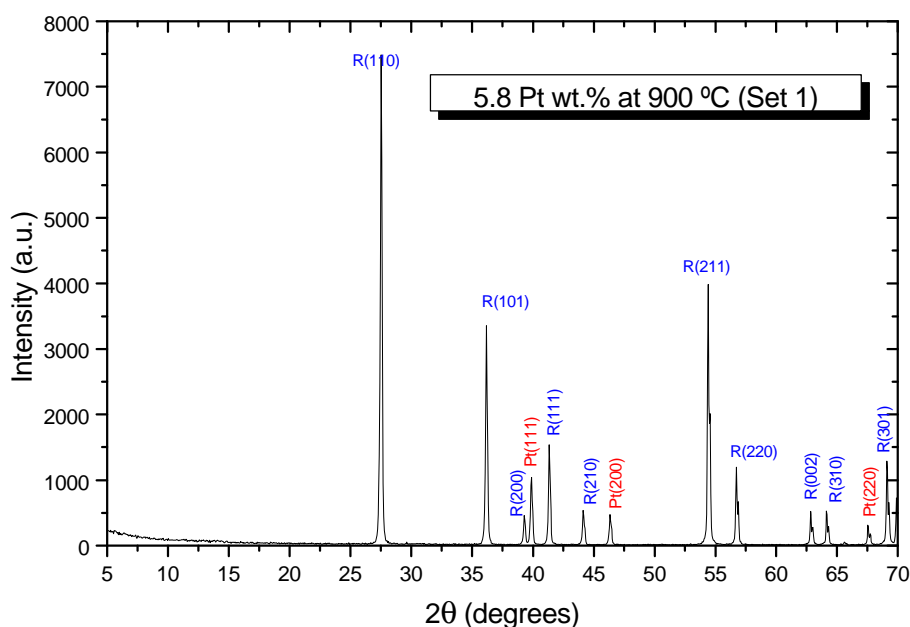


Figure 4.2. XRD spectrum of the *set B* sample with 5.8 Pt wt.% at 900 °C (*B4*). Peaks corresponding to the TiO_2 rutile phase are marked with the letter R and the ones corresponding to Pt metallic phase with Pt. In parenthesis we wrote the plane to which the peak is referred.

Moreover, results about the chemical composition of samples could be obtained by EDS analysis. In *figure 4.3*, we show the EDS spectrum of the 2.9 Pt wt.% sample from *set B* (*B2*). The presence of Ti and Pt is clearly shown, as well as the existence of Cu. The Cu peak appears in every spectra,

and it is due to the X-rays created on the borders of the copper sample grid (although we could minimize the peak size, we could never hide it). All samples present similar EDS spectra, with slight variations in the intensity of the Pt peak respect to the Ti one.

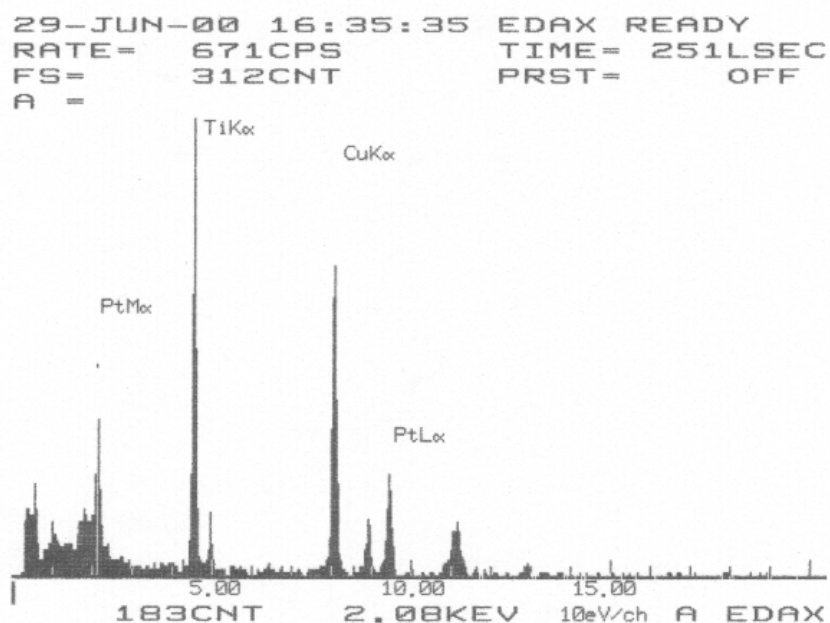


Figure 4.3. EDS spectrum of the *set B* sample with 2.9 Pt wt.% at 900 °C (*B2*). The presence of Ti and Pt on sample surface is evident. Cu peak is due to X-rays produced in the copper grid.

It is seen that a good statistical result of the structural composition is obtained from XRD analysis. Moreover, a compositional description of the sample can be obtained by EDS. Both techniques, as well as other spectroscopic techniques as XPS or RAMAN offer good resources in order to determine compositions, structures and atomic states, as they average the information subtracted from a big amount of material at the same time. However, no one of them is precise enough to deeply analyze the catalysts characteristics that can dramatically influence in gas sensing, such as particle and cluster size, cluster shape and faceting, catalyst dispersion and

4. Superficial Clustering

distribution, etc. In this way, we will need a more powerful tool, such as HRTEM, that allows us to reach the objectives and analyze in more detail the sample characteristics.

In the following, the structural and morphological characteristics of our samples will be studied by means of TEM and HRTEM related techniques.

4.3.2 Morphology and Structure of TiO₂ nanoparticles

A general characterization of samples obtained by methods *A* and *B* has revealed that although in both samples, TiO₂ particles have nanometric sizes, there is a slight difference between their morphology.

TiO₂ particles from a *set A* sample are shown in *figure 4.4*. Nanoparticle shapes are not well defined and particles present irregular borders. In few words, we can assume that TiO₂ nanoparticles obtained following the first method look like "smashed" (*figure 4.4*). These TiO₂ nanoparticles show a strong evidence of grinding effects. However, samples corresponding to the second set (*set B*) do not show the grinding effects (*figure 4.5*). On the contrary, these TiO₂ nanoparticles (*set B* nanopowders) have got defined shapes (quasi-spherical) and their borders are clearly visible at low magnification (see an example in *figure 4.5*). The difference in nanoparticles morphology between both sets of samples can be explained because in the second set the thermal treatment is applied after grinding, leading to a recrystallization of TiO₂ nanoparticles. These recrystallized particles acquire quasi-spherical shapes. In the following, we will assume TiO₂ grains as spherical particles (for samples corresponding to *set B*), in order to carry out the statistics developed in *section 4.4.2*. This assumption could be achieved after TEM micrograph observation. The low agglomeration of the nanoparticles visualized in small-magnified micrographs as well as the particle reduced size, is a great advantage for the posterior properties of the SGS devices implemented.

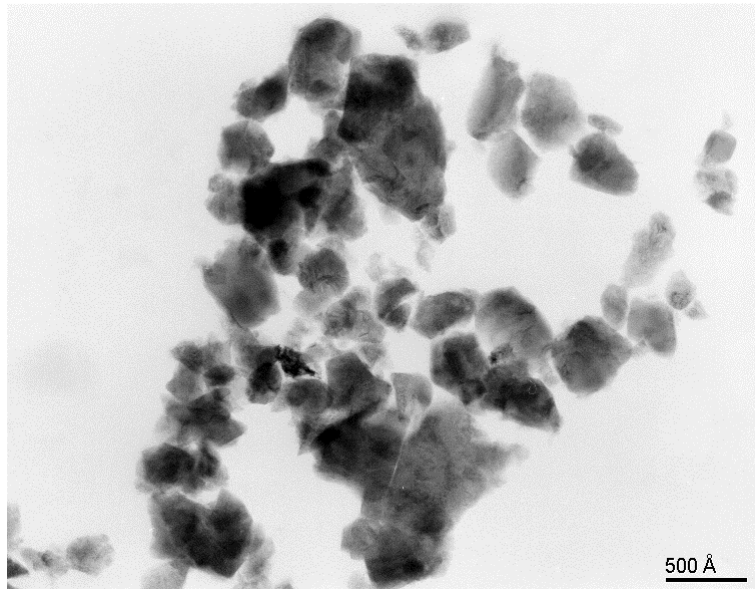


Figure 4.4. TiO₂ nanoparticles of the *set A* sample with 2.9 Pt wt. % (*A2*), submitted to a temperature treatment of 900 °C (First preparation method).

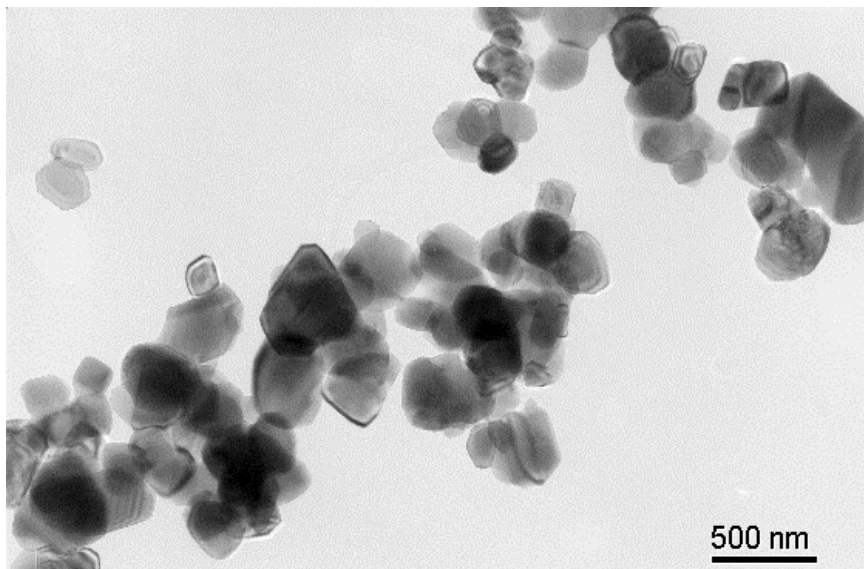


Figure 4.5. TiO₂ nanoparticles of the *set B* sample with 5.8 Pt wt. % (*B4*), submitted to a temperature treatment of 900 °C (Second preparation method).

4. Superficial Clustering

The general aspect of samples found in TEM micrographs needs a more detailed analysis. We obtained HRTEM micrographs of all samples in order to understand the general morphological changes observed above. As we pointed out before, samples from both sets were submitted to thermal treatments up to reach the rutile stable phase. The structural analysis made through HRTEM confirms that TiO_2 rutile phase is present in all samples (as

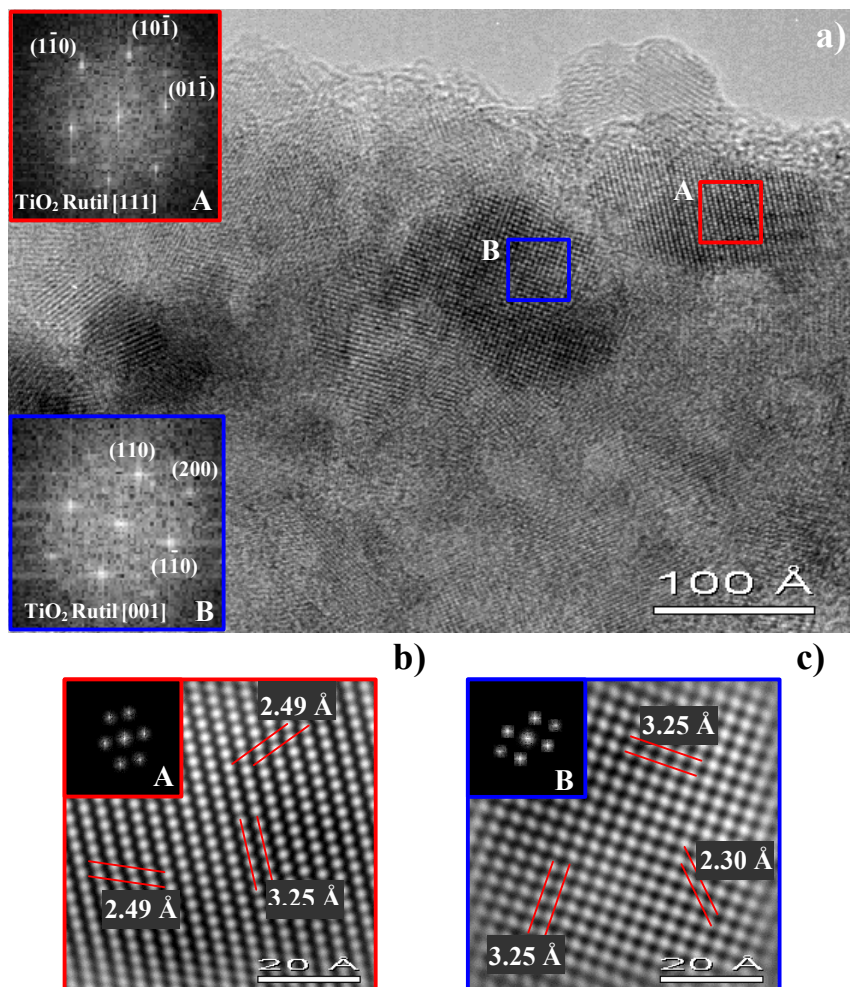


Figure 4.6. a) HRTEM micrograph for the *set A* sample with 5.8 Pt wt.% (A4). Each TiO_2 particle is composed of several nanocrystals, each one differently oriented. Example A (in red) was found in the zone axis [111], while example B (in blue) was in the [001], as shown in the respective digital diffractograms inserted. b) and c) correspond to the filtered images.

shown in *figures 4.6 and 4.7*). Anatase phase nanoparticles are rarely found in HRTEM micrographs, being their percentage lower than 1%. This result shows that the thermal treatment was highly effective. Even though TiO_2 rutile phase is the dominant in both samples, the disposition of rutile crystals is different. In samples from *set A*, the smashed structures viewed in low magnification TEM micrographs result in particles formed of several nanocrystals when imaging under HRTEM conditions. We find different rutile orientations in each particle, denoting that original TiO_2 nanoparticles have been broken during grinding, and the broken pieces acquired the orientations showed (*figure 4.6*). However, particles from *set B* samples show a unique orientation in the whole nanoparticle. It means that the nanoparticles in *set B* samples are compact particles and not the composition of several crystals.

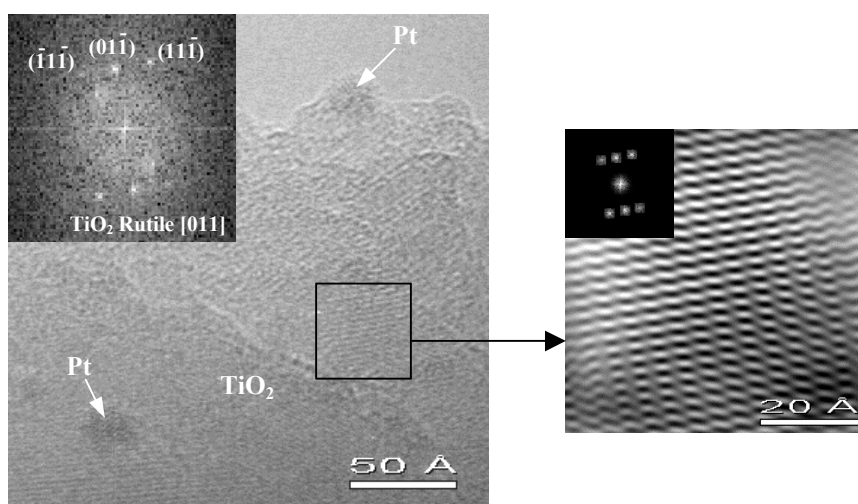


Figure 4.7. HRTEM micrograph for the *set B* sample with 5.8 Pt wt.% (*B4*). There are Pt clusters embedded on TiO_2 surface. TiO_2 structure is rutile and it is oriented in the zone axis [011]. On the right side, we show the corresponding filtered image.

TiO_2 structure is rutile in both samples, as found after indexing the digital diffractograms (FFT) of different areas from each image. In *figure 4.6*, we find that the two regions studied presented different orientation, suggesting that are composed of different crystals. Orientations found

4. Superficial Clustering

correspond to [111] and [001] zone axis, respectively. These crystals could be small pieces of a particle broken during grinding process. In *figure 4.7*, the TiO₂ grain imaged is oriented in the [011] direction. In this case the whole TiO₂ nanoparticle has the same orientation. Atomic columns can be clearly seen after image filtering (using a mask on FFT), as shown also in *figures 4.6* and *4.7*. Some other grain orientations can be also observed in other particles but these will be analyzed in more detail in next section as a whole with Pt clusters. In order to determine the orientations of the TiO₂ rutile particles we have calculated using the *EJEZ* software the relationship between angles and plane distances for several zone axes. In *table 4.3* we show the results obtained for the most common orientations found.

Plane 1	Plane 2	D1 (Å)	D2 (Å)	Angle	Zone Axis
(200)	(110)	2.30	3.25	45.0 °	[001]
(1-10)	(110)	3.25	3.25	90.0 °	[001]
(01-1)	(10-1)	2.49	2.49	45.0 °	[111]
(1-10)	(10-1)	3.25	2.49	67.5 °	[111]
(11-1)	(01-1)	2.19	2.49	28.4 °	[011]
(11-1)	(11-1)	2.19	2.19	56.9 °	[011]
(11-1)	(200)	2.19	2.30	61.6 °	[011]
(01-1)	(200)	2.49	2.30	90.0 °	[011]
(2-10)	(10-1)	2.05	2.49	61.0 °	[121]
(2-10)	(1-11)	2.05	2.19	50.3 °	[121]

Table 4.3. Angle and distance plane relationship for TiO₂ rutile phase.

Morphological and structural results found for TiO₂ nanoparticles in samples corresponding to the same *set* are similar, thus in this *section* we won't extend so much in particular descriptions and we just have given a characteristic example in every case. In *section 4.4* a further examination about TiO₂ grain size variation will be made.

Some Pt nanoclusters can be found on TiO₂ surface in the case of samples from *set B*. The large quantity of crystal orientations present in the

example showed for *set A* (*figure 4.6*) makes difficult to find the platinum clusters in this case. In the following, we will focus our efforts in the analysis of Pt morphology and structure.

4.3.3 Morphology and Structure of Pt nanoclusters

4.3.3.1 Grain Size related Cluster Morphology

Cuboctahedral Nanoclusters ($d < 3\text{nm}$)

HRTEM analysis of the samples has been carried out in order to find the structural morphology of our samples. In *table 4.4* we summarize the distances and angles between platinum planes that can be resolved by HRTEM because of the resolution limit of our equipment.

Plane 1	Plane 2	D1 (Å)	D2 (Å)	Angle	Zone Axis
(200)	(020)	1.96	1.96	90.0 °	[001]
(1-11)	(11-1)	2.27	2.27	70.5 °	[011]
(200)	(11-1)	1.96	2.27	54.7 °	[011]

Table 4.4. Angle and distance plane relationship for Pt metallic phase.

In *figure 4.8* (corresponding to sample *A2*), we show the formation of Pt clusters, in dark contrast, on the TiO₂ nanoparticles surface. The study of the digital diffractogram shows that the Pt forming the clusters is in metallic phase. The Pt region visualized is oriented following the [011] direction, and shows perfectly the {200} and {111} family planes. These clusters acquire quasi-spherical shapes when they have sizes bigger than 3 nm in diameter. For smaller diameter sizes, these clusters present facets that have to be studied carefully. As shown in *figure 4.8*, Pt nanoclusters distribution on TiO₂ samples from *set B* is not homogeneous. This

4. Superficial Clustering

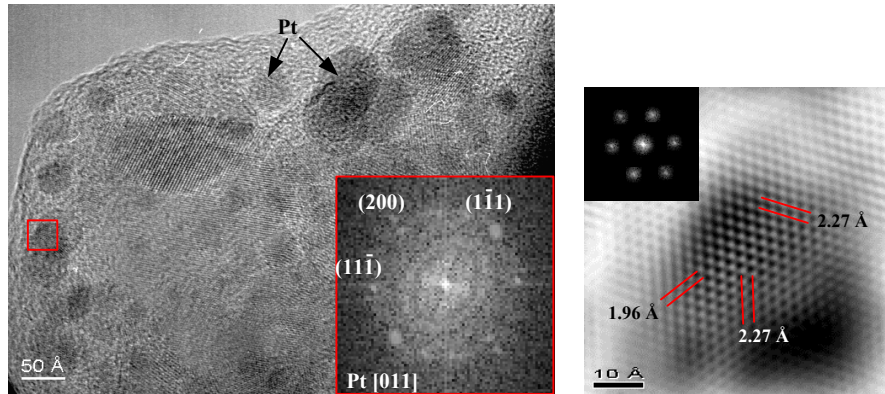


Figure 4.8. HRTEM micrograph for the *set A* sample with 2.9 Pt wt.% (*A2*). We have determined that dark contrast shapes correspond to Pt clusters in metallic phase. Pt clusters acquired big sizes, up to 7.5 nm. Notice that for sizes bigger than 3 nm Pt clusters tend to be spherical. DIP was applied to an image region.

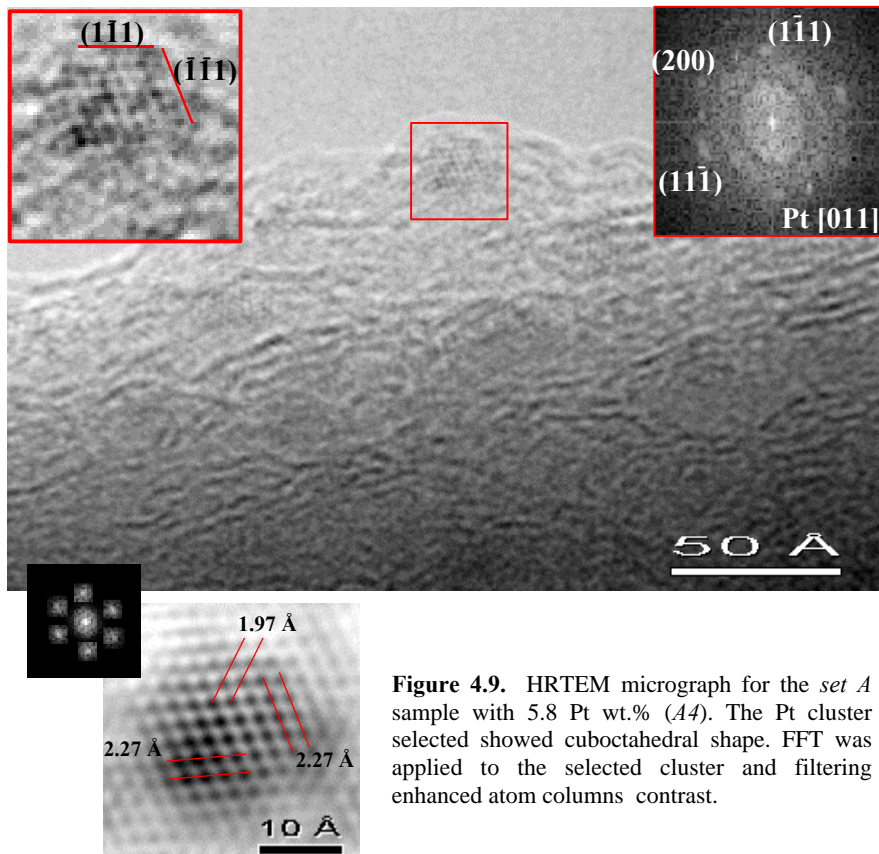


Figure 4.9. HRTEM micrograph for the *set A* sample with 5.8 Pt wt.% (*A4*). The Pt cluster selected showed cuboctahedral shape. FFT was applied to the selected cluster and filtering enhanced atom columns contrast.

characteristic as well as the non-definition on the TiO_2 nanograins shape makes difficult the statistical study of this kind of samples.

Nevertheless, due to the small size of the TiO_2 crystals, this set of samples has been very useful in order to study the morphology of the small Pt clusters (less than 3 nm in diameter). The low thickness of support crystals has allowed us to obtain better contrast when imaging the Pt nanoclusters. As shown in *figure 4.9* (sample *A4*), the Pt nanocluster imaged has a square projected shape faceted on (111) planes. This result is in good agreement with the projection expected for a cuboctahedral cluster imaged in the [011] zone axis.

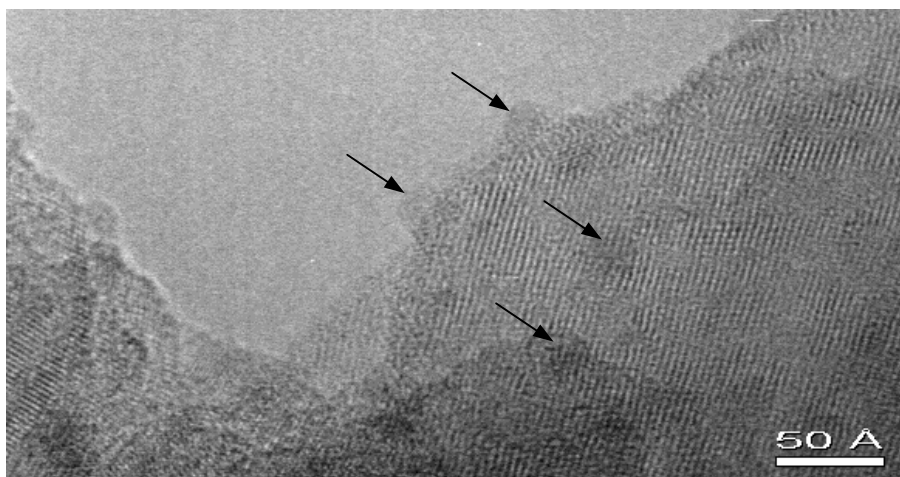


Figure 4.10. HRTEM micrograph for the *set A* sample with 5.8 Pt wt.% treated at 1100 °C (*A5*). Pt nanoclusters are marked with black arrows.

The HRTEM micrographs corresponding to sample *A5* show a wide variety of Pt nanoclusters disposition. Several clusters embedded on TiO_2 surface are shown in *figure 4.10*. These clusters have diameter sizes in the range 1-3 nm. In *figure 4.11*, we have submitted to a careful analysis the Pt cluster selected. As showed in the amplified picture, both, TiO_2 support and Pt planes interfere in the image. The digital diffractogram of the selected area gives us the information about both materials planes. However, after a detailed mask filtering we can separate both data, and obtain Pt and TiO_2 planes separately. In this case, the exact shape of the Pt cluster remains a bit

4. Superficial Clustering

diffuse, due to the interaction of the electrons with the support. Anyway, we can observe its faceted morphology in the (111) planes. The CIS of the system give us a good idea of the real metal cluster morphology. In the following, we tried two possibilities. In a first attempt, we supposed the particle as a 309-atom cuboctahedron truncated on its basis (*figure 4.12*). We took as epitaxial interfaces those perpendicular to the experimental image zone axis. The experimental HRTEM image is compared with the simulated model in *figures 4.12c* and *4.12.d* respectively. In the second attempt, we

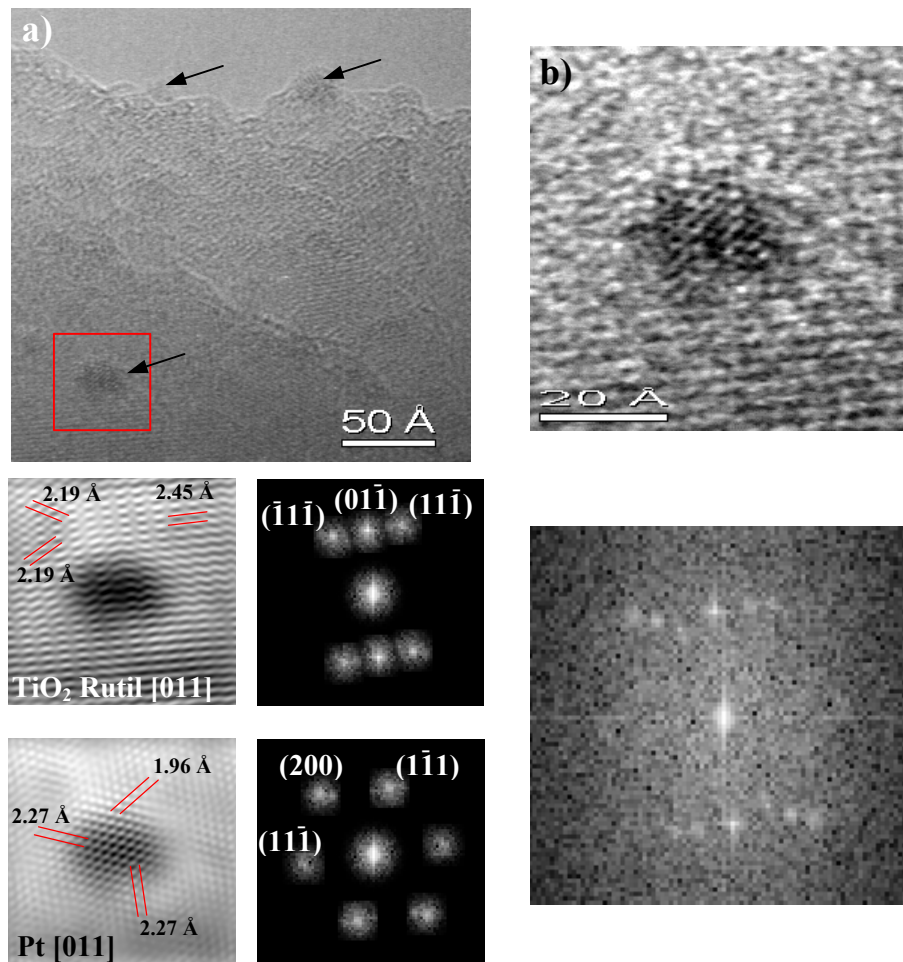


Figure 4.11. a) HRTEM micrograph and selected area DIP, for the *set A* sample with 5.8 Pt wt.% treated at 1100 °C (*A5*). b) Pt nanocluster on [011] orientation is placed on TiO₂ rutile particle also oriented on the [011] zone axis.

take the same epitaxial relationship as before, but assuming the cluster as a sphere (with a radius of 12 Å) and truncated in its basis (*figure 4.13*). The comparison between the simulated and experimental images has a good resemblance in both cases. It is difficult to decide a priori which one of the two examples corresponds to the real morphology of the particle analyzed. However, if we compare both examples accurately, we can observe slight differences in the borders of the simulated clusters. In the case of the cuboctahedron, the borders of the clusters are more diffuse in the simulated image than in the case of the sphere. This is due to the lower thickness of the

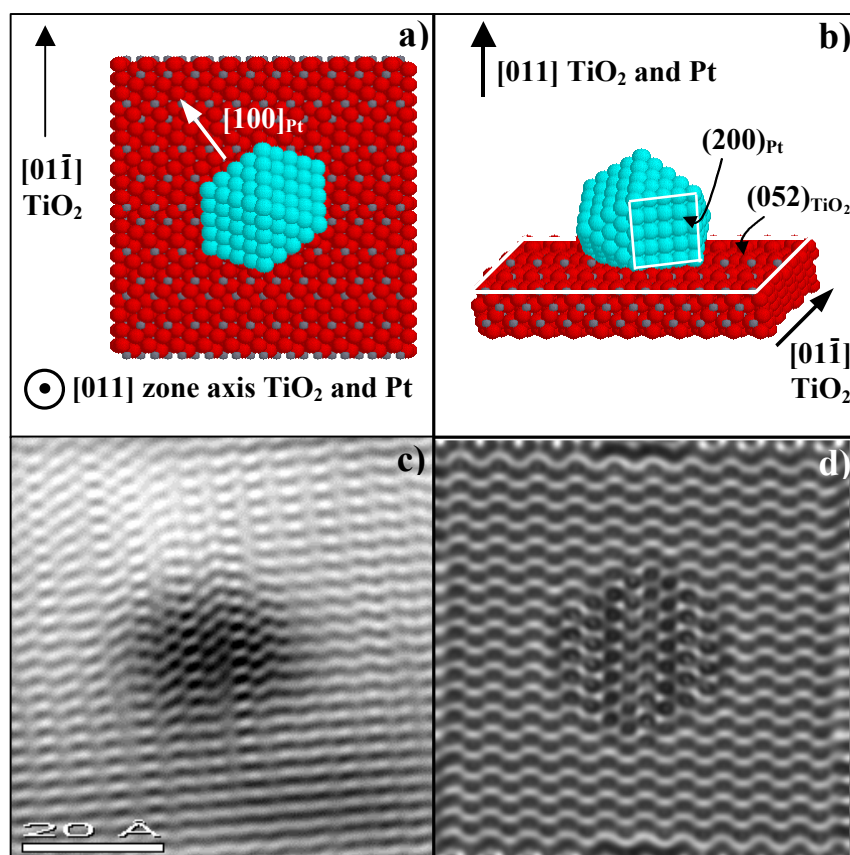


Figure 4.12.a-b. Supercell model for the Pt cluster showed in *figure 4.11*. A cuboctahedral model has been considered for platinum cluster morphology. The images behind correspond to the cluster-support system obtained experimentally (after noise filtering) (**c**) and to the computer simulation from the model presented above (**d**). Support thickness chosen for computer simulation had a value of 48 Å.

4. Superficial Clustering

projected borders for the cuboctahedron compared with the sphere. This effect can be explained by means of a stronger faceting in the cuboctahedron. As in the experimental image the borders appear also slightly diffused, we can assume that the best agreement between simulated and experimental images corresponds to the cuboctahedral model.

Another example is shown in *figure 4.14*. In this case, the Pt nanocluster selected is oriented in the $[001]$ zone axis. The projection shows a square shape, in good agreement with the projected shape of a cuboctahedral nanoparticle oriented in the $[001]$ direction. The image has

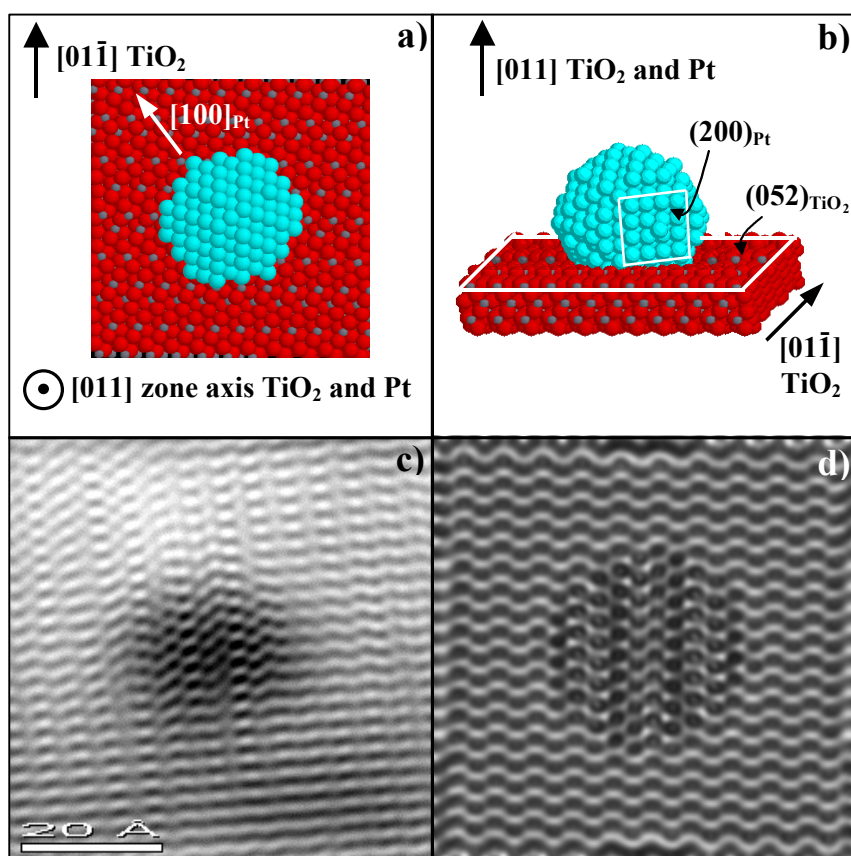


Figure 4.13.a-b. Supercell model for the Pt cluster showed in *figure 4.11*. **c)** Cluster-support system obtained experimentally (after noise filtering) and **d)** the computer simulation from the model presented in **(a-b)**, in this case a Pt spherical model has been considered. Support thickness chosen for computer simulation had a value of 48 Å.

been processed digitally, separating Pt frequency data from those corresponding to TiO_2 . We find that the [001] oriented Pt cluster is embedded on a TiO_2 support approximately placed in the [211] zone axis. We have also carried out CIS to confirm the results obtained (*figure 4.15*). After few attempts, we found the supercell model that suited better to the experimental image (*figure 4.15*). The model presented corresponds to a 309-atoms cuboctahedral Pt cluster in the [001] zone axis, supported on a TiO_2 rutile substrate 16° out of [211] direction.

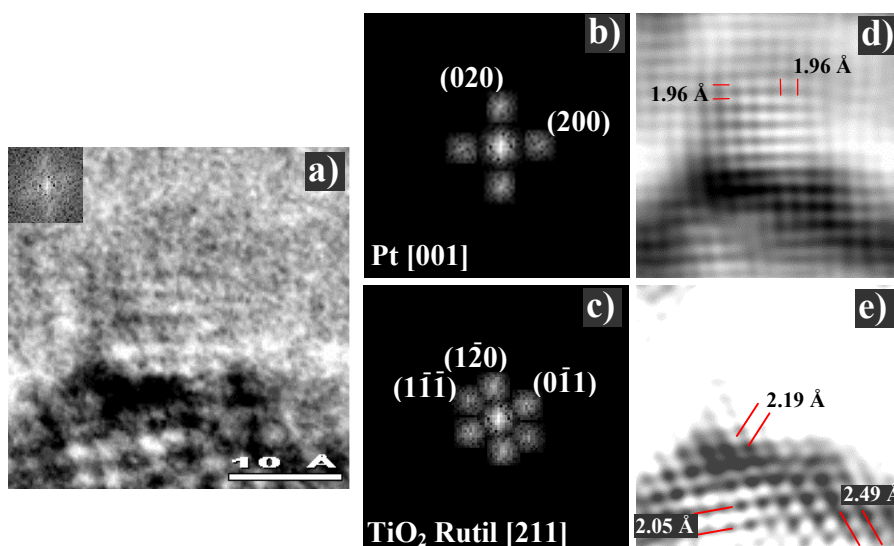


Figure 4.14. **a)** HRTEM micrograph for the *set A* sample with 5.8 Pt wt.% treated at 1100°C (*A5*). On the top left side of the experimental image the corresponding FFT is shown. **b-e)** DIP of the selected experimental cluster is made. After digital diffractogram indexation (**b-c**) we found that the Pt nanocluster was imaged in the [001] zone axis (**b,d**) on a [211] oriented TiO_2 rutile particle (**c,e**).

In the case of *set B* samples, the destructive grinding effects are not present in TiO_2 nanopowders. The main difference between these samples and those obtained in the first set is the good homogeneity in Pt clusters dispersion. In *figure 4.16* (corresponding to sample *B1*), there is an example of well-distributed nanoclusters on TiO_2 support. Although there is a clear difference in Pt distribution with respect to *set A*, the morphology of Pt nanoclusters remains equal. In this way, we find the same cluster shapes as

4. Superficial Clustering

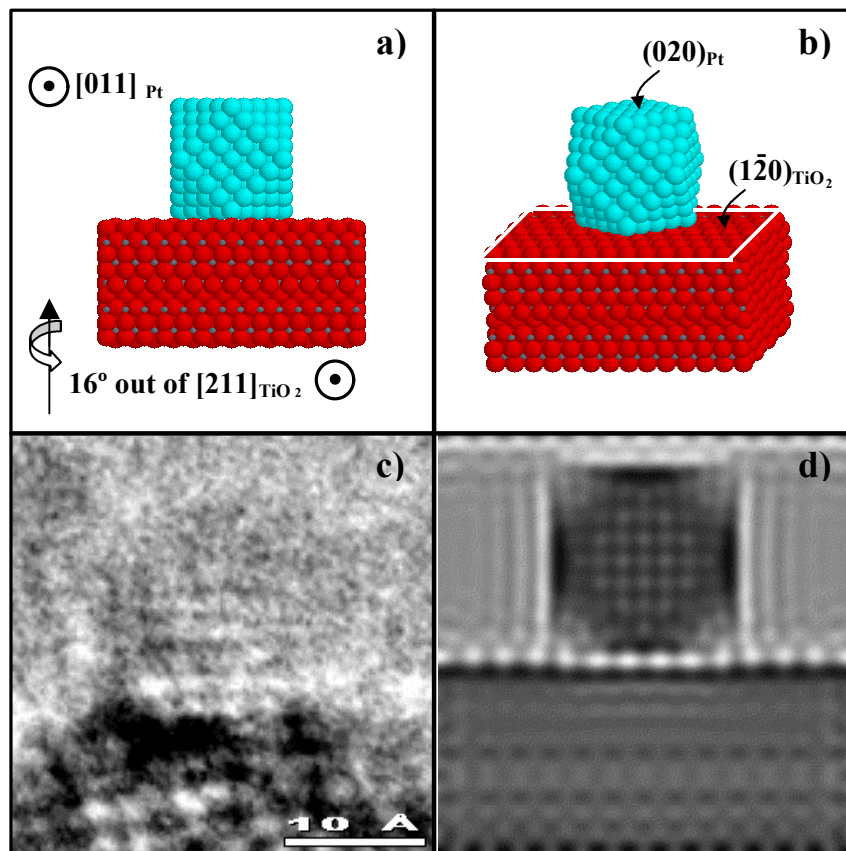


Figure 4.15.a-b. Supercell model for the Pt cluster showed in *figure 4.14*. The images behind correspond to the cluster-support system obtained experimentally (**c**) and to the computer simulation from the model presented above (**d**).

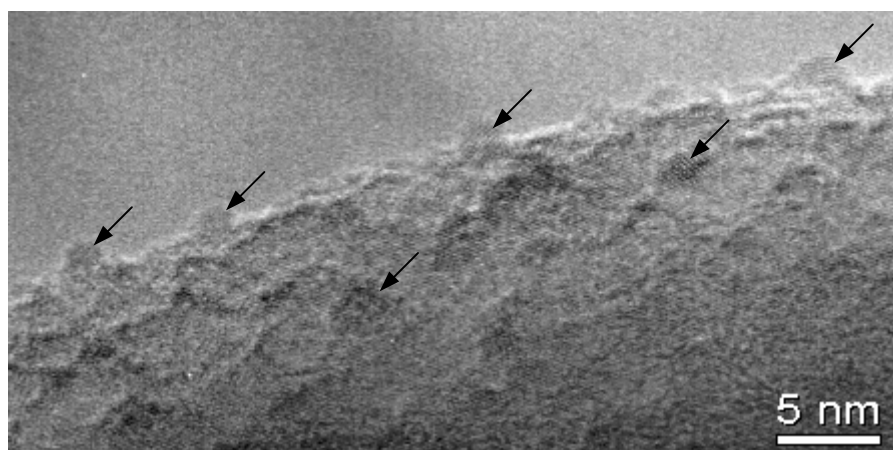


Figure 4.16. HRTEM micrograph for the *set B* sample with 0.58 Pt wt.% (*B1*). There were several Pt clusters embedded on TiO_2 surface (marked with black arrows).

in the precedent *set* of samples. As shown in *figure 4.17* (sample *B2*), particles with sizes smaller than 3 nm have projected morphologies similar to those that should be obtained in the case of cuboctahedral clusters. The particle selected in this case presents the typical (111) facets attributed to the projected cuboctahedron in the [011] zone axis.

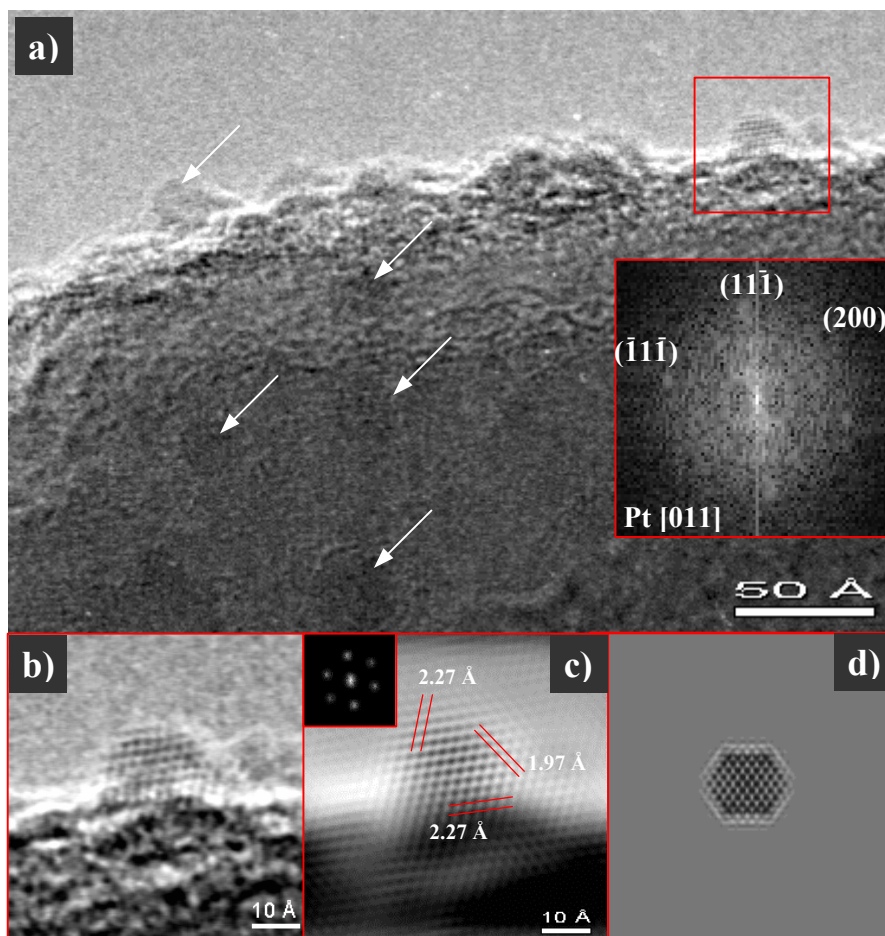


Figure 4.17. **a)** HRTEM micrograph for the *set B* sample with 2.9 Pt wt.% (*B2*). Metal Pt nanoclusters were homogeneously distributed over TiO_2 surface (some of them marked with white arrows in the top image). **b)** The selected nanocluster was studied in detail. **c)** After DIP, we could determine that the selected nanoparticle corresponded to a 309-atoms cuboctahedral Pt nanocluster oriented in the [011] zone axis. **d)** 309-atom cuboctahedral simulated image, in the [011] zone axis.

4. Superficial Clustering

Quasi-Spherical Nanoclusters ($d > 3\text{nm}$)

In the following, we will study the morphology of the Pt nanoclusters with diameter sizes bigger than 3 nm. *Figure 4.18*, also corresponding to the *B2* sample, shows the distribution of the Pt clusters. Notice that clusters with diameters bigger than 3 nm have quasi-spherical shapes, as we will deduce from the simulated models provided in the following. As we observe, when the cluster grows from small to bigger sizes, its morphology acquires more rounded shapes. We have selected two examples of clusters. In red, we select a special case in which the cluster presents wide black fringes on surface. In blue we select one of the typical spherical clusters without those black contrast fringes on surface. In *figure 4.18*, we carry out a detailed analysis of the Pt cluster selected in red. After DIP, we obtain that the TiO₂ rutile support (A) is oriented in the [001] direction, and that the Pt cluster (B) has been imaged in the [011] zone axis. There are some other lines that appear in the image and that do not correspond to any known material (C). Those lines have been attributed to Moiré fringes, formed by interfering two sets of lines (Pt planes with TiO₂ planes). Different supercell models have been tested until we found the one with the best agreement with the experimental image. In *figure 4.19*, we show the supercell model and simulated image for the Pt cluster selected in red in *figure 4.18*. In order to reach the perfect resemblance between experimental and simulated images (*figures 4.19.c* and *4.19.d*, respectively) we take into account an out of zone axis interface. The perpendicular planes to zone axis do not correspond to the epitaxial planes taken in our model. The cluster/support interface considered is: $(\bar{1}11)_{\text{Pt}} \parallel (\bar{1}11)_{\text{TiO}_2}$. Notice that the model has also been tilted 5° on $(11\bar{1})_{\text{TiO}_2}$ and $(31\bar{1})_{\text{Pt}}$ plane directions to assure a perfect agreement with the experimental results. The 5° tilt was found after comparison between experimental digital diffractogram with the diffraction pattern obtained for a pure [011] zone axis in a TiO₂ rutile layer. The most intense spot in the theoretical [011] zone axis pattern should

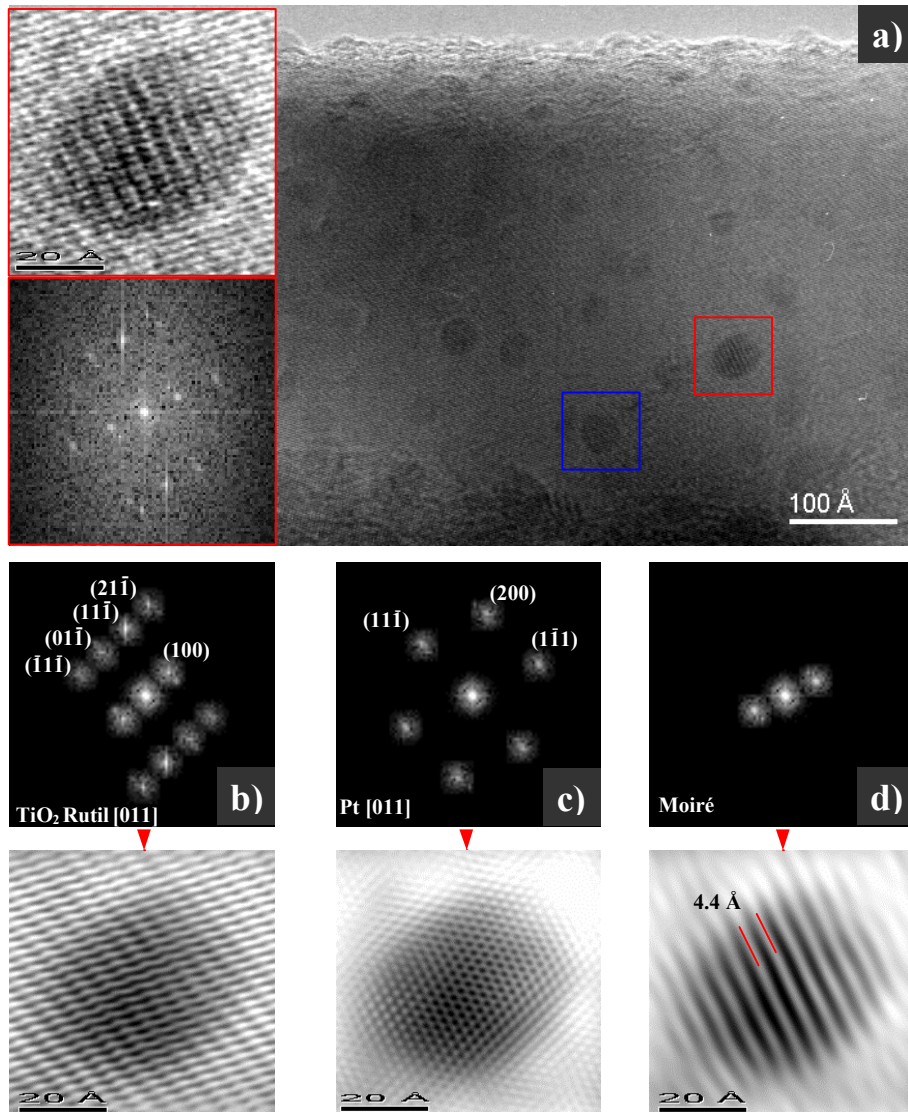


Figure 4.18. **a)** HRTEM micrograph for the *set B* sample with 2.9 Pt wt.% (*B2*). Metal nanoclusters tend to be spherical for sizes bigger than 3 nm. The cluster marked in red was analyzed carefully. The application of mask filters on the digital diffractogram allowed us to subtract image information. We could separate those planes corresponding to TiO₂ rutile from those corresponding to metal Pt, **b)** and **c)**, respectively. **d)** Subtracted constructive interferences between planes (Moiré).

4. Superficial Clustering

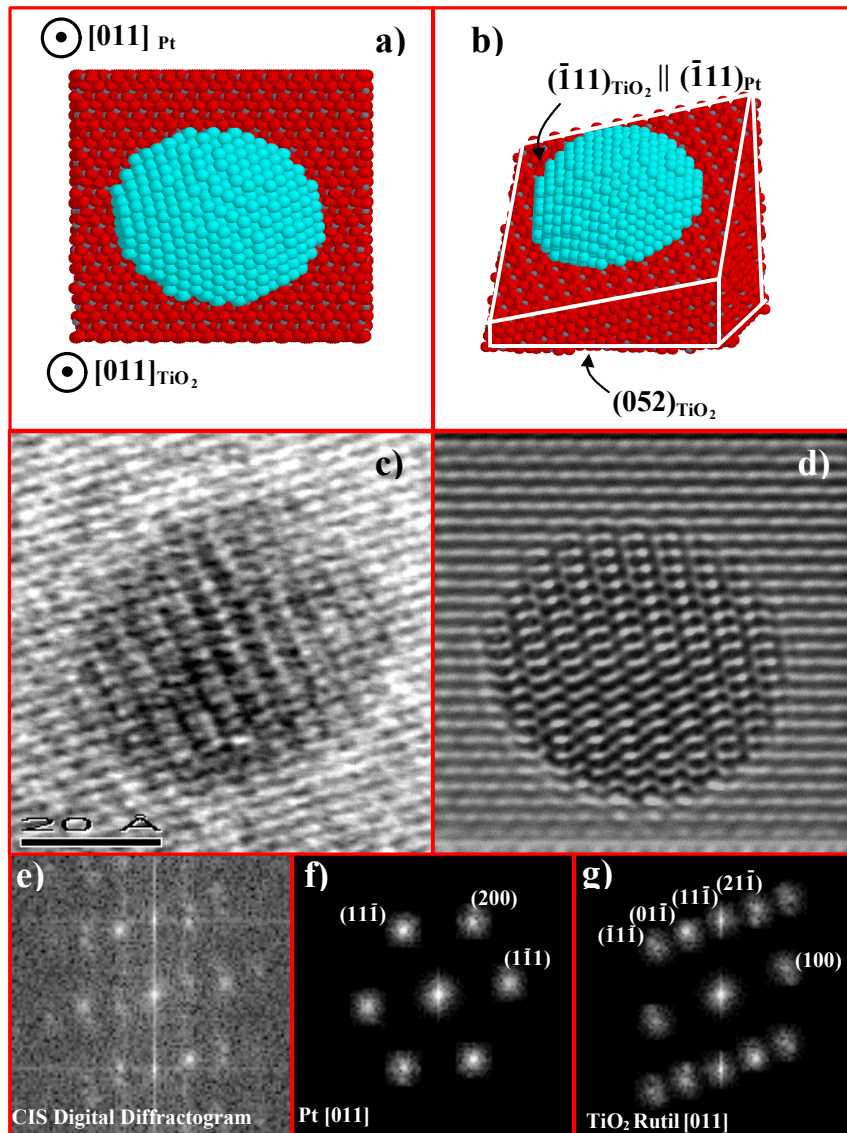


Figure 4.19.a-b. Supercell model for the Pt cluster marked in red in *figure 4.18*. The model was rotated 5° off $[011]$ towards $(1\bar{1}\bar{1})_{\text{TiO}_2}$ and $(3\bar{1}\bar{1})_{\text{Pt}}$ plane directions. The images behind correspond to the cluster-support system obtained experimentally (**c**) and to the computer simulation from the model presented above (**d**). We obtained the digital diffractogram of the CIS image (**e**). In (**f**) and (**g**) we show the filtered frequencies for Pt and TiO_2 respectively. Notice the perfect resemblance of the CIS diffractogram with the one obtained from the experimental image (*figure 4.18*).

correspond to the $(01\bar{1})$. In the experimental diffractogram, we find an unusual bright spot for $(1\bar{1}\bar{1})$ planes, suggesting a tilt in that direction. The 5° tilt on $(31\bar{1})_{\text{Pt}}$ direction keeps the orientation relationship obtained experimentally, where $(1\bar{1}\bar{1})_{\text{TiO}_2}$ and $(31\bar{1})_{\text{Pt}}$ directions are parallel. Comparing the digital diffractograms obtained for both, experimental (*figure 4.18*) and simulated (*figure 4.19.e*), we find that all the frequency spots coincide in angle and reciprocal distances. This is a good test to confirm the validity of our model.

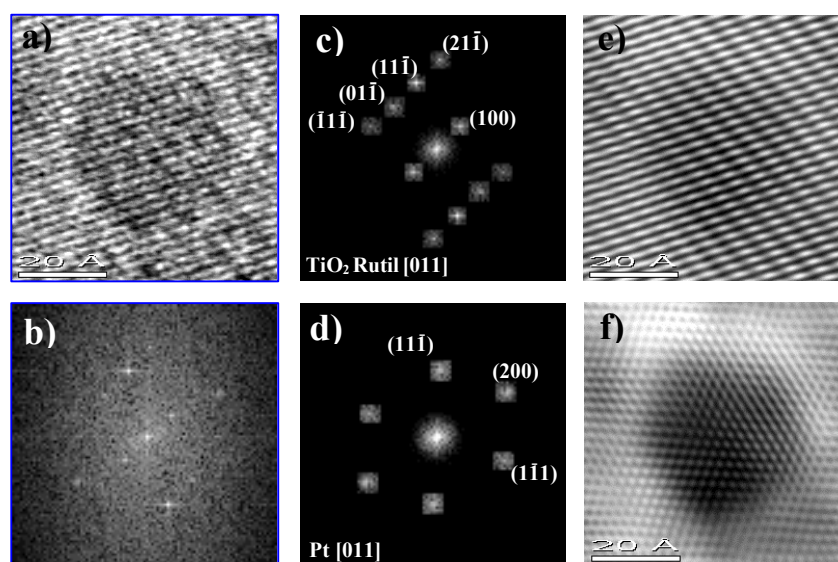


Figure 4.20. DIP of the Pt cluster marked in blue in *figure 4.18*. (a) Spherical Pt cluster on TiO_2 surface. (b) Digital diffractogram of the HRTEM image in (a). We could separate those frequencies corresponding to TiO_2 rutile (in the $[011]$ zone axis) from those corresponding to Pt (in the $[011]$ zone axis), (c) and (d), respectively. (e) and (f) reproduce the equivalent planes to frequencies filtered in (c) and (d), respectively.

The cluster selected in blue in *figure 4.18*, has also been studied carefully (*figures 4.20* and *4.21*). The orientation relationship associated with the experimental image is obtained after DIP (*figure 4.20*). This relation can be described as follows: $[011](1\bar{1}\bar{1})_{\text{Pt}} \parallel [011](21\bar{1})_{\text{TiO}_2}$. The only pair of possible planes that satisfies the orientation relationship is the perpendicular

4. Superficial Clustering

to both zone axes. Some other possibilities have been considered, but none of them present reasonable index values.

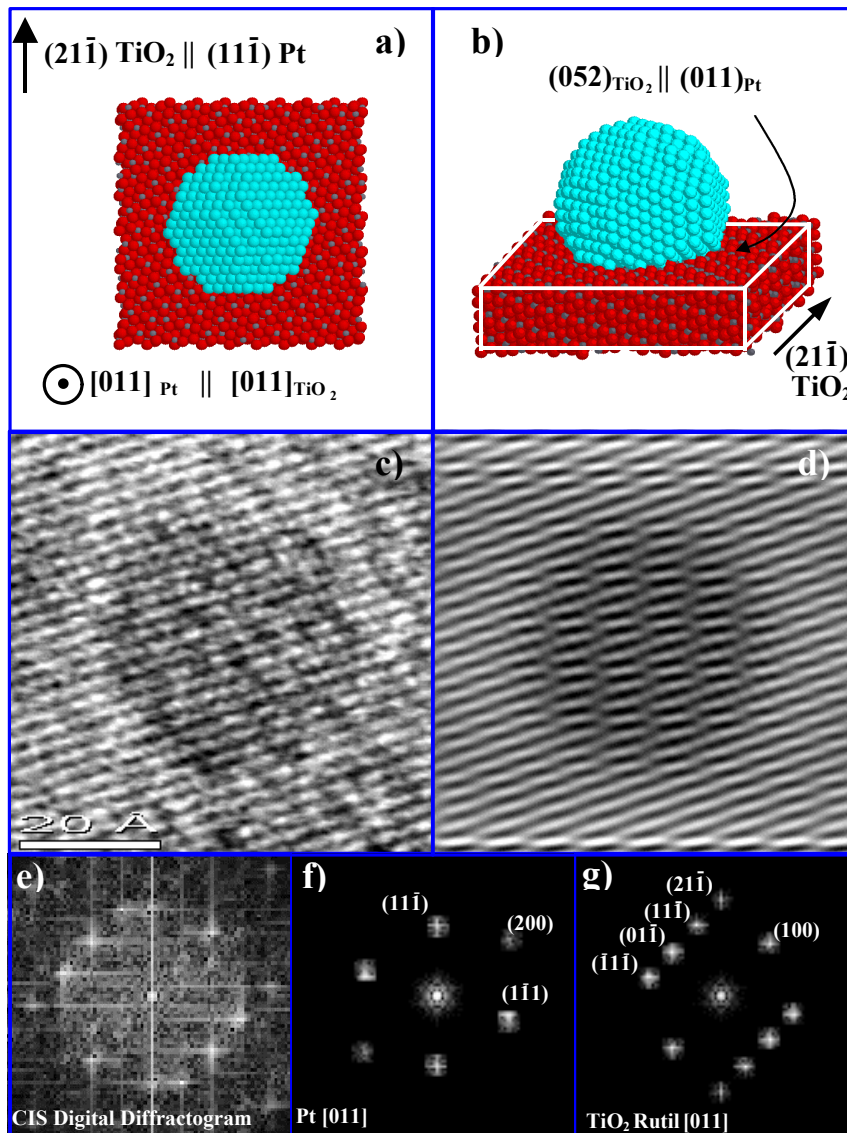


Figure 4.21.a-b. Supercell model for the Pt cluster marked in blue in *figure 4.18*. The model was rotated 5° on $(11\bar{1})_{\text{TiO}_2}$ and $(25\bar{5})_{\text{Pt}}$ plane directions. **c)** Experimental image corresponding to the cluster-support system and **d)** computer simulation from the model presented in **(a-b)**. We obtained the digital diffractogram of the CIS image **(e)**. In **(f)** and **(g)** we show the filtered frequencies for Pt and TiO_2 respectively. Notice the perfect resemblance of the CIS diffractogram with the one obtained from the experimental image **c)**.

We have created a supercell model based on the orientation relationship found (*figures 4.21.a and 4.21.b*). The epitaxial planes considered are those perpendicular to $[011]$ zone axis in both materials: $(011)_{\text{Pt}} \parallel (052)_{\text{TiO}_2}$ [^]. The model has been tilted 5° on $(11\bar{1})_{\text{TiO}_2}$ and $(25\bar{5})_{\text{Pt}}$ plane directions to assure a better resemblance with the experimental results. The experimental image has been compared with the simulated (*figures 4.21.c and 4.21.d*, respectively). The comparison between digital diffractogram obtained for both, experimental (*figure 4.20.b*) and simulated (*figure 4.21.e*) images are in good agreement. We obtain the same spot distribution in both, and moreover the relative position of planes coincides perfectly.

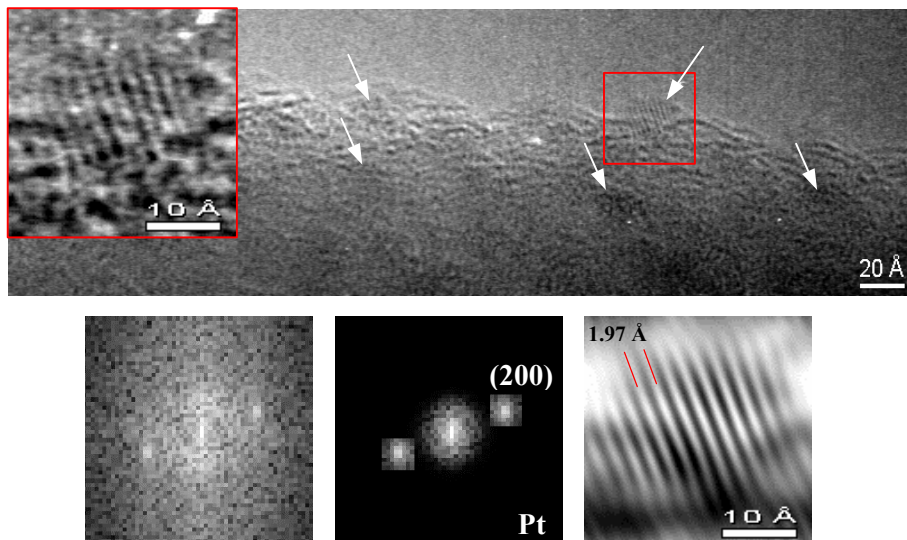


Figure 4.22. HRTEM micrograph for the *set B* sample with 5.8 Pt wt.% treated at 900°C (*B4*). Some Pt clusters have been marked with white arrows. Metal dispersion was homogeneous.

[^] In a non-cubic system, the (h,k,l) indexes of a plane can be different than the $[u,v,w]$ indexes for its perpendicular vector. In the case selected, the perpendicular plane to $[011]_{\text{TiO}_2}$ corresponds approximately to $(052)_{\text{TiO}_2}$.

4. Superficial Clustering

Another good example of platinum homogeneous distribution is shown in *figure 4.22*. The Pt cluster selected is not oriented in one of the preferable zone axis that allows a bidimensional resolution of planes. In this example we can just visualize the $(200)_{\text{Pt}}$ planes. We would need at least the information provided from two planes to determine the cluster zone axis. Although we have applied a noise filter to the image, the cluster morphology is not clear in this case. However, attending to the results obtained in other examples, we can assume cuboctahedral morphology, as the cluster diameter is smaller than 3 nm.

Hot Zones

Until now, all the examples showed for samples from *set B* have got a good distribution of Pt clusters, but few TiO_2 particles present zones on surface where there is not a homogeneous distribution of platinum clusters. In these zones (“hot-zones”), we have observed the presence of big platinum clusters (> 10 nm) as well as a reduction of the number of the small clusters (1-8 nm) in its neighborhood. In *figure 4.23* we show an example of this phenomena. The number of platinum clusters is far lower than the mean observed in other zones of the same sample (*B4*). However, the big Pt cluster on the right down corner concentrates the main part of the Pt atoms present on TiO_2 surface. If we take into account both kinds of clusters, the mass density of platinum on TiO_2 surface remains constant, even in these “hot-zones”. The statistical calculus about sample densities is made in the *Section 4.4.2* of this chapter. As the sample was submitted to a heating process during preparation, it is possible to think that the temperature in punctual regions could acquire a higher value than the mean leading to the inhomogeneity of platinum distribution. That is the reason why we call these zones as “hot-zones”.

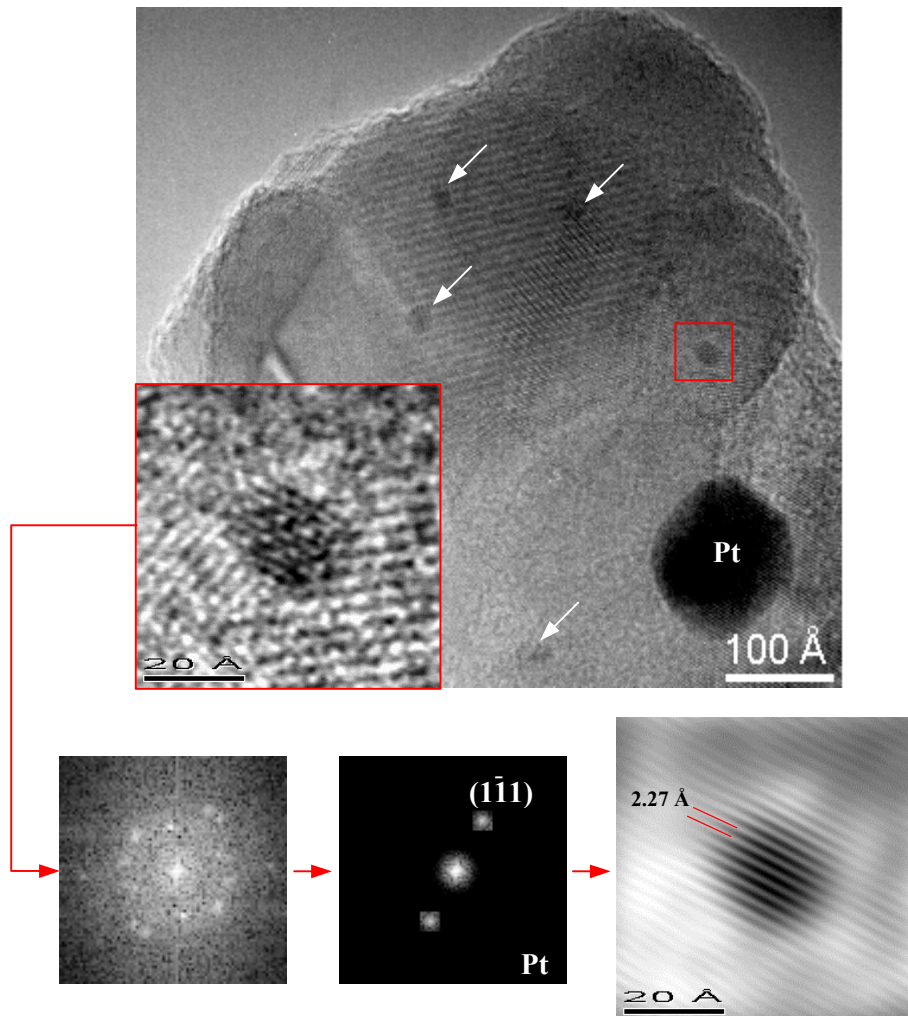


Figure 4.23. HRTEM micrograph for the *set B* sample with 5.8 Pt wt.% treated at 900 °C (*B4*). Some Pt nanoclusters have been marked with white arrows. The presence of a big size Pt cluster is related with the decreasing of small nanocluster density in the so-called “hot-zones”.

4. Superficial Clustering

4.3.3.2 Minority Structural Phases

The former results have shown that platinum clusters adopt the cubic metallic phase and titanium oxide the tetragonal rutile one. However, few examples of other phases have been observed on HRTEM micrographs. Its quantity can not exceed the 1% because we could not find any evidence of them in the XRD spectra obtained for the samples studied. Anyway, in the following we present a pair of examples of these non-common phases.

The cluster in red in *figure 4.24* has been carefully analyzed. We have obtained the digital diffractogram of the cluster selected. A fast overview on the spot pattern indicates that the cluster phase does not correspond to metallic platinum or to rutile titanium oxide. We have

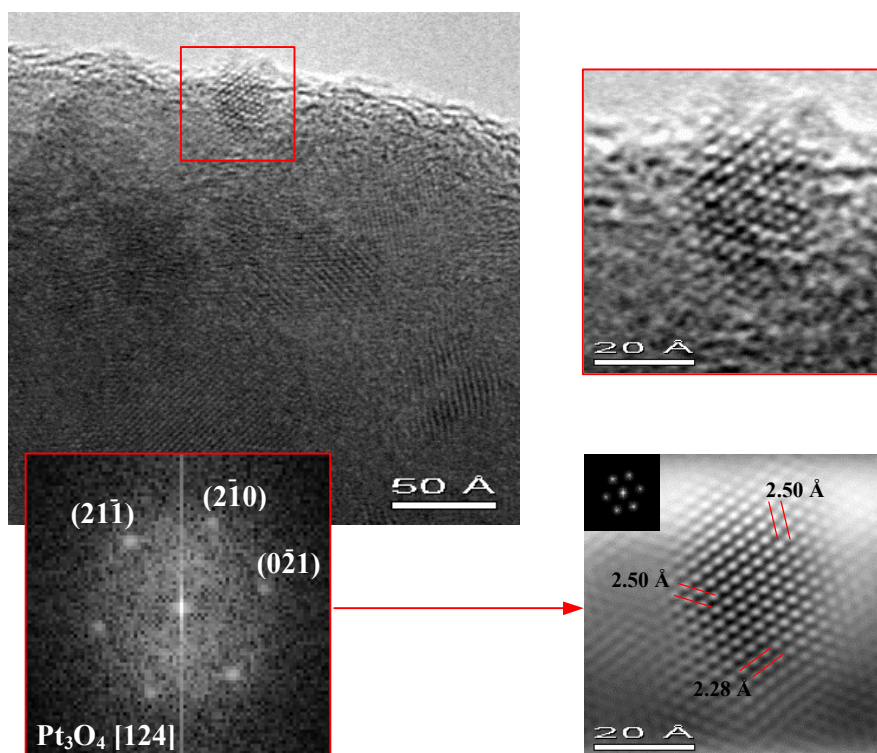


Figure 4.24. HRTEM micrograph for the *set B* sample with 0.58 Pt wt.% (*B1*). The presence of Pt oxides was rarely found in our samples. In the image above we show an example of Pt_3O_4 oxide phase.

compared the angle and distances between planes with the ones that should be obtained in some of the possible Pt oxides and Pt-Ti alloys. After few attempts we have obtained that the cluster selected adopts the Pt_3O_4 cubic phase and it is imaged in the $[124]$ zone axis. It has been possible to find the resulting phase because we have bidimensional resolution in the HRTEM image, which let us compare angles and distances between planes included in a determinate zone axis. In the case of the Pt_3O_4 phase, the relationship in reciprocal space for diffracted spots in the $[124]$ zone axis are given in *table 4.5*. Data showed in this table was calculated using *EJEZ* software.

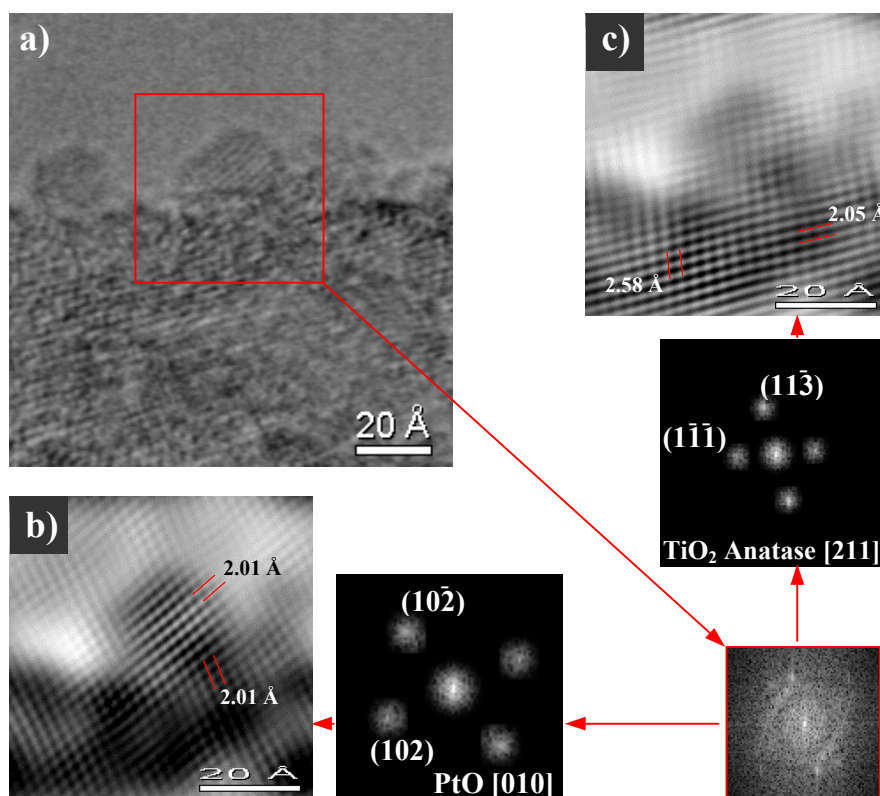


Figure 4.25. a) HRTEM micrograph for the *set A* sample with 5.8 Pt wt.% treated at 1100 °C (A5). b) PtO cluster on c) TiO_2 anatase particle. These phases were rarely found in our samples.

4. Superficial Clustering

Plane 1	Plane 2	D1 (Å)	D2 (Å)	Angle	Zone Axis
(21-1)	(2-10)	2.28	2.50	56.8 °	[124]
(0-21)	(2-10)	2.50	2.50	66.4 °	[124]

Table 4.5. Angle and distance plane relationship for Pt₃O₄ in the [124] zone axis.

In the example shown in *figure 4.25*, the selected cluster presents a PtO phase, while the support has the anatase metastable phase. Anatase support has been found to be oriented near the [211] zone axis and PtO cluster near the [010]. Relationships between plane distances and angles for TiO₂ anatase and PtO phases in those zone axes are shown in *tables 4.6* and *4.7*, respectively.

Plane 1	Plane 2	D1 (Å)	D2 (Å)	Angle	Zone Axis
(11-3)	(1-1-1)	2.58	2.05	79.9 °	[211]

Table 4.6. Plane distances and angle relationship for TiO₂ anatase in the [211] zone axis. The relationship has been obtained using the software *CARINE 3.1*.

Plane 1	Plane 2	D1 (Å)	D2 (Å)	Angle	Zone Axis
(10-2)	(102)	2.01	2.01	82.6 °	[010]

Table 4.7. Angle and distance plane relationship for PtO in the [010] zone axis. Data obtained from *EJEZ* software. Structural parameters found in: [8, 9].

4.3.3.3 Orientation Relationship between Pt clusters and Titania support

From Materials Science point of view, the possible epitaxy between materials is one of the most interesting parameters that can be analyzed. Epitaxial relations can provide us important information about the preferable planes that clusters and supports have on the interface.

Normally, when we talk about epitaxy, we make reference to the characteristics of the interface between two material layers considering a perfect matching between interface atoms [10, 11, 12]. However, the materials studied in this *Thesis* work have special characteristics that make difficult the normal procedure for epitaxy analysis. In this way, we will

describe as epitaxial relationship, the extended model used in catalysis, where the structural correspondences found between metal clusters and oxide supports will allow us to define a small-size coincidence cell that can be repeated periodically along the structural surface directions. In the following, we will consider that there is “epitaxy” when one of these coincidence cells can be established with low misfit values (see *expression 4.1*) [13],

$$misfit = \frac{d_{Pt} - d_{TiO_2}}{d_{TiO_2}} \times 100 \quad (4.1)$$

The standard procedure in semiconductor science to analyze an epitaxial relationship between two layers consists in the meticulous observation of the sample in cross-section. Plane and zone axis relations can be extracted from HRTEM micrographs obtaining their digital diffractogram, and then we can use all this information to create a supercell model that will be simulated using a multislice method program (*EMS*).

Those supercell models are created giving the atomic positions for all the atoms that compose both material layers. The introduction of such a huge amount of coordinates one by one becomes an insane work that should be avoided. Instead of that, we can use already made software routines that will soften our work.

Analysis of Big Clusters Epitaxy (> 5nm)

One of the software routines used to build up the supercell models was developed in CEMES-CNRS in Toulouse (France). This program is called *INDEM* and it allows the user to build two epitaxed material layers using the orientation relationship observed in HRTEM micrographs.

In our case, platinum clusters acquire reduced sizes leading to small epitaxial interfaces. The use of programs like *INDEM* can be useful to simulate the interface of the biggest platinum clusters (lateral size > 5 nm), but it will not be so accurate for clusters with smaller sizes.

In *figure 4.26* we show an example of the clusters that can be simulated using *INDEM*. In this case, the image was taken from a *set A* sample where

4. Superficial Clustering

the platinum cluster dispersion was inhomogeneous. The lateral size of the cluster selected is of about 10 nm. The cluster/support interface will be easily modeled using *INDEM*. We have digitally processed the experimental image (figure 4.26) obtaining the orientation relationship for the metal/oxide

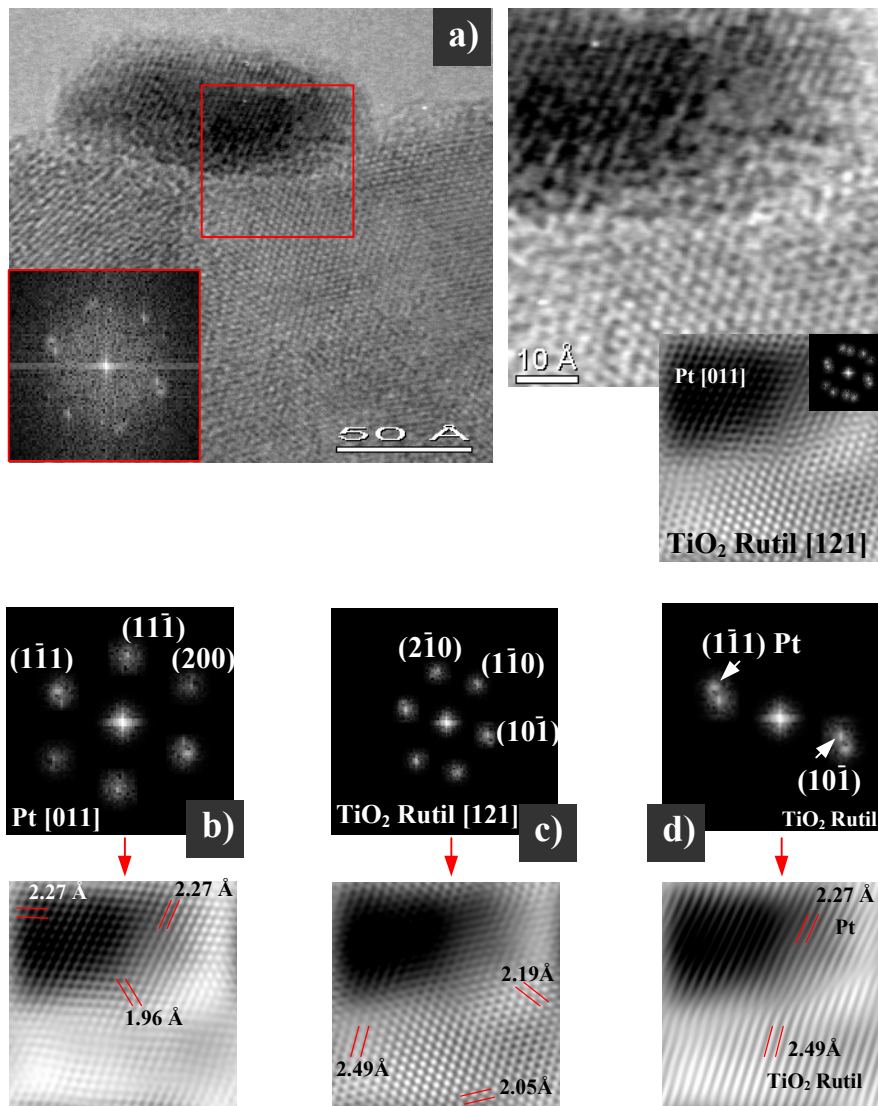


Figure 4.26. **a)** HRTEM micrograph for the *set A* sample with 5.8 Pt wt.% treated at 1100 °C (45). We studied the possible epitaxy of a Pt cluster embedded on TiO₂ rutile particle. The area selected in the top image was processed obtaining the best contrast for Pt (**b**) and TiO₂ planes (**c**) separately. **d)** (1-11) and (10-1) planes for Pt and TiO₂ respectively are not totally aligned.

system. The TiO_2 rutile substrate is oriented in the $[121]$ zone axis, while the Pt cluster in the $[011]$ direction. We observe that $(\bar{1}\bar{1}\bar{1})_{\text{Pt}}$ and $(10\bar{1})_{\text{TiO}_2}$ planes are quasi parallel in the image. Moreover, $(1\bar{1}\bar{1})_{\text{Pt}}$ and $(2\bar{1}0)_{\text{TiO}_2}$ planes are also quasi parallel and they are placed in the interface. The epitaxial relationship selected for the supercell model is: $[011](1\bar{1}\bar{1})_{\text{Pt}} \parallel [121](2\bar{1}0)_{\text{TiO}_2}$. The model was simulated for different image defocus and layer thickness. In *figure 4.27* we show a map with all the simulated images obtained from the supercell model created. The experimental image has been compared with the simulations. In *figure 4.28*, we can appreciate the good resemblance between the experimental image after noise filtering and one of the simulated (we have selected the simulated image that presents the best agreement, layer thickness = 6 nm and defocus = 60 nm). Simulated images would suggest a possible epitaxy between metal cluster and support. However, a further study of the model created clearly shows that both materials have not an epitaxial relationship. In *figure 4.29*, supercell model has been visualized in the different axis orientations. In *figure 4.29.a*, the image is oriented following the epitaxial relationship selected for the simulation. In this zones axis, Pt atoms in $(\bar{1}\bar{1}\bar{1})$ planes present a -8.8% misfit with respect to TiO_2 $(10\bar{1})$ planes (*expression 4.1*), where $d(\bar{1}\bar{1}\bar{1})_{\text{Pt}} = 2.27 \text{ \AA}$ and $d(10\bar{1})_{\text{TiO}_2} = 2.49 \text{ \AA}$.

Such a misfit value would be compatible with a stressed epitaxy between cluster and support. When we rotate the whole model 90° around Z-axis, *figure 4.29.b*, the idea of epitaxial growth becomes hardly supported. Pt atoms do not coincide in spatial positions with TiO_2 atoms. The same phenomenon occurs when we visualize the supercell model in planar (top) view (*figure 4.29.c*). In this later case we also appreciate that atomic platinum positions do not coincide with the ones for TiO_2 . The analysis performed suggests that the platinum cluster is not epitaxed on TiO_2 particle surface.

4. Superficial Clustering

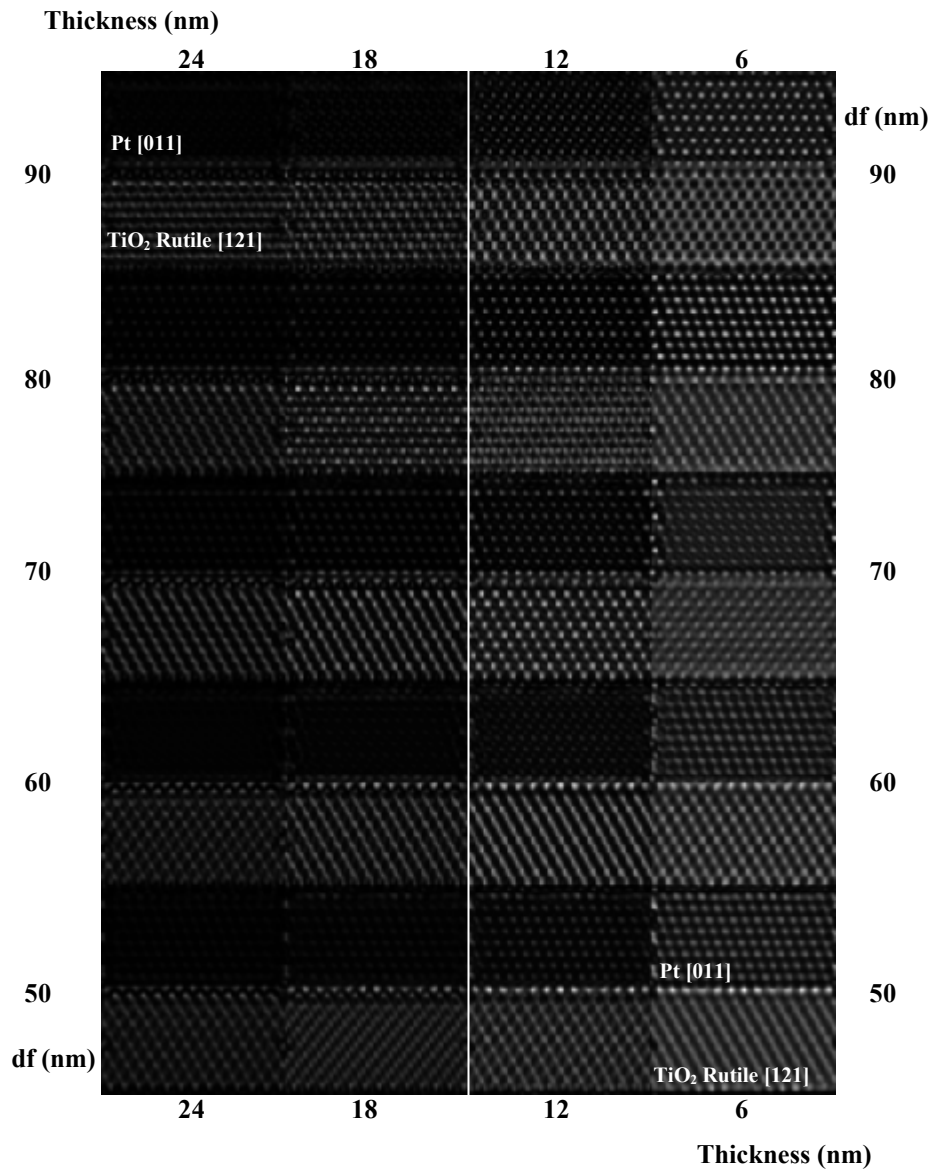


Figure 4.27. Map of simulated images for the interface $[011](11-1)_{\text{Pt}} \parallel [121](2-10)_{\text{TiO}_2}$. The *supercell file* was created using the program INDEM. Microscope conditions were taken as 300 kV and $C_s = 1.2$ nm. Images size is 512x461 pixels with a resolution of 0.00802 nm/pixel.

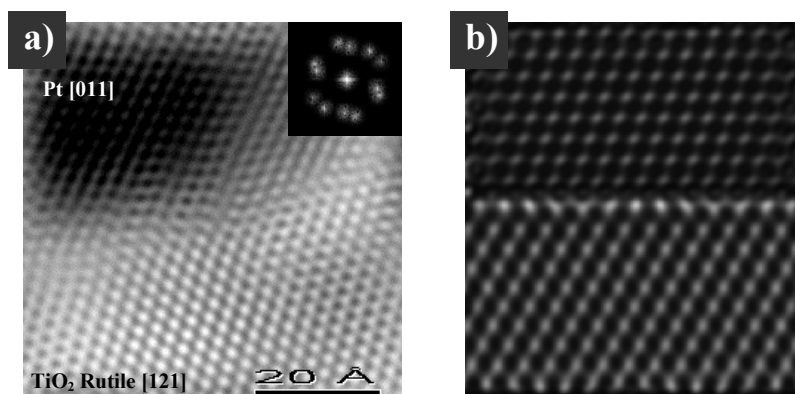


Figure 4.28. **a)** HRTEM experimental micrograph and **b)** the corresponding simulated image. The simulated has a horizontal side length of 3.697 nm. Microscope conditions were taken as 300 kV and $C_s = 1.2$ nm, layer thickness = 6 nm and defocus = 60 nm. Notice that the simulated image was horizontally twisted with respect to the one shown in *figure 4.27* to assure a good resemblance with the experimental one.

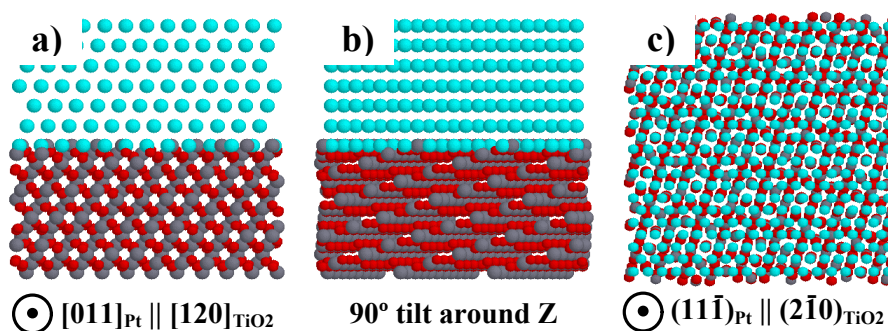


Figure 4.29. Supercell model used for the simulations presented in *figures 4.27* and *4.28*. The epitaxy could be possible taking into account *figure (a)*. Further examinations of the tilted model around Z-axis (**b**) and the plan view (**c**) confirms that there is not an epitaxy between interfacial planes.

Analysis of Small Clusters Epitaxy (1 – 5 nm)

In order to study the epitaxial relationship of the small platinum clusters (lateral size < 5 nm) we can use the supercell models created with the program *RHODIUS* (see characteristics in *Chapter 2*), which allows to build complex models of small structures epitaxed on the desired support. In

4. Superficial Clustering

figure 4.30, we show a plan (top) view of the model used in figure 4.12. Notice that the atomic radii have been reduced to let us observe the atomic projections in the zone axis. There is a good coincidence between $(1\bar{1}\bar{1})_{\text{Pt}}$ and $(200)_{\text{TiO}_2}$ planes. The lateral misfit between them is just -1.3% , $d(1\bar{1}\bar{1})_{\text{Pt}} = 2.27 \text{ \AA}$ and $d(200)_{\text{TiO}_2} = 2.30 \text{ \AA}$. Moreover, if we consider $(\bar{2}\bar{1}\bar{1})_{\text{Pt}}$ and $(0\bar{1}\bar{1})_{\text{TiO}_2}$ planes, we can obtain a new coincidence relation. In this case, every three $(\bar{2}\bar{1}\bar{1})_{\text{Pt}}$ plane spacings a platinum atom coincide with a titanium atom in two $(0\bar{1}\bar{1})_{\text{TiO}_2}$ plane spacings, giving an equivalent misfit of -3.6% ; $3 \cdot d(\bar{2}\bar{1}\bar{1})_{\text{Pt}} = 3 \cdot 1.60 \text{ \AA} = 4.80 \text{ \AA}$; $2 \cdot d(0\bar{1}\bar{1})_{\text{TiO}_2} = 2 \cdot 2.49 \text{ \AA} = 4.98 \text{ \AA}$, results are summarized in table 4.8. This structural correspondence allows us to define a small-size coincidence cell that can be repeated periodically along the $[1\bar{1}\bar{1}]_{\text{Pt}}$ and $[\bar{2}\bar{1}\bar{1}]_{\text{Pt}}$ directions. The coincidence cell has been marked in figure 4.30, and its dimensions are $3 \cdot [1\bar{1}\bar{1}]_{\text{Pt}} \times 3 \cdot [\bar{2}\bar{1}\bar{1}]_{\text{Pt}}$. The epitaxial relationship can be described as follows: $[1\bar{1}\bar{1}](011)_{\text{Pt}} \parallel [200](052)_{\text{TiO}_2}$.

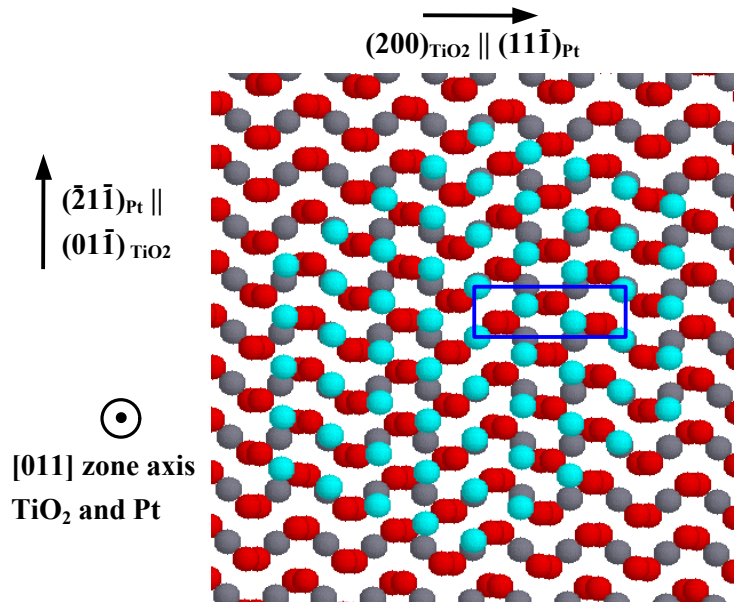


Figure 4.30. Structural model of metal/support interfaces corresponding to the one studied in figures 4.11 and 4.12. Epitaxial relationship is $[1\bar{1}\bar{1}](011)_{\text{Pt}} \parallel [200](052)_{\text{TiO}_2}$.

N·Plane 1	N·Plane 2	D1 (Å)	D2 (Å)	misfit (%)
(11-1) _{Pt}	(200) _{TiO2}	2.27	2.30	-1.3
3·(-21-1) _{Pt}	2·(01-1) _{TiO2}	3·1.60	2·2.49	-3.6

Table 4.8. Epitaxial relations for the model presented in *figure 4.30*.

Another epitaxial relationship has been studied. In this case we have considered the supercell model used in *figure 4.15*. The top view of this model is shown in *figure 4.31*. Observing the model we find that there also exist a certain structural correspondence between both interfaces. In this case, there are also two pairs of planes that have a good correspondence. The first correspondence is between (200)_{Pt} and (002)_{TiO2} planes. Every three (200)_{Pt} and four (002)_{TiO2} plane spacings there is a platinum atom that coincides with the position of a titanium atom, giving an equivalent misfit of -0.7%; $3 \cdot d(200)_{Pt} = 3 \cdot 1.96 \text{ \AA} = 5.88 \text{ \AA}$; $4 \cdot d(002)_{TiO2} = 4 \cdot 1.48 \text{ \AA} = 5.92 \text{ \AA}$. Moreover, considering (020)_{Pt} and (120)_{TiO2} planes, we can obtain a new coincidence relation. Now, both planes coincide pretty well with a misfit of -4.4%; $d(020)_{Pt} = 1.96 \text{ \AA}$; $d(120)_{TiO2} = 2.05 \text{ \AA}$, complete results are summarized in *table 4.9*. This structural correspondence also allows us to

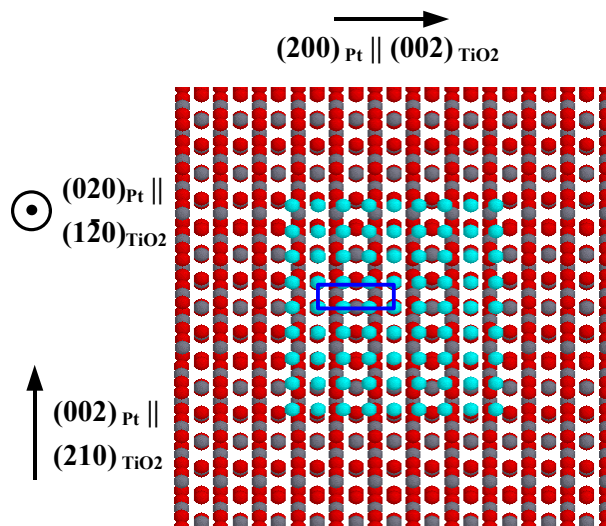


Figure 4.31. Structural model of metal/support interfaces corresponding to the one studied in *figures 4.14 and 4.15*. Epitaxial relationship is $[001](020)_{Pt} \parallel [210](1-20)_{TiO2}$.

4. Superficial Clustering

define a small-size coincidence cell that can be repeated periodically along the $[200]_{\text{Pt}}$ and $[002]_{\text{Pt}}$ directions. The coincidence cell has been marked in *figure 4.31*, and its dimensions are $3 \cdot [200]_{\text{Pt}} \times 1 \cdot [002]_{\text{Pt}}$. In this case the epitaxial relationship is: $[001](020)_{\text{Pt}} \parallel [210](\bar{1}\bar{2}0)_{\text{TiO}_2}$.

N·Plane 1	N·Plane 2	D1 (Å)	D2 (Å)	<i>misfit</i> (%)
$3 \cdot (200)_{\text{Pt}}$	$4 \cdot (002)_{\text{TiO}_2}$	3·1.96	4·1.48	-0.7
$(002)_{\text{Pt}}$	$(210)_{\text{TiO}_2}$	1.96	2.05	-4.4

Table 4.9. Epitaxial relations for the model presented in *figure 4.31*.

The above epitaxial relationships have been found in some of the samples analyzed in our work, but we can not exclude the existence of some others. These results as well as some other possibilities will be extensively discussed in *Section 4.3.4.4*.

4.3.3.4 Platinum Macro-Agglomeration

Metal distribution in our samples, even in those from *set B*, present the effects of macro-agglomeration. In recent works we showed that this phenomenon is typical in metal/oxide systems, as in the case of Au loaded in SnO_2 [14] or in the case of the system studied in this *thesis* work, Pt in TiO_2 [1, 2]. These effects can not be avoided, although they can be reduced. As shown in *figure 4.32*, between the TiO_2 nanopowders there is a black particle. The darker contrast of the particle marked, in comparison with the rest, makes us think that it can not be a titanium oxide nanoparticle. The darkness suggests a higher density material, and attending to the materials we have in our samples, it should be a platinum nanoparticle. Such opacity of the particle makes impossible to obtain a HRTEM micrograph with plane resolution. However, it was easy to obtain the EDS spectra of the particle, and corroborate that it was composed of platinum. The corresponding EDS spectrum is also shown in *figure 4.32*. In the following, we will call these platinum particles as *Macro-Agglomerated Clusters* (MAC). We have found

that these MAC have sizes similar to the TiO_2 nanoparticles (50-300 nm). Sometimes, these MAC can be present in a high density, as in the example showed in *figure 4.33*. Notice that images showed in *figures 4.32* and *4.33* correspond to the same sample. It means that MAC distribution is highly inhomogeneous. The loss of homogeneity makes difficult an accurate analysis of MAC density. In *Section 4.4.4*, we will use different complementary techniques in order to determine indirectly the mass density of this MAC with respect to the rest of Pt present in our samples.

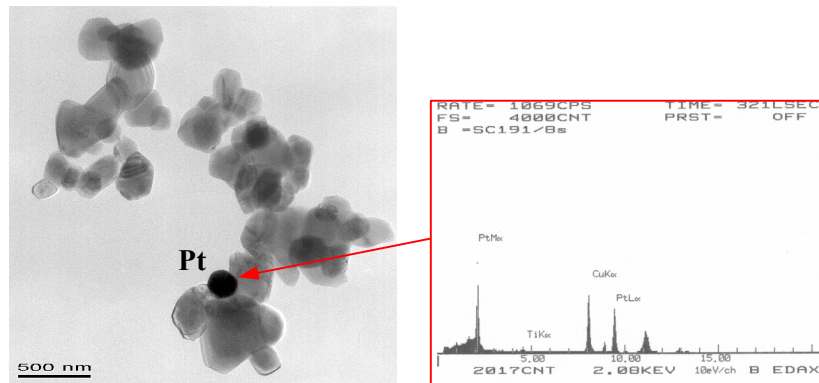


Figure 4.32. HRTEM micrograph for the *set B* sample with 0.58 Pt wt.% treated at 900 °C (*B1*). The arrow marks a big Pt cluster surrounded by TiO_2 nanopowders. The EDS spectrum of the cluster is also shown.

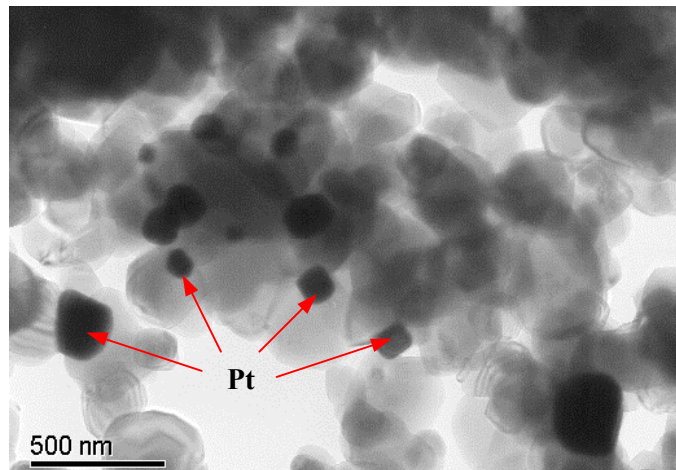


Figure 4.33. HRTEM micrograph for the *set B* sample with 0.58 Pt wt.% treated at 900 °C (*B1*). The area imaged presents a big concentration of big Pt clusters.

4.3.4 Discussion about Nanostructural Results

In the following we will discuss the main results showed in *Section 4.3.3*. There are several points that should be commented attending to results obtained.

4.3.4.1 Presence of the TiO₂ Rutile Stable Phase

Although we could find few anatase nanoparticles in our samples, we have demonstrated that the main part of TiO₂ nanopowders has adopted the TiO₂ rutile stable phase. We have found the anatase phase just in two occasions after analyzing several hundreds of TiO₂ nanoparticles in HRTEM micrographs. Complementary techniques as XRD have given us more precise information about sample composition. TiO₂ rutile peaks appear clearly in XRD spectra and there is not data that referred to the anatase phase. This result suggests that anatase phase should be present in less than 1 % of our TiO₂ nanoparticles. The thermal treatment used to stabilize our TiO₂ samples in the rutile stable phase has been shown to be highly effective. As our samples have been all treated at temperatures higher than 700 °C, in air (*set A*) or in N₂ (*set B*) at least during 4 hours, these are the results we could expect. As shown in literature, the anatase metastable phase becomes rutile (stable) when it is submitted to temperatures above 700 °C [15, 16] in an inert environment, or even at lower temperatures, around 500 °C, under reducing conditions (H₂) [17]. It can be also pointed out that phase transition seems not to be affected by Pt loading, since transition temperatures are comparable to those found in the case of pure TiO₂ with no additives added (compare for example with results obtained for *Sample A* in *Chapter 3*, where phase transition temperature was also around 700 °C).

4.3.4.2 Effects of Grinding to Samples Structure

In a first approach and as it has been previously reported, sample grinding promotes a reduction in grain size [18, 19, 20, 21]. All the samples analyzed have been grinded, although the grinding process has been applied in different steps of sample preparation.

On one hand, in *set A samples* we have applied the grinding process to the last step of the preparation method. As we have observed from low magnification TEM micrographs, TiO₂ nanograins show irregular faceted borders. When we use HRTEM techniques on the same samples, we observe that those nanometric grains have a polycrystalline structure, every grain is formed of several crystals randomly oriented. The result obtained suggests that the grinding process may break small parts of the original TiO₂ particles creating the facets observed, and then, those snatched small crystals may be stucked to the bigger particles surface.

On the other hand, *set B samples* show quasi-spherical shapes with defined borders in low magnification images. Under HRTEM conditions, we can see how every TiO₂ grain is monocrystalline, presenting a unique orientation. Although these samples have also been submitted to a grinding process, it has been performed before the thermal treatment. Thermal treatment could lead to a recrystallization of TiO₂ nanograins; thus these grains could acquire quasi-spherical shapes.

The influence of grinding on SGS characteristics has been widely studied. Several authors have suggested that the particle size reduction due to grinding can increase the sensitivity of the sensor as well as an increase in the effective active surface [18].

It has been useful to study the platinum clusters morphology in both sets of samples, but in the following our statistical analysis of the platinum dispersion will be only carried out in *set B samples*. In *set A samples* platinum clusters density is inhomogeneous and moreover TiO₂ grains present high size dispersion, however *set B samples* have a homogeneous density of Pt clusters and their TiO₂ grain shapes and sizes are well defined. Both conditions commented above are necessary to obtain a precise

4. Superficial Clustering

statistical analysis of the platinum dispersion, as we will show in *Section 4.4.2*.

4.3.4.3 Platinum Clusters Morphology

We have analyzed the platinum clusters morphology from HRTEM micrographs. Several structural models have been suggested for the clusters found and the corresponding CIS have been carried out in order to corroborate the proposed models. The results obtained suggest that platinum nucleated as cuboctahedral nanoclusters for diameter sizes smaller than 3 nm and in non-regular faceted shapes, which tended to be spherical, for bigger diameter sizes.

Noble metal nanoclusters morphology has been widely studied theoretically and experimentally in literature. Some of the investigations have been focussed on obtaining information about the structures and shapes of the nanoclusters. This information is normally obtained from the contour and contrast characteristics of the particle images even at lower magnifications [22]. Moreover, general information about the internal structure type of a particle is obtained both from the shape of the particle and especially from atomic resolution micrographs. Atomic resolution adds credibility to the shape determination. Some of these works show that it is also possible to get useful information about more detailed structural features from atomic resolution micrographs [22, 23, 24]. Using this information as input, HRTEM CIS of the cluster image has been performed in order to draw accurate conclusions about the structure (and lattice parameters) of the cluster. Image simulations of metal clusters have been previously performed on metal particles with various structures (e.g. cuboctahedral, decahedral and icosahedral). Comparisons between the real structures of metal particles and structures derived from simulated images have been previously made [23, 25, 26].

As suggested by M. –J. Casanove and co-workers [27], in the case of close packed cubic fcc metal clusters, the simplest model to consider would be a super-cell of the bulk lattice. Taking in account total free energy

considerations, it appears that preferred shapes for such particles would be closed-shell cuboctahedra. As contribution of the surface energy is very high in small colloids some authors suggested considering Multiply Twinned Particles (MTP) models [27, 28]. The most used MTP geometries are icosahedra and decahedra, stable and quasi-stable geometries from the point of view of the elasticity theory [29, 30].

There are a wide variety of geometry models related to noble metal nanoclusters in literature. Icosahedral nanoclusters have been found in the case of Pt and Pd for reduced sizes ($d < 3$ nm), F. Dassenoy [26] and K. Ebitani et al. [31], respectively. However, for the same range of sizes ($d < 3$ nm) cuboctahedral geometry has also been found; S. Bernal and co-workers [23, 24] demonstrated that Rh clusters grew epitaxially on CeO_2 supports adopting cuboctahedral shapes. The same morphology was found by P.- A. Buffat et al. in the case of Au nanoclusters [32]. Other results talk about half-octahedral geometries of Au clusters epitaxed on MgO, as S. Giorgio et al. [33] found in their study of MgO microtubes. Even some authors suggest the spherical morphology for Pd clusters with low metal loading and elliptical shapes for larger metal loads, as J. Schneider and co-workers [34] suggested after their STM analysis of Pd/graphite system catalysts.

In a theoretical work, C. Barreteau et al. [35] demonstrated that for Rh and Pd the icosahedral structure is the preferred at small cluster sizes, and that at a critical size the relative stability becomes favorable to cuboctahedrons. They demonstrated that for 13-atoms Rh and Pd clusters cuboctahedron is unstable, and it spontaneously transfers to an icosahedron. For 55, 147 and 309-atoms clusters the cuboctahedral morphology would be metastable, although the stable phase would still be the icosahedral. It is from 561 and 923-atoms clusters than cuboctahedral morphology would become stable for Pd and Rh respectively. In the case of platinum, Hoare and Pal indicated that a fifty-five atoms cluster would take up an icosahedral structure in preference to face centered cubic cuboctahedral structure [36].

The cluster sizes we have been studying are in the range of 1-8 nm. We have found that platinum clusters acquire cuboctahedral geometry for

4. Superficial Clustering

cluster sizes smaller than 3 nm (≤ 561 -atom). This consideration is in good agreement with theoretical results, because as we could see, cuboctahedral morphologies are allowed in this range [37]. Although 13-atoms cuboctahedral clusters seem to be energetically unstable from theoretical studies, this result does not affect our assumptions, since we could never visualize such small clusters. Platinum cuboctahedral clusters present in our samples are comprised in the size range 1-3 nm (55- 561-atoms). Recently, M.- J. Casanove and co-workers [27], in their analysis using HRTEM and Wide Angle X-ray Scattering (WAXS), demonstrated experimentally the existence of cuboctahedral fcc platinum clusters in such small clusters (55 and 147-atoms). This atomic configuration had also been proposed for 55-atoms Au clusters by Marcus et al. [38] in early 90s.

For diameter sizes bigger than 3 nm (≥ 561 -atoms clusters), the supercell models tested suggest a quasi-spherical morphology. Although for these sizes cuboctahedral geometry is still energetically favorable, the experimental results show that our clusters adopt rounded surfaces. These surfaces are still faceted, but in multiple plan directions leading to a spherical shape.

Both kinds of cluster geometries, cuboctahedral and spherical, have been found to show facets on the interface with the semiconductor oxide. The truncated clusters present a plan surface that allows the cluster to be epitaxed on the support. In the models proposed, the clusters are truncated at more or less $\frac{1}{4}$ of the cluster volume, remaining $\frac{3}{4}$ of the cluster volume morphology. Other works about metal catalysts suggested that metal clusters grew as half cuboctahedrons on the oxide support, as in the case of Rh in TiO_2 and CeO_2 [23, 24]. In our case, profile HRTEM images suggest the $\frac{1}{4}$ models selected.

4.3.4.4 Epitaxy in the Pt/ TiO_2 system

After sample analysis, we have pointed out the existence of two epitaxial relationships: $[1\bar{1}\bar{1}](011)_{\text{Pt}} \parallel [200](052)_{\text{TiO}_2}$ and $[001](020)_{\text{Pt}} \parallel$

$[210](\bar{1}\bar{2}0)_{\text{TiO}_2}$. Although these relationships can be considered representative of some of the sample metal clusters studied in this work, we do not exclude the existence of some others. In the case of similar noble metal / TiO_2 systems, several epitaxial possibilities have been reported. In the case of palladium deposited on titania (110) surface layers, T. Suzuki et al. [39], proposed the $[\bar{1}\bar{2}1](111)_{\text{Pd}} \parallel [001](110)_{\text{TiO}_2}$ relationship. As they found, Pd epitaxed on TiO_2 surface formed islands, in the range 5 – 40 Å. In the case of rhodium loaded on titania nanopowders, S. Bernal and co-workers [40], found the following relationship: $[110](001)_{\text{Rh}} \parallel [010](101)_{\text{TiO}_2}$. Notice that the works mentioned above were carried on with noble metals (Pd and Rh) with similar structural characteristics as platinum (see *table 4.10*), [41, 42, 43]. In this case, it should be reasonable to expect similar results in the case of Pt / TiO_2 .

Noble Metal	a (Å)	S.G.
Pt	3.92	Fm3m (cubic)
Pd	3.89	Fm3m (cubic)
Rh	3.80	Fm3m (cubic)

Table 4.10. Structural characteristics of Pt, Pd and Rh.

In this way, M. Tsujimoto et al. [44], reported in a recent work that Pt clusters presented a $[110](001)_{\text{Pt}} \parallel [001](110)_{\text{TiO}_2}$ epitaxial relationship in their TiO_2 nanopowders. The relationship presented is equivalent to the one suggested previously by Bernal et al. in the case of Rh / TiO_2 system.

However, other authors, as Singh et al. [45] in their work about Rh / TiO_2 , proposed the non-existence of preferred orientations between metal clusters and oxide surfaces.

As we have shown in *Section 4.3.4.4*, it is not possible to determine a clear epitaxial relationship for all the metal clusters found experimentally. We have shown several examples, *figures 4.19, 4.21 and 4.29*, where the epitaxial relationship was not clear. However, the CIS of the models

4. Superficial Clustering

designed had a good resemblance with the experimental images, which makes us think that the models selected were the most appropriated to describe the real systems although non-epitaxial relation had been found.

Nanopowders studied present a wide index variety of faceted surfaces. Since the platinum loaded is distributed homogeneously over all TiO₂ surface, we would expect to find platinum clusters “laying” on titania also for those index surfaces with non-usual indexes. This is the case showed in *figure 4.30*, where the titania surface that supports the platinum is equivalent to a (052) plane. In this case, a further analysis showed that the epitaxy was possible, but in some other cases, as those mentioned above, we could not find any epitaxial relationship. This point will need a further study in the future, in order to establish the percentages of every epitaxial relation. As it has been found in literature, the preferred orientations would be those found by S. Bernal et al. and M. Tsujimoto and co-workers, since {110}_{TiO₂} family planes are the most usual for TiO₂ nanopowders faceting. Anyway the relations found in this work show that some other epitaxial relations can be considered.

4.3.3.5 Metal Nanoclusters versus Macro-Agglomerated Clusters

Although platinum shows a good distribution over titania nanopowders surface as metal nanoclusters, part of the metal loaded remains out of surface as platinum macro-agglomerated clusters (MAC).

Platinum nanoclusters constitute the main part of the Pt involved in catalytic reactions, implied in gas sensing [46, 47, 48, 49] due to its reduced size and high effective area. As shown above and also in previous works [1, 2], the Pt not only nucleates forming small nanoclusters on TiO₂ surface, but it also forms independent MAC with sizes, sometimes, as big as the TiO₂ grains. Since Pt forming MAC has a lower effective area involved in gas reactions, it will be of great interest to reduce its quantity obtaining a higher dispersion of Pt nanoclusters on TiO₂ surface. The determination of the Pt dispersion variation and the differentiation of the Pt/TiO₂ mass ratio

involved in big cluster formation from that involved in Pt nanoclusters embedded on TiO_2 surface, will be the subject of the next *Section*.

4.4 Platinum Dispersion in Titania Samples

Determination of the dispersion state of the supported metal clusters is crucial for the study of their gas sensing properties. Catalytic activities are strongly influenced by the cluster size, homogeneity of distribution and localization (superficial or volumic) [6, 7, 50, 51, 52]. In terms of catalysis, the metal cluster dispersion (D) is defined as the ratio between the number of surface atoms (N_s) and the total number of atoms (N_t). It is important to notice that there is a decreasing of the N_s / N_t relation when increasing the cluster size, as we illustrate in *figure 4.34*, after reading [53]. In the case of the cubic metal clusters shown in *figure 4.34*, metal dispersion decreases dramatically with cluster size. The proportion of surface atoms becomes lower with respect to total cluster atoms when cluster grows. The result obtained is related to the diminution of the cluster specific area in front of their total volume.

In the following, we will study all these characteristics performing the necessary statistical calculus from data obtained experimentally and concluding with an empirical quantitative method.

4.4.1 Mathematical Models and Statistical Parameters

As we have shown in the previous *section*, our clusters adopt cuboctahedral or quasi-spherical shape depending on its diameter size. It will be important to determine the mathematical expressions that can describe the cuboctahedral and quasi-spherical morphologies.

4.4.1.1 Cuboctahedral Model Expressions

For platinum clusters with size diameter in the range 1-3 nm, we have previously determined that they adopt cuboctahedral shape. The distance

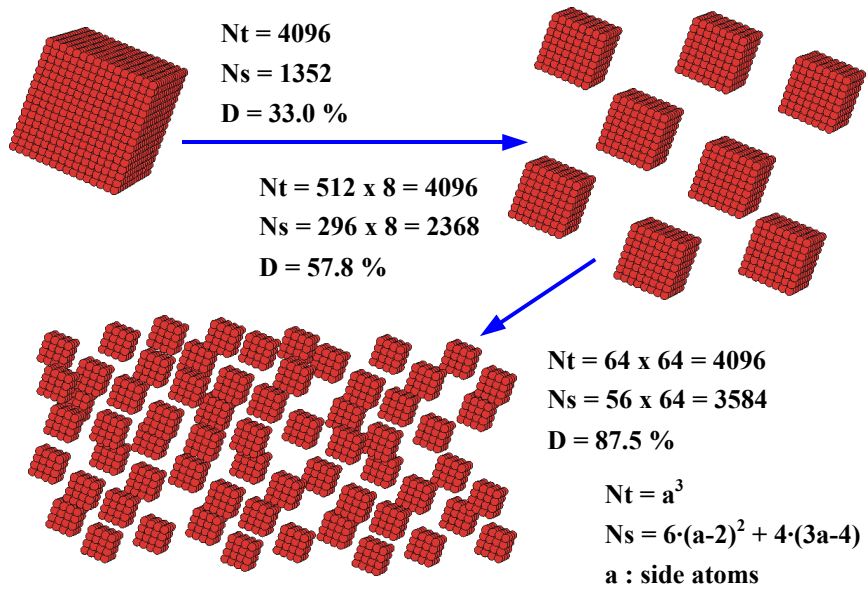


Figure 4.34. Evolution of the N_s/N_t (D) relation for simple cubic metal clusters with cubical morphology. After reading [53].

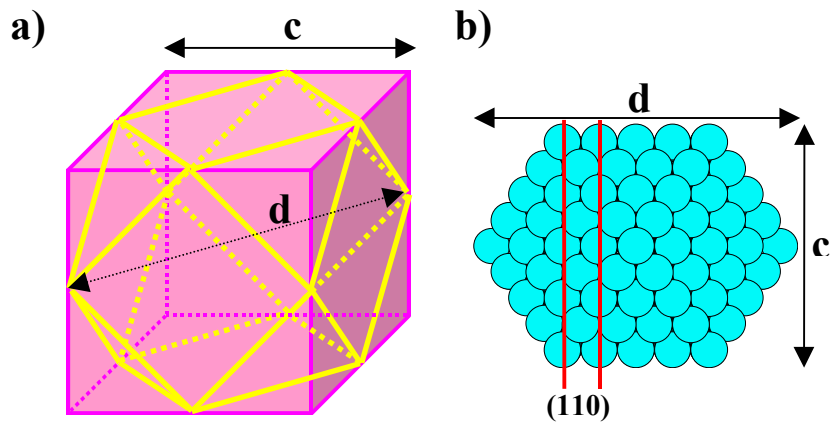


Figure 4.35. (a) Scheme showing a cuboctahedron inserted in a cub. The volume of cuboctahedron can easily be deduced from this picture. In figure (b) we present a Pt cuboctahedral nanocluster of 147 atoms imaged in the [011] orientation, where the cub side, c , is related to the cluster diameter, d , measured by HRTEM images.

4. Superficial Clustering

marked with d on the *figure 4.35* has been used as a measurement of the particle size. In order to evaluate the number of platinum atoms in every cuboctahedral cluster, we will establish a relationship between cluster diameter (d) and the number of atoms on the edges of the (100) faces of the cuboctahedron, K (see *expression 4.2*),

$$d = (3K - 2) d_{110} \quad (4.2)$$

where d_{110} represents the (110) metal lattice spacing, 0.277 nm in the case of platinum. The parameter K has been used in previous works by Martin [54] and Van Hardeveld and Hartog [55] to measure the size of the cuboctahedron metal clusters. In these works, they analyze a wide variety of cluster morphologies (decahedra, icosahedra, cuboctahedra with triangular faces, cuboctahedra with hexagonal faces, etc) concluding that K parameter can be used in all of them indistinctly.

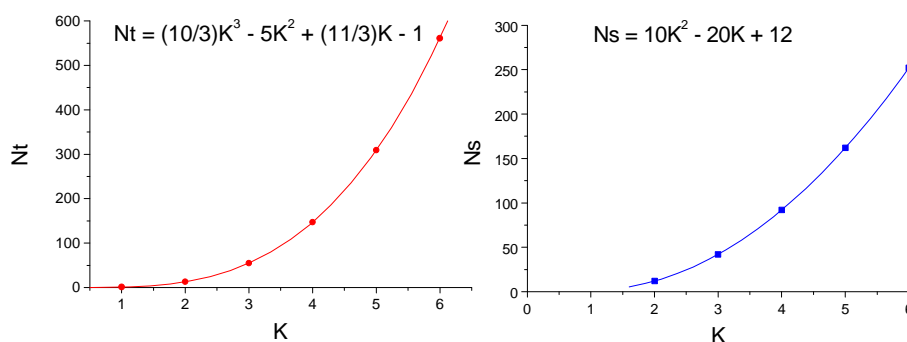


Figure 4.36. Polynomial adjustment for the N_t vs K relation on the left (red curve) and for the N_s vs K on the right (blue curve).

Our clusters have been modeled as cuboctahedrons with triangular faces[♥]. As it is well known, the total number of atoms (N_t) in a cuboctahedron with triangular faces is [54]:

$$N_t = 10/3 K^3 - 5 K^2 + 11/3 K - 1 \quad (4.3)$$

[♥] In the following, when we mention the cuboctahedral morphology we will refer to the cuboctahedron with triangular faces.

The equation shown above can be obtained adjusting a polynomial function of third degree to the well-known magic atomic number sizes that define the cuboctahedral structure (as shown in *figure 4.36*).

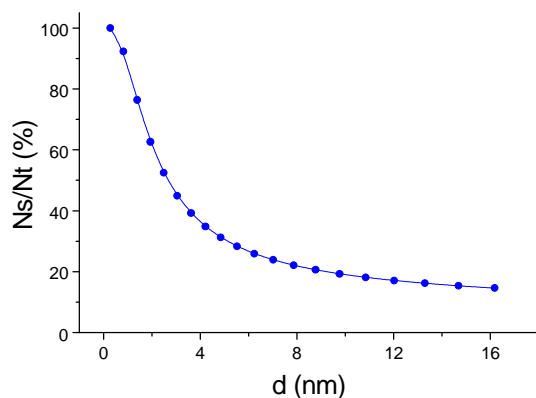


Figure 4.37. N_s/N_t relation in front of cluster size (d). Notice the important decreasing of the dispersion.

We are also interested in the number of surface atoms (N_s) in every cuboctahedral cluster. In this case, we could not find in literature any polynomial expression equivalent to that shown above for the total number of atoms. Van Hardeveld and Hartog obtained a polynomial expression for the N_s of the cuboctahedral clusters, but in this case they referred to the cuboctahedron with hexagonal faces [55]. Anyway, we can trivially obtain the polynomial expression for N_s in the case of cuboctahedron with triangular faces simply adjusting a curve to the number of surface atoms corresponding to the first five magic sizes (see *table 4.11* and *figure 4.36*).

K	d (nm)	N _s	N _t	D (%)
1	0.2772	1	1	100
2	0.8316	12	13	92.3
3	1.386	42	55	76.4
4	1.9404	92	147	62.6
5	2.4948	162	309	52.4
6	3.0492	252	561	44.9

Table 4.11. Correspondence of K with the other parameters of interest.

Notice that we have had to remove data for $K = 1$, when we have fitted the N_s curve. In this first point there is a singularity that do not allow a

4. Superficial Clustering

perfect fitting with a polynomial expression. The final expression calculated for N_s is:

$$N_s = 10 K^2 - 20 K + 12 \quad (\forall K \geq 2) \quad (4.4)$$

With both expressions, N_s and N_t , we can calculate the evolution of metal cluster dispersion ($D = N_s / N_t$) versus cluster size (d) (see *figure 4.37*). As in the case illustrated above (*figure 4.34*) for cubic clusters, there is also an important decreasing of D when increasing the cluster size of the cuboctahedral clusters. The relation of D with metal cluster size was recently widely studied by C. López-Cartes in his *Ph.D. Thesis work* [56]. He found that D values are similar for different cluster morphologies for the same cluster relative size. The morphologies they took in account into their study are widely representative of the experimental results found in literature for metal cluster shapes: octahedron, cube, cuboctahedron with triangular faces, cuboctahedron with hexagonal faces and sphere.

The model cluster proposed in this work corresponds to a cuboctahedron truncated at $\frac{1}{4}$ of the cluster total volume, remaining $\frac{3}{4}$ of the cluster volume. Therefore, the corresponding N_t^* and N_s^* values will be $\frac{3}{4}$ of those described in *expressions 4.3* and *4.4* for a complete cuboctahedron. In the following, the expressions used to evaluate the total and surface cluster atoms will be:

$$N_t^* = 10/4 K^3 - 15/4 K^2 + 11/4 K - 1 \quad (4.5)$$

$$N_s^* = 15/2 K^2 - 15 K + 9 \quad (\forall K \geq 2) \quad (4.6)$$

In order to calculate the volume of a cuboctahedral cluster we will use the Schemes drawn in *figure 4.35*. The scheme shows a cuboctahedron inserted in a cube. From this picture we can easily deduce the cuboctahedron volume as (*equation 4.7*),

$$V_{cuboc} = \frac{5}{6} c^3 \quad (4.7)$$

where c is the side of the cube where cuboctahedron is inserted. In *figure 4.35* we also present a Pt cuboctahedral nanoparticle of 147 atoms, where the cube side, c , is related to the cluster diameter, d , measured by

HRTEM images. The volume of our cuboctahedral clusters will be $\frac{3}{4}$ of the volume showed in *equation 4.7*.

4.4.1.2 Spherical Model Expressions

For platinum clusters with size diameter bigger than 3 nm, the spherical morphology has been assumed. Now, parameter d can be directly defined as the diameter of the sphere. In order to calculate the total number of atoms in the sphere, we will take a different way as the one followed for the cuboctahedral model. In this case, the volume of the sphere can be trivially obtained from the diameter size,

$$V_{esf} = \frac{4}{3}\rho\left(\frac{d}{2}\right)^3 \quad (4.8)$$

Notice that parameter d can be directly obtained from HRTEM or conventional TEM images. Once we obtain the volume of our clusters, their corresponding mass is calculated as shown in *equation 4.9*,

$$M_{esf} = V_{esf} \cdot \rho_{Pt} \quad (4.9)$$

where ρ_{Pt} is the density of platinum in bulk material (21.45 gr/cm³). The total number of atoms of the spherical cluster (N_{t-esf}) can be calculated taking in account the Pt atomic weight,

$$N_{t-esf} = N_A \cdot \frac{M_{esf}}{AW_{Pt}} \quad (4.10)$$

where N_A is the well known *Avogadro's Number* ($6.022 \cdot 10^{23}$ 1/mol) and AW_{Pt} is the platinum atomic weight (195.08 gr/mol). In order to calculate the number of surface atoms in a sphere, we will calculate the volume of the external shell of atoms (V_{shell}), assuming the depth of the external shell as 2.772 Å (r_{shell}), equivalent to the distance between (111)_{Pt} planes,

$$V_{shell} = V_{esf} - \frac{4}{3}\rho\left(\frac{d}{2} - r_{shell}\right)^3 \quad (4.11)$$

4. Superficial Clustering

Once we know the V_{shell} we can calculate the corresponding number of atoms using similar expressions to *equations 4.8* and *4.9*,

$$M_{shell} = V_{shell} \cdot \mathbf{d}_{Pt} \quad (4.12)$$

$$N_{s-esf} = N_{shell} = N_A \cdot \frac{M_{shell}}{AW_{Pt}} \quad (4.13)$$

where, as we have pointed out, the number of surface atoms in the spherical cluster correspond to the number of atoms in the shell.

Notice that the expressions above consider a whole sphere. In order to take in account the real morphology found experimentally we will multiply all the expressions above by the $\frac{3}{4}$ factor.

4.4.1.3 Platinum Nanoclusters Mass Ratio Expressions

Using the expressions shown above, we will discuss the experimental results obtained. We have measured cluster diameter sizes (d) in the experimental HRTEM micrographs obtained for more than 100 Pt clusters in every sample. Once we have these data, we can calculate the total amount of Pt distributed on TiO_2 surface as nanoclusters. We can estimate this Pt/ TiO_2 mass ratio calculating the total volume of Pt embedded on a certain volume of TiO_2 , see *equation 4.14*,

$$\% \frac{Pt_{mass}}{TiO_{2mass}} = R \times \frac{V_{Pt}}{V_{TiO_2}} \times 100 \quad (4.14)$$

where $R (= 5.05)$ is the relation between Pt and TiO_2 bulk densities.

First Order Approximation

The V_{TiO_2} can be easily calculated, measuring the TiO_2 grains diameter from TEM images, and assuming TiO_2 grains as spherical. In the case of V_{Pt} , we take a certain area from a TiO_2 grain and calculate the density of platinum per area unit. We sum the volume of each Pt particle (V_j^{Pt}) inside

that area ($A_x^{TiO_2}$) and divide by two times that area[♦]. The density of platinum per area unit is then calculated in different TiO_2 particles for every sample to check if the Pt mass distribution is homogeneous in all sample regions. In a first approximation, we can assume all Pt nanoclusters as spheres using the diameters calculated from HRTEM micrographs. The volume of the platinum clusters is calculated in this case using the expressions for the spherical model, *equation 4.8**. Assuming the homogeneity of Pt mass distribution, we take the density of platinum per surface unit multiplied by total area of TiO_2 grains (A_{TiO_2}) and divide by the corresponding total volume of these grains (V_{TiO_2}). The total area of TiO_2 grains (A_{TiO_2}) is calculated from the sum of about 100 TiO_2 grain areas ($A_i^{TiO_2}$) to assure a statistical accuracy. Using all these data, we can calculate, in a first order approximation, the mass percent of platinum forming nanoclusters at the TiO_2 grains surface. See *equation 4.15.*,

$$\% \frac{Pt_{mass}}{TiO_2_{mass}} = R \times \frac{\sum_j^m V_j^{Pt}}{2A_x^{TiO_2}} \times \frac{\sum_i^{n \approx 100} A_i^{TiO_2}}{\sum_i^{n \approx 100} V_i^{TiO_2}} \times 100 \quad (4.15)$$

Second Order Approximation

In a second order approximation, we can assume that only the nanoclusters with a diameter bigger than 3 nm should be considered as spherical. We repeat then our calculation, assuming that particles with a diameter (d) less than 3 nm have cuboctahedral morphology, while those

♦ We took in account that the clusters observed can be as well on the upper side as in the back side, since transmitted electrons pass through the matter without giving us information about deepness.

* Just remember that in our model we will reduce the total volume of the sphere in $\frac{1}{4}$ due to the truncation on clusters base.

4. Superficial Clustering

with $d \geq 3$ nm adopt spherical morphology. We apply these changes to *equation 4.20* obtaining the expression shown below, (*equation 4.16*),

$$\% \frac{Pt_{mass}}{TiO_2_{mass}} = R \times \frac{\left(\frac{\sum_j^m V_j^{*Pt} (\forall d_j < 3nm) + \sum_j^m V_j^{Pt} (\forall d_j \geq 3nm)}{2A_x^{TiO_2}} \right) \times \sum_i^{n=100} A_i^{TiO_2}}{\sum_i^{n=100} V_i^{TiO_2}} \times 100 \quad (4.16)$$

where V_j^{Pt} is the volume of a spherical nanocluster with $d \geq 3$ nm (that defined in *equation 4.8* and reduced in $\frac{1}{4}$), and V_j^{*Pt} is the volume of a cuboctahedral nanocluster with $d < 3$ nm (that defined in *equation 4.7* and reduced in $\frac{1}{4}$).

4.4.1.4 Cluster Dispersion Distribution Curves

Using also nanocluster diameter sizes measured from HRTEM micrographs, we can build up different types of distribution curves, as those used in catalysis. S. Bernal and co-workers defined in a recent work [24], three types of distribution curves that can describe perfectly the properties of the cluster dispersion. These distribution curves measure the accumulated percentage of metal clusters vs. cluster size (*type A*), the accumulated percentage of the total number of metal atoms contained in clusters (*type B*) and the fraction of the total number of platinum atoms that are present at the surface of metal clusters (*type C*). In the following, we provide a brief description of these distribution curves [24].

Type A: It accounts for the direct experimental data, i.e. accumulated percentage of metal clusters vs. cluster size (d_k):

$$100 [\sum_i n_i (d_i \leq d_k)] / n_t \text{ vs. } d_k \quad (4.17)$$

where n_i is the number of metal clusters with size d_i and n_t the total number of metal clusters. From this kind of plot, we can estimate the mean platinum cluster size, d_m , and, therefore a metal dispersion value (D_d). D_d

would be defined as the fraction of the total number metal atoms in a cluster with the mean size, d_m , which are exposed at its surface:

$$D_d = N_d(\text{Pt}_s)/N_d(\text{Pt}_t) \quad (4.18)$$

where $N_d(\text{Pt}_s)$ is the number of Pt atoms at the surface of a cluster with the mean size, d_m and $N_d(\text{Pt}_t)$ the total number of atoms in a cluster with the mean size, d_m .

Although the plot shown in *expression 4.17* can be useful to determine the mean cluster size (d_m), we will use conventional histogram diagrams with gaussian adjustments in order to calculate this parameter value.

Type B: It plots the accumulated percentage of the total number of metal atoms contained in clusters with size equal or smaller than a predefined d_k value:

$$100 [\sum_i n_i(\text{Pt}) (d_i \leq d_k)]/n_t \text{ vs. } d_k \quad (4.19)$$

where $n_i(\text{Pt})$ is the number of platinum atoms in clusters with size d_i and $n_t(\text{Pt})$ the total number of metal atoms. This plot can be used as a measure for the mass distribution of platinum.

Type C: It shows the fraction of the total number of platinum atoms that are present at the surface of metal clusters with size equal or smaller than a given d_k value. Therefore, it would account for the contribution to the true metal dispersion (Dm) of the particles with a predefined d_k value or smaller,

$$[\sum_i N_i(\text{Pt}_s)(d_i \leq d_k)]/N_t(\text{Pt}) \text{ vs. } d_k \quad (4.20)$$

where $N_i(\text{Pt}_s)$ is the number of surface platinum atoms in clusters with size d_i and $N_t(\text{Pt})$ the total number of platinum atoms. The last point of the whole distribution curve would measure the metal dispersion of the sample,

$$D_m = [\sum_i n_i(\text{Pt}_s)] / n_t(\text{Pt}) \quad (4.21)$$

In the expressions shown above we will use cuboctahedral or spherical models depending on cluster size in order to calculate total and surface cluster atoms.

4. Superficial Clustering

4.4.2 Statistics on Experimental Results

In this *section* we report the influence of thermal treatment temperature and metal loading percentage on catalytic metal distribution and mean size of both TiO₂ nanopowders and Pt nanoclusters. TEM and HRTEM micrographs have provided us the information about particle sizes and morphologies. As we previously showed, Pt is present in our samples in two different ways: forming Pt nanoclusters embedded on TiO₂ surface (with a size smaller than 8 nm in diameter) or agglomerated forming big Pt clusters not embedded on TiO₂ support (MAC). The distribution of the Pt MAC is not easy to estimate because of its inhomogeneity. However, the Pt nanoclusters' wt.% evaluation is possible thanks to their high homogeneous distribution on TiO₂ surface. We have used a chemical quantitative technique as Inductively Coupled Plasma (ICP) to obtain the total Pt mass proportion versus TiO₂ in our samples. In order to evaluate the Pt wt.% dispersion rate (Pt wt.% involved in each kind of structures), we have developed a simple quantitative method, using HRTEM images information and ICP results. We have also calculated the number of Pt surface nanoclusters per TiO₂ nanoparticle, as well as the Pt atoms shell/surface distribution in these nanoclusters. We will also analyze the distribution plots introduced in the former *section* in order to obtain the metal dispersion parameters.

4.4.2.1 Metal Cluster Dispersion with Thermal Treatment Temperature

In the following, we will analyze the influence of the thermal treatment to our samples. Therefore we will analyze the metal distribution properties of *samples B3, B4 and B5*.

Grain and Cluster Size Distribution

In *figure 4.38*, we illustrate the evolution of TiO₂ grain size when increasing the calcination temperature. Next to TEM micrographs, we present the grain size distribution histograms corresponding to every sample temperature, where more than 100 clusters were measured in every case (see results in *table 4.12*).

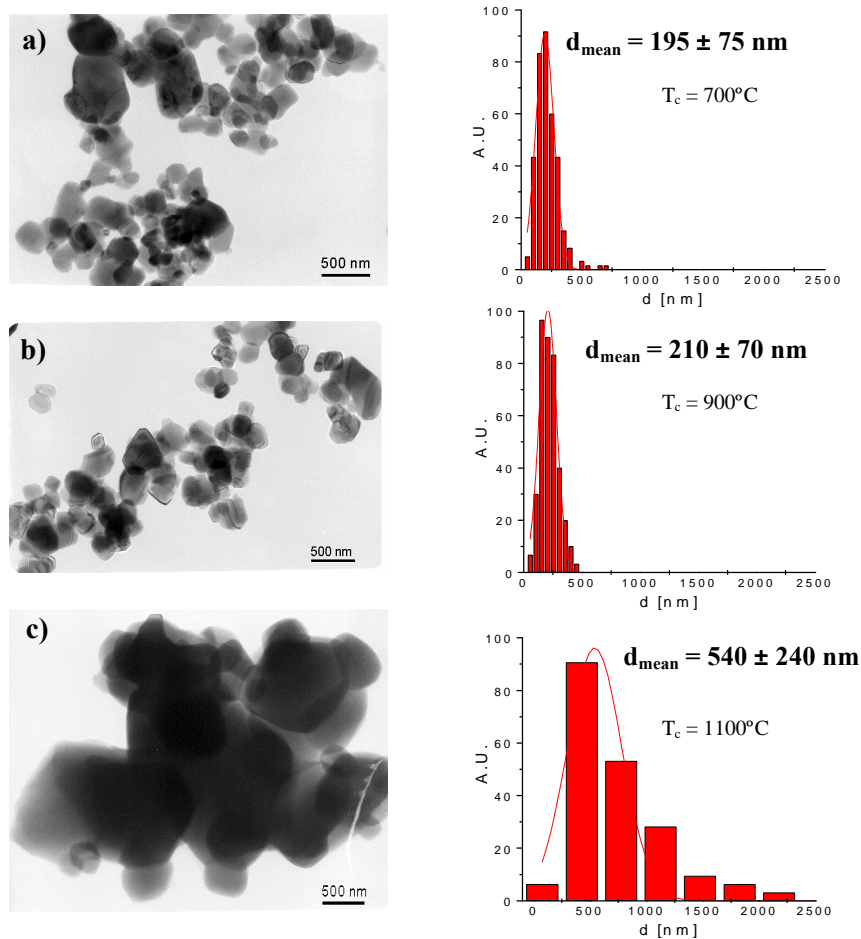


Figure 4.38. The evolution of TiO₂ grain size is observed when increasing the thermal treatment temperature. Temperatures studied correspond to 700, 900 and 1100 °C, (a), (b) and (c) respectively. Next to every TEM micrograph, we present the grain size distribution histograms for each sample.

4. Superficial Clustering

Thermal Treatment temperature (°C)	$d_m^{TiO_2}$ (nm)	d_m^{Pt} (nm)
700	195 ± 75	1.4 ± 0.3
900	210 ± 70	2.2 ± 0.4
1100	540 ± 240	4.4 ± 1.2

Table 4.12. Values calculated from distribution histograms for Pt and TiO₂ nanoclusters and grain mean diameters (d_m) respectively.

There have been just slight changes in grain size distribution when we have treated thermally our samples from 700 to 900 °C, as we have already submitted all our TiO₂ samples to a 900 °C annealing during 4 hours to reach rutile stable phase. However, strong changes occurred when we submitted the sample to 1100 °C, increasing almost 3 times the TiO₂ mean particle size (see d_m values in *table 4.12*).

The next step in our work is to measure the size distribution of the Pt nanoclusters embedded on TiO₂ surface. Platinum clusters morphology has already been determined in previous *sections* from HRTEM images. In *figure 4.39* we show the Pt nanoclusters' size and morphology evolution with thermal treatment temperature (in dark contrast). Next to HRTEM micrographs we also present the respective size distribution histograms, where more than 100 clusters were measured in every case. We have found that Pt nanoclusters size increased with increasing the thermal treatment temperature (results are also shown in *table 4.12*). As we have already demonstrated in a previous *section* with HRTEM analysis, Pt nucleates as cuboctahedral nanoclusters for diameter sizes smaller than 3 nm and in non-regular faceted shapes, which tend to be spherical, for bigger diameter sizes (up to 8 nm). These nanoclusters constitute the main part of the Pt involved in catalytic reactions, implied in gas sensing [7, 47, 48, 49] due to its reduced size and high effective area.

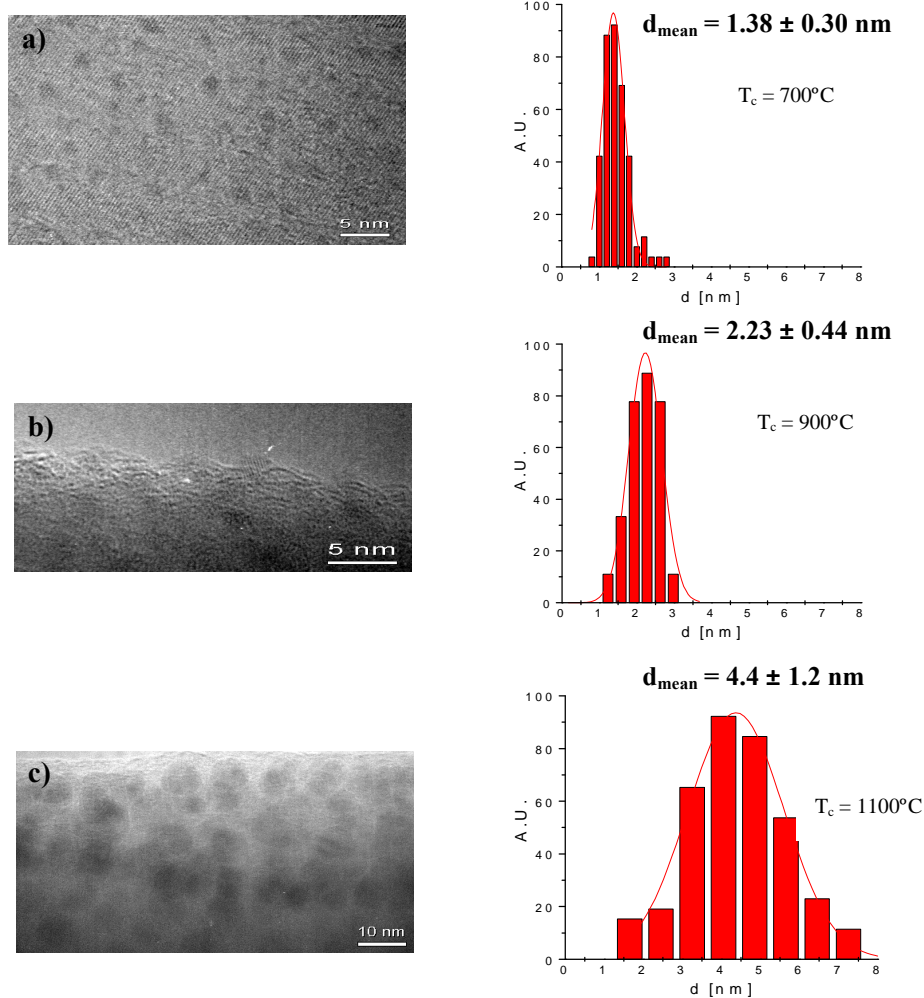


Figure 4.39. We show the Pt nanoclusters' size and morphology evolution with thermal treatment temperature (notice that Pt nanoclusters appear in dark contrast). Samples imaged in figures (a), (b) and (c) correspond to samples submitted to 700, 900 and 1100 °C respectively, (B3, B4 and B5). We measured in every case more than 100 nanoclusters in order to create the size distribution histograms, as those shown next to the HRTEM micrographs.

Platinum Surface Nanoclusters Mass Ratio

As shown also in a previous *section*, Pt nucleates forming nanoclusters on TiO₂ surface as well as independent big clusters (MAC) with sizes, sometimes, as big as the TiO₂ grains. Macro-agglomerated platinum

4. Superficial Clustering

clusters have a lower effective area involved in gas reactions, in this way it will be of great interest to reduce its quantity obtaining a higher dispersion of Pt nanoclusters on TiO₂ surface. To determine the Pt dispersion variation and differentiate the Pt/TiO₂ mass ratio involved in MAC formation from that involved in Pt nanoclusters embedded on TiO₂ surface, we have developed an empirical quantitative method (see *expressions 4.14-4.16*).

As we found in our previous works [1, 2, 14], there is a loss of Pt during the first stages of sample preparation. The amount of platinum remaining in the samples after calcination is evaluated by Inductive Coupled Plasma (ICP). It is indeed 10 to 25% lower than the nominal value (around 5.8 wt.%).

After evaluating the Pt that remained in our samples, we continue our investigation by determining the total amount of Pt distributed on TiO₂ surface as nanoclusters extracting the information from HRTEM images, and using the method described in the former *section (expressions 4.14-4.16)*.

In *figure 4.40*, we compare the mass percents of platinum distributed on TiO₂ surface, calculated using first or second order approximation. Notice that values obtained in both cases are similar for the highest thermal treatment temperature (1100 °C). This happens because at this temperature, the 89.5 % of nanoclusters have diameters bigger than 3 nm and therefore adopt spherical shape.

We have also evaluated the error committed in both, first and second, order approximations as it is shown in *figure 4.40* with the error bars and in *table 4.13*. The error obtained for cuboctahedral volumes comes mainly from the uncertainty in diameter measured from HRTEM images, and it has a value of about 10%. On the other hand, the error committed in the case of spherical approximation is mainly due to the difference between sphere and cuboctahedron volumes, 44 % (see *figure 4.41*). The error in spherical approximation decreases when the particles mean size is over 3 nm, for example in sample submitted to 1100 °C (*B5*). For such a high temperature the main part of nanoclusters has spherical morphology, the same morphology as we take in our first approximation model, so the error is

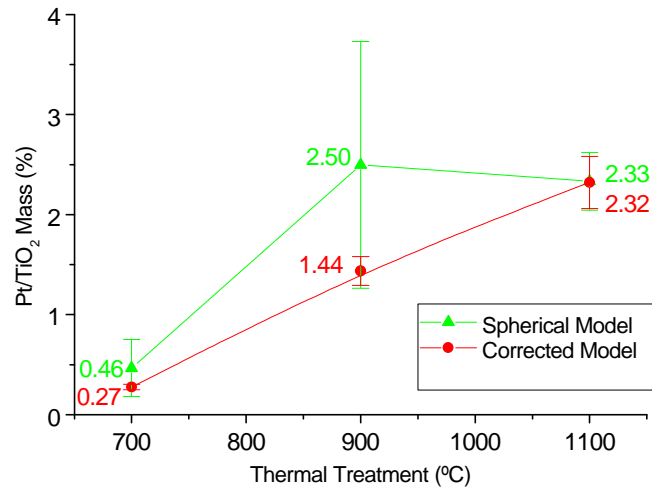


Figure 4.40. Comparison between the Pt/TiO₂ mass % values calculated from TEM and HRTEM micrographs using our empirical method in first (spherical) and second (corrected) order approximations.

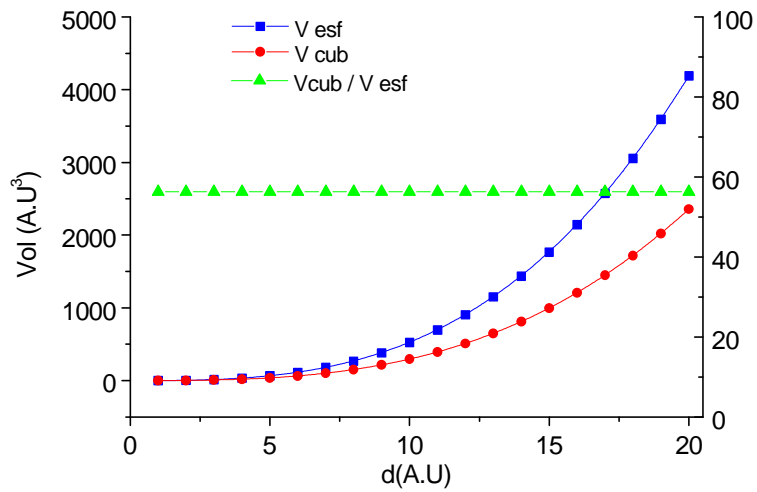


Figure 4.41. Comparison between sphere and cuboctahedron volumes vs. d . V_{cub}/V_{esf} is kept constant with a value of 56.23%. This means that the difference between volumes is equal to 44% of V_{esf} .

4. Superficial Clustering

reduced from 44 % to 11 %. Nevertheless, and according to these error values, we have realized that the spherical approximation was too rough to describe our population and we have taken the results calculated in second order approximation to perform our final analysis of Pt dispersion.

Thermal Treatment temperature (°C)	Pt _{mass over TiO2} wt.% (TEM) 1 st order (spheres)	Pt _{mass over TiO2} wt.% (TEM) 2 nd order (corrected)
700	0.46 ± 0.28	0.27 ± 0.03
900	2.50 ± 1.23	1.43 ± 0.14
1100	2.33 ± 0.29	2.32 ± 0.26

Table 4.13. Pt/TiO₂ mass % calculated using our empirical method in first (spheres) and second (corrected) approximation order.

Evolution of Platinum Distribution

Taking the Pt wt.% mass calculated with ICP as the total platinum mass existing in our samples, we can subtract from these values the ones calculated from HRTEM images in second order approximation and obtain the amount of platinum not included in the nanoclusters (see *figure 4.42* and

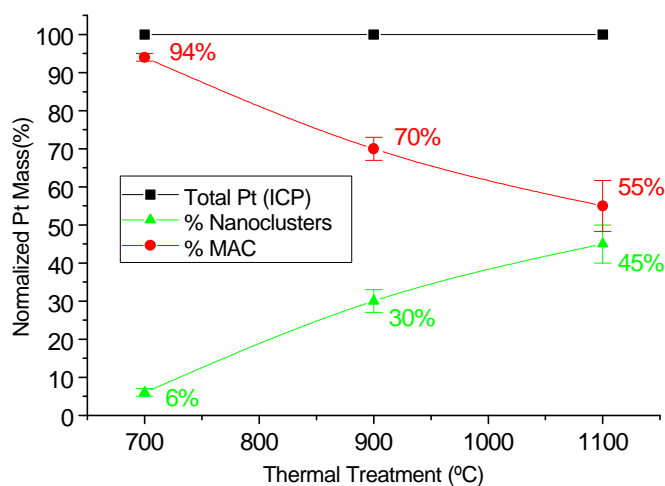


Figure 4.42. Comparison between normalized Pt/TiO₂ wt.% forming nanoclusters with that forming big clusters. Notice that we took as absolute value in all cases, the Pt obtained from ICP results.

table 4.14). Part of this Pt mass could be distributed as dispersed surface atoms or could diffuse inside TiO₂ bulk occupying interstitial places. As it was shown in previous works [14, 57], the mass percent of solute atoms in the case of platinum is negligible, compared with the mass percent included in nanoclusters or MAC. This ratio would not be negligible in the case of other noble metals as Pd, as it was also demonstrated in these previous works [14, 57]. We suggest therefore that the Pt atoms outside the nanoclusters gathered in MAC (see *figure 4.42*).

Thermal Treatment temperature (°C)	Pt Normalized % Mass surface nanoclusters	Pt Normalized % Mass Independent MAC
700	6 ± 1	94 ± 1
900	30 ± 3	70 ± 3
1100	45 ± 5	55 ± 5

Table 4.14. Taking ICP results as absolute values for Pt total mass existing in sample, we present the evolution of the amount of Pt forming nanoparticles respect that forming big clusters.

From results presented in *table 4.14* and illustrated in *figure 4.42*, we deduce that there could exist a migration of Pt from big clusters that feeds and increases the size of the Pt nanoclusters distributed on TiO₂ surface while increasing the thermal treatment temperature. At the same time, these big clusters will lose mass and become smaller. The growth model found is quite more complex than the Ostwald ripening model used to explain precipitate evolution in a semiconductor matrix under annealing, as explained by other authors [58, 59]. Bonafós et al. described the exchange of atoms between precipitates during annealing processes, with the net result that small ones dissolved while the larger precipitates grew [58, 59]. The Pt migration mechanism that we suggest above will be studied and discussed in more detail in following *sections*.

4. Superficial Clustering

Platinum Distribution per TiO₂ Nanograin

Another important parameter involved in gas sensing is the total number of Pt nanoclusters embedded on the surface of every TiO₂ nanograin. We have calculated in every sample the number of nanoclusters in different regions obtaining a mean density of nanoclusters per area unit. With Pt nanoclusters density and the mean TiO₂ nanoparticle area, we obtained the total number of nanoclusters per TiO₂ nanoparticle for each sample; results are shown in *table 4.15* and *figure 4.43*.

Thermal Treatment temperature (°C)	Mean TiO ₂ nanoparticle Area ($\cdot 10^{-9} \text{ cm}^2$)	# Pt nanoclusters per TiO ₂ nanoparticle
700	1.2 ± 0.2	3850 ± 190
900	1.4 ± 0.3	6880 ± 340
1100	9.2 ± 1.8	21340 ± 1060

Table 4.15. Data referred to the total number of Pt nanoclusters embedded on the surface of every TiO₂ nanoparticle and TiO₂ nanoparticles mean area.

The total area of a mean TiO₂ particle has been calculated assuming it as spherical and taking into account the mean TiO₂ diameter obtained from grain size histograms, those showed in *figure 4.38*. We have found that the total number of Pt nanoclusters embedded in every TiO₂ nanoparticle increases dramatically with increasing the treatment temperature. However, we should take into account the evolution of TiO₂ grain size, which can widely modify the surface Pt/TiO₂ mass ratio. In this way, we have obtained that when we increase the temperature, there is an increasing of TiO₂ grain size, reducing dramatically the effective total TiO₂ area. Although the area per TiO₂ grain increases, we have obtained less effective area for the same amount of TiO₂ mass (effective area has an inverse relation with diameter, $\sim 1/d$). Therefore, the quantity of Pt forming Pt nanoclusters on TiO₂ surface has also increased as we have demonstrated above. Both results indicate that

the number of Pt nanoclusters on TiO₂ surface increases with the treatment temperature.

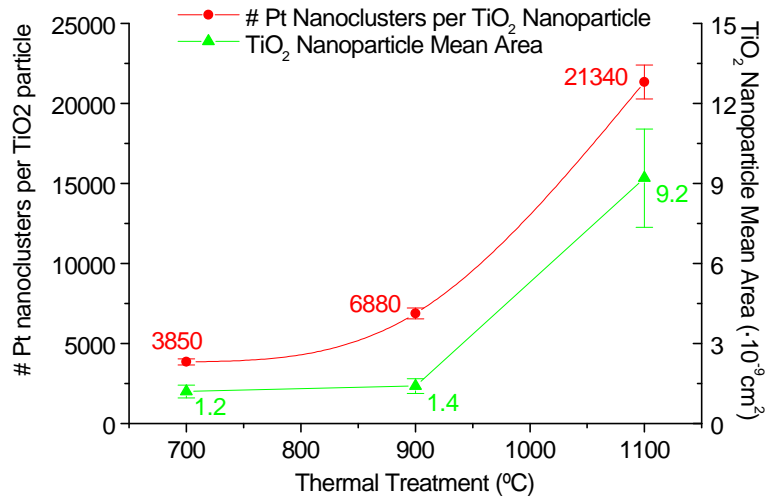


Figure 4.43. Evolution with the treatment temperature of the total number of Pt nanoclusters embedded on the surface of every TiO₂ nanoparticle and the TiO₂ nanoparticle mean area.

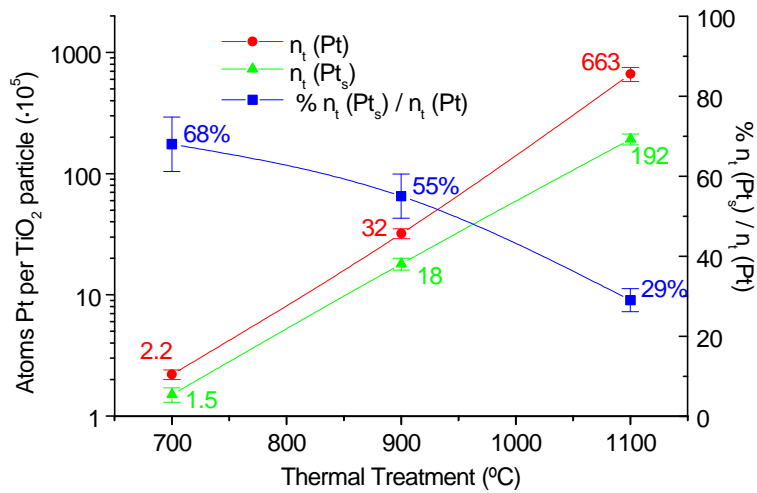


Figure 4.44. The figure shows the number of Pt atoms placed on Pt nanoclusters surface ($n_t(Pt_s)$) per each TiO₂ nanoparticle (active Pt atoms), and also the total Pt atoms ($n_t(Pt)$) per TiO₂ grain (on Pt nanoclusters surface and inside nanoclusters bulk). Notice that these data are shown in logarithmic scale. The ratio of Pt active atoms with respect to the total amount is also present in linear scale.

4. Superficial Clustering

Platinum Dispersion, Catalytic Active Atoms

The quantity of Pt nanoclusters per TiO₂ nanoparticle wouldn't be a parameter to take in account, if we don't calculate also the ratio of Pt catalytic active atoms per TiO₂ grain. We call catalytic active Pt atoms those placed on Pt nanoclusters surface, because these are the ones that interact with gas molecules and participate to the catalytic reactions. As shown in *figure 4.44*, the number of Pt surface atoms ($n_t(Pt_s)$) and the total number of Pt atoms ($n_t(Pt)$) increase when the thermal treatment temperature increases. The important result is not this increase but the ratio of Pt catalytic active atoms with respect to the total Pt atoms per TiO₂ grain, and this ratio decreases with temperature (see results in *table 4.16*). The former *ratio* can be considered as a good measurement of the platinum dispersion.

Thermal Treatment Temperature (°C)	$n_t(Pt_s) (\cdot 10^5)$	$n_t(Pt) (\cdot 10^5)$	$n_t(Pt_s) / n_t(Pt)$ (%)
700	1.5 ± 0.2	2.2 ± 0.2	68 ± 7
900	18 ± 2	32 ± 3	56 ± 6
1100	192 ± 20	663 ± 66	29 ± 3

Table 4.16. Results about the number of Pt atoms placed on Pt nanoclusters surface ($n_t(Pt_s)$) per each TiO₂ nanoparticle (active Pt atoms), and also the total Pt atoms ($n_t(Pt)$) per TiO₂ grain (on Pt nanoclusters surface and inside nanoclusters bulk).

Metal Dispersion Expressions commonly used in Catalysis

In the following we will compare the dispersion results obtained by using our methodology with the standard dispersion calculations used in catalysis. In this way, we use the distribution plots described in *section 4.4.1.4* in order to obtain the metal dispersion in the samples studied (these plots are the ones described by S. Bernal et al. in a recent work [24]). In

figure 4.45 we show the results obtained for these plots. Data corresponding to D_m (metal dispersion) is shown in table 4.17. Notice the coincidence of the results obtained for the ratio $n_i(Pt_s)/n_i(Pt)$ for every TiO_2 particle with those obtained for D_m from metal distribution curves. We have found that both methods show similar results, as the mathematical expressions used in both cases are equivalent. The last result shows that both methods can be complementary used.

Thermal Treatment Temperature (°C)	700	900	1100
D_m (%)	68.4	55.1	29.0

Table 4.17. D_m values obtained from figure 4.45 results.

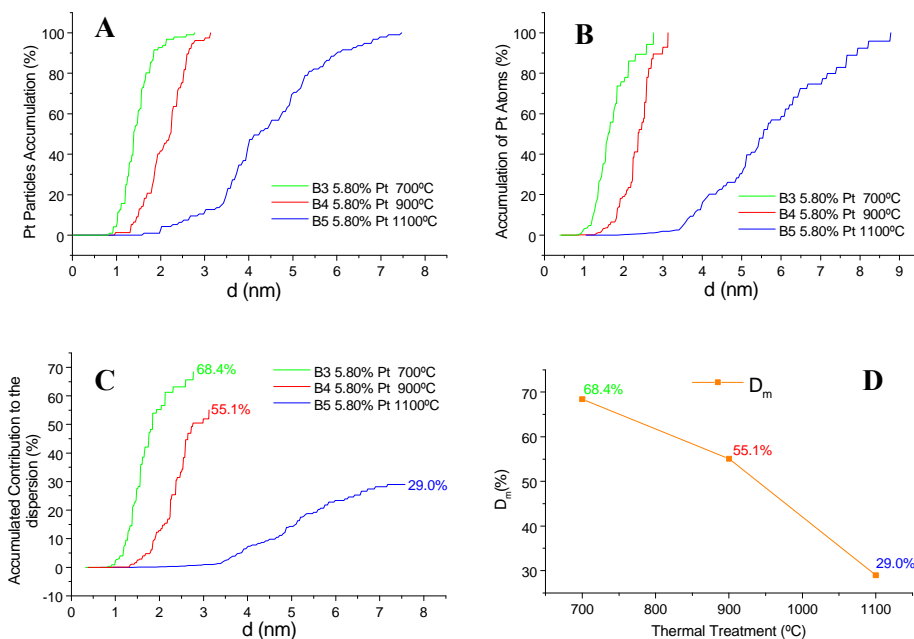


Figure 4.45. Distribution curves (types A-C) corresponding to Pt/TiO₂ samples treated at 700, 900 and 1100 °C. Picture D accounts for the evolution of the metal dispersion (D_m) as function of the Thermal Treatment Temperature.

4. Superficial Clustering

4.4.2.2 Metal Cluster Dispersion with Platinum Loading Percentage

In this *section*, we will analyze the influence of the platinum wt.% loading. Therefore we will analyze the metal distribution properties of *samples B1, B2 and B4*.

Grain and Cluster Size Distribution

In *figure 4.46*, we illustrate the evolution of TiO₂ grain size when increasing the metal loading %. We also show the grain size distribution histograms corresponding to every sample (see results in *table 4.18*).

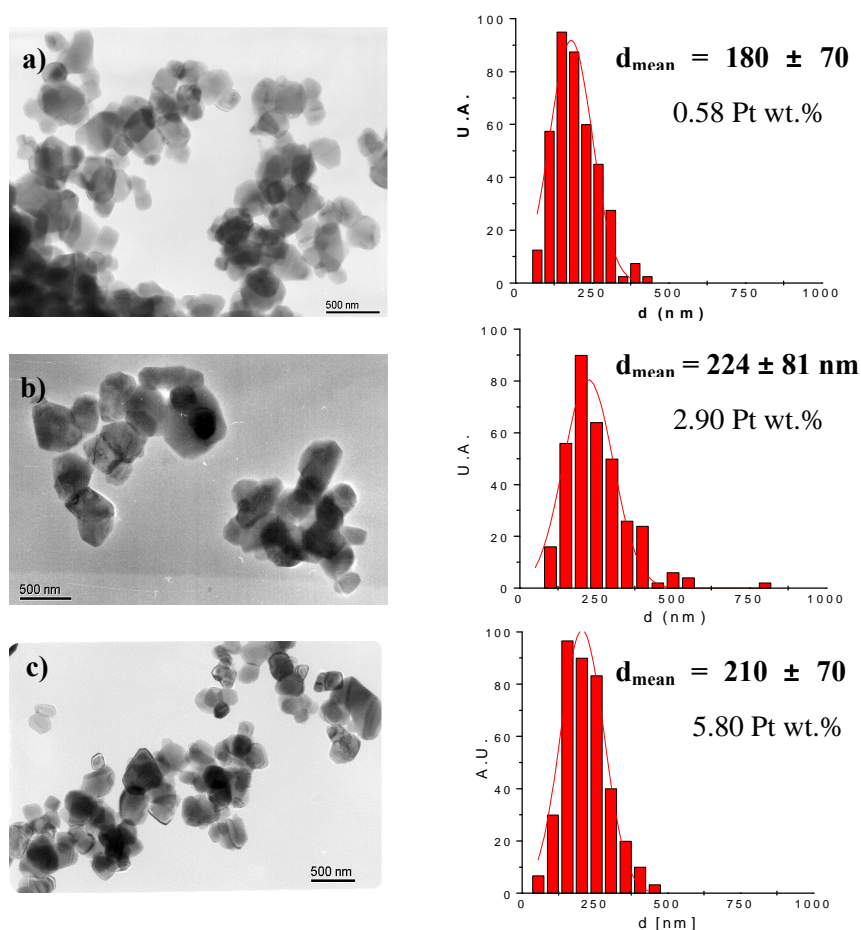


Figure 4.46. The evolution of TiO₂ grain size when increasing the platinum wt.%. Samples studied are *B1, B2 and B4*, (a), (b) and (c) respectively. Next to every TEM micrograph, we present the grain size distribution histograms for each sample.

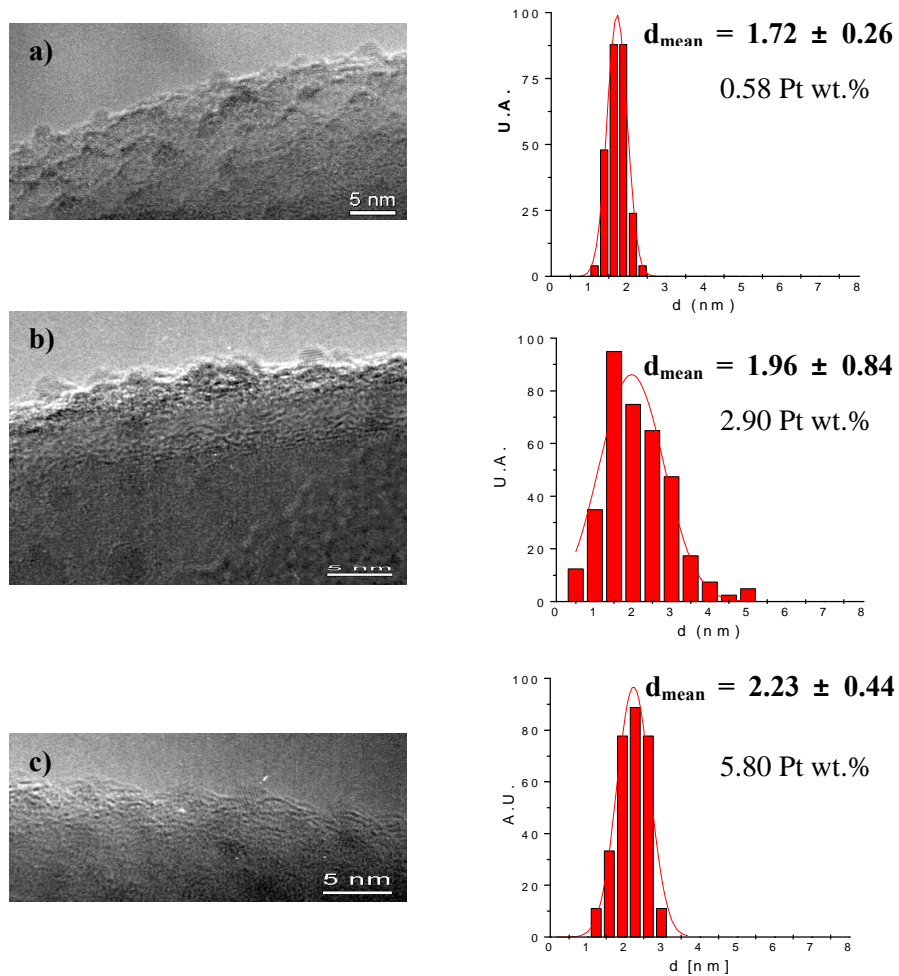


Figure 4.47. We show the Pt nanoclusters' size and morphology evolution with thermal treatment temperature (notice that Pt nanoclusters appear in dark contrast). Samples imaged in figures (a), (b) and (c) correspond to samples submitted with 0.58, 2.90 and 5.80 Pt wt.%, respectively, (B1, B2 and B4). We measured in every case more than 100 nanoclusters in order to create the size distribution histograms, as those shown next to the HRTEM micrographs.

4. Superficial Clustering

Pt wt. %	$d_m^{TiO_2}$ (nm)	d_m^{Pt} (nm)
0.58	180 ± 70	1.7 ± 0.3
2.90	224 ± 81	2.0 ± 0.8
5.80	210 ± 70	2.2 ± 0.4

Table 4.18. Values calculated from distribution histograms for Pt and TiO₂ nanoclusters and grain mean diameters (d_m) respectively.

As we can appreciate, there are just slight changes in TiO₂ grain size distribution when we have changed metal loading from 0.58 to 5.80 Pt wt.%. The differences between TiO₂ grain size values in the different samples have a random variation with Pt wt.% increasing. Moreover its Full width Half Maximum (FWHM) values in statistical distributions are wide enough to consider that there is not an important influence of the platinum amount on TiO₂ grain size.

In *figure 4.47*, we present the Pt nanoclusters size evolution when increasing the metal loading amount. Next to HRTEM micrographs we also present the respective size distribution histograms, as before, more than 100 clusters have been measured in every case (results are also shown in *table 4.18*). In the case of Pt clusters, we have noticed a slight increment in their mean size with increasing the Pt nominal wt.%. The FWHM values in statistical distributions are low for Pt particles mean diameter.

Platinum Surface Nanoclusters Mass Ratio

The amount of platinum evaluated from ICP results is indeed 12 to 18% lower than the nominal values. Suggesting that there is also a loss of Pt during the first stages of sample preparation. Since we have found the platinum mass percent remaining in our samples, we can estimate the Pt/TiO₂ mass ratio using the mathematical expressions shown in the former *section*. In the following, we have omitted the expressions corresponding to the first approximation model considering that they are too rough to describe

the platinum cluster population. In this way we will just present the results calculated in second order approximation.

In *figure 4.48*, we show the mass percents of platinum distributed on TiO₂ surface, calculated using the second order approximation (see also *table 4.19*).

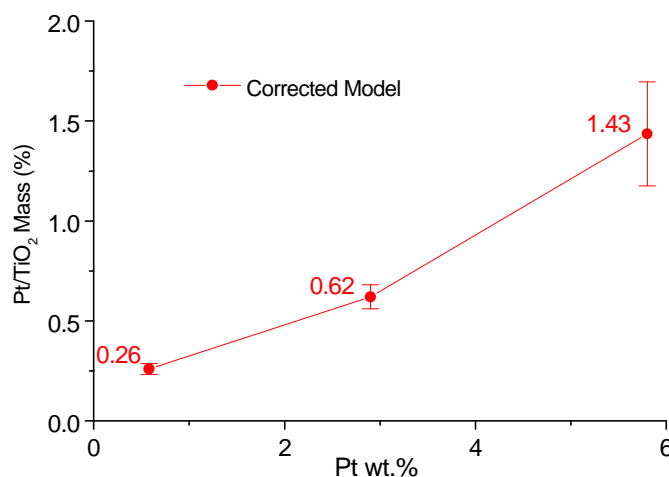


Figure 4.48. Evaluation of the Pt/TiO₂ mass % values calculated from TEM and HRTEM micrographs using our empirical method in second (corrected) order approximation.

Pt wt. %	Pt _{mass over TiO2} wt.% (TEM) 2 nd order
0.58	0.26 ± 0.03
2.90	0.62 ± 0.06
5.80	1.43 ± 0.28

Table 4.19. Pt/TiO₂ mass % calculated using our empirical method in second (corrected) approximation order.

Evolution of Platinum Distribution

Comparison between platinum wt.% forming nanoclusters with respect to the Pt present in MAC is shown in *figure 4.49*. Notice that we have taken the Pt wt. % mass calculated with ICP as the total platinum mass

4. Superficial Clustering

existing in our samples and the rest of results have been normalized to these ICP values. The former results are shown in *table 4.20*.

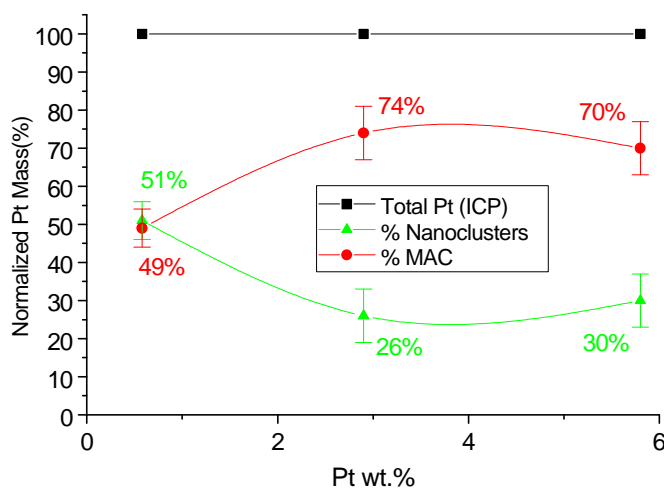


Figure 4.49. Comparison between normalized Pt/TiO₂ wt.% forming nanoclusters with that forming big clusters. Notice that we took as absolute value in all cases, the Pt obtained from ICP results.

Pt wt. %	Pt Normalized % Mass surface nanoclusters	Pt Normalized % Mass Independent MAC
0.58	51 ± 5	49 ± 5
2.90	26 ± 3	74 ± 3
5.80	30 ± 3	70 ± 3

Table 4.20. Taking ICP results as absolute values for Pt total mass existing in sample, we present the evolution of the amount of Pt forming nanoparticles respect that forming big clusters.

The last results show how the Pt wt.% forming nanoclusters remains equal to that agglomerated in MAC, for low Pt loading. However, for higher Pt loadings (beyond 2.9 wt.%), there is a decreasing of the platinum relative percentage that forms nanoclusters, while the amount of Pt included in MAC increases considerably.

Platinum Distribution per TiO₂ Nanograin

We have also estimated the total number of Pt nanoclusters embedded per TiO₂ nanograin and the area of the mean size TiO₂ nanoparticle (table 4.21 and figure 4.50). The mean size TiO₂ particle area remains almost inalterable while the number of platinum clusters increase notably with increasing the Pt percentage loading. The TiO₂ nanoparticles surface area do not experiment important changes, since as we have suggested above, just slight differences have been observed for TiO₂ grain size.

Pt wt. %	Mean TiO ₂ nanoparticle Area ($\cdot 10^{-9} \text{ cm}^2$)	# Pt nanoclusters per TiO ₂ nanoparticle
0.58	1.0 \pm 0.2	2300 \pm 120
2.90	1.6 \pm 0.3	3390 \pm 170
5.80	1.4 \pm 0.3	6880 \pm 340

Table 4.21. Data referred to the total number of Pt nanoclusters embedded on the surface of every TiO₂ nanoparticle and TiO₂ nanoparticles mean area.

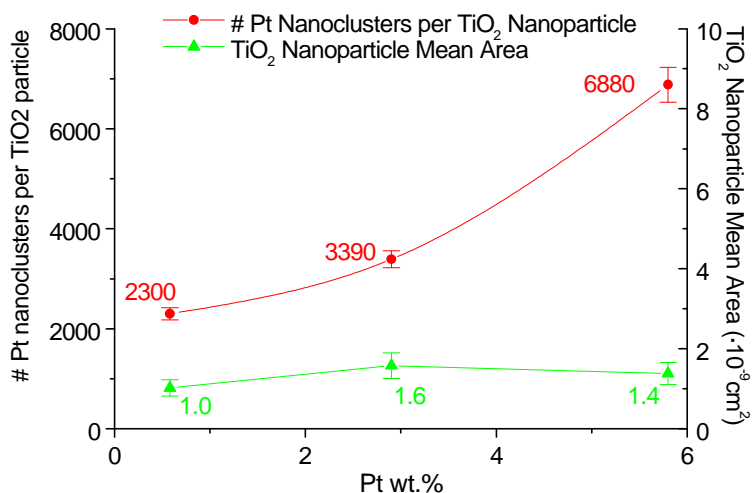


Figure 4.50. Evolution with the treatment temperature of the total number of Pt nanoclusters embedded on the surface of every TiO₂ nanoparticle and the TiO₂ nanoparticle mean area.

4. Superficial Clustering

Platinum Dispersion, Catalytic Active Atoms

When we increase the platinum loading percentage, as shown in *figure 4.51*, the number of Pt surface atoms ($n_t (Pt_s)$) and the total number of Pt atoms ($n_t (Pt)$) increase. This result is obvious taking in account that the amount of Pt present in our system is increasing. However, it is important to notice that the ratio of Pt catalytic active atoms with respect to the total Pt atoms per TiO_2 grain decreases with Pt loading (*table 4.22*). The inflexion point found for middle loadings will be discussed in the following *section*.

Pt wt. %	$n_t (Pt_s) (\cdot 10^5)$	$n_t (Pt) (\cdot 10^5)$	$n_t (Pt_s) / n_t (Pt)$ (%)
0.58	1.3 ± 0.2	1.9 ± 0.2	70 ± 7
2.90	4.5 ± 0.5	9.7 ± 1.0	47 ± 5
5.80	23 ± 2	43 ± 4	55 ± 6

Table 4.22. Results about the number of Pt atoms placed on Pt nanoclusters surface ($n_t (Pt_s)$) per each TiO_2 nanoparticle (active Pt atoms), and also the total Pt atoms ($n_t (Pt)$) per TiO_2 grain (on Pt nanoclusters surface and inside nanoclusters bulk). The ratio of Pt active atoms with respect to the total amount is also present.

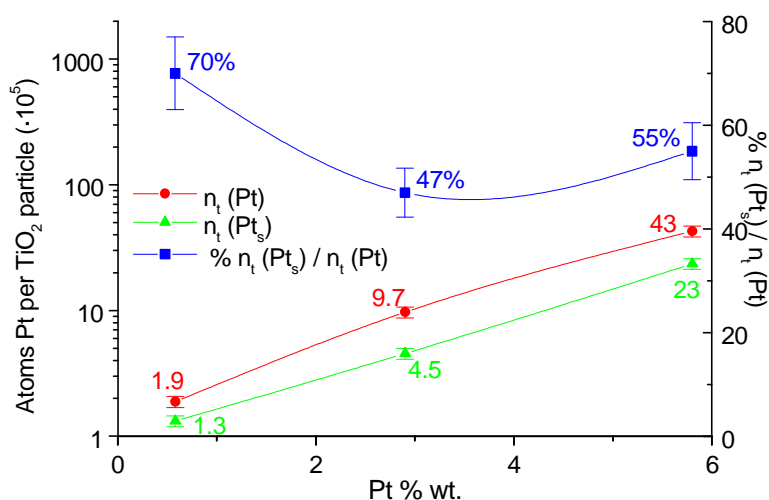


Figure 4.51. The figure shows the number of Pt atoms placed on Pt nanoclusters surface ($n_t (Pt_s)$) per each TiO_2 nanoparticle (active Pt atoms), and also the total Pt atoms ($n_t (Pt)$) per TiO_2 grain (on Pt nanoclusters surface and inside nanoclusters bulk). Notice that these data are shown in logarithmic scale. The ratio of Pt active atoms with respect to the total amount is also present in linear scale.

Metal Dispersion Expressions commonly used in Catalysis

The distribution plots described in *section 4.4.1.4* for metal dispersion analysis are also achieved for these samples (see *figure 4.52* and *table 4.23*). The D_m (metal dispersion) parameter shows also an inflexion point for middle loading values. In the same way, the rest of plots also show a non-expected behavior of the 2.9 Pt wt.% sample. Notice that the D_m values calculated using the common expressions used in catalysis also reproduce the results obtained before.

Pt wt. %	0.58	2.90	5.80
D_m (%)	66.3	47.0	55.1

Table 4.23. D_m values are obtained from *figure 4.52* results.

The next *section* it has been devoted to discuss all the statistical results shown until now.

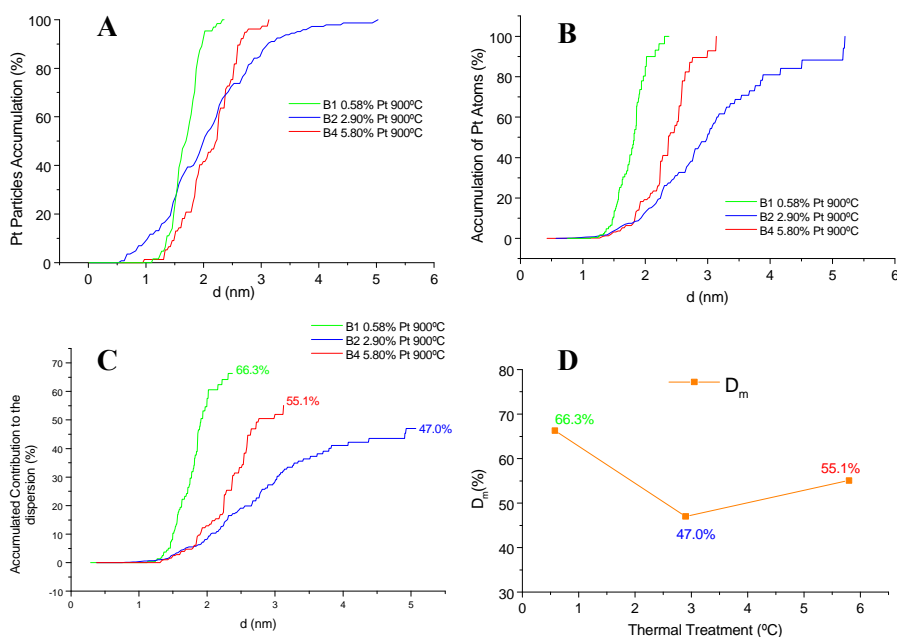


Figure 4.52. Distribution curves (types A-C) corresponding to *B1*, *B2* and *B4* Pt/TiO₂ samples. Picture D accounts for the evolution of the metal dispersion (D_m) as function of the Thermal Treatment Temperature.

4.4.3 Discussion on Dispersion Analysis

Evaluation of the different experimental and calculated results obtained in this work allows us to select the a priori best sample for gas-sensing devices. We will consider the results found for both analyses, evolution of the metal dispersion with temperature and loading percentage, in order to determine the best sample preparation parameters.

4.4.3.1 Influence of the Thermal Treatment

On one hand, we have found that at high treatment temperatures the amount of Pt placed on TiO₂ surface is bigger although Pt is distributed in a low catalytic effective way (big clusters with less effective area). On the other hand, for low temperatures, the Pt is not mainly placed on TiO₂ surface, although the less numerous Pt clusters are highly active in gas reactions due to their reduced size and high effective area. Therefore, we should reach a compromise between the amount of Pt on TiO₂ surface forming nanoclusters, nanoclusters size (related to the Pt active atoms ratio) and quantity of these nanoclusters per TiO₂ grain. Taking in account the former considerations, the best sample for gas sensing would be that obtained at medium treatment temperature (~ 900 °C). Plots shown in *figure 4.45*, also suggest that the best metal dispersion lies on the samples with lower treatment temperatures, while in the sample treated at the higher temperature the platinum dispersion falls down dramatically. From the former results the last sample should not be considered in order to implement a SGS device. The election for the best candidate should be done taking in account the samples treated at lower temperatures, 700 and 900 °C respectively. In both cases the noble metal dispersion is acceptable, > 50 %, meaning than more than 50 % of the metal atoms forming the clusters are catalytically active. Comparing the results obtained for both, we can suggest that the a priori best sample is the one treated at 900 °C, for the reasons

commented above, higher Pt mass percentage forming clusters, and bigger number of clusters per TiO₂ nanograin.

4.4.3.2 Influence of the Metal Loading Percentage

As a general result we have found that Pt wt.% increases with increasing the noble metal loading. This is in good agreement with the results expected. There are many reasons to select the *sample B4* powders as the best candidates in order to implement a SGS device. Firstly, the sample has been treated at the optimum temperature, as shown in the former *section*. Secondly, the metal loading percentage used is the one that presents better properties. At such platinum percentage, the number of surface nanoclusters per TiO₂ nanograin is the highest. Moreover, although 70% of the platinum loaded is included in MAC, the percentage of platinum remaining in surface clusters is also higher with respect to the samples with lower loadings. Furthermore, another parameter to take in account is the high dispersion of the platinum on the sample, > 50 %, meaning that the main part of the Pt atoms forming surface nanoclusters are catalytically active.

It is interesting to discuss the results obtained for *sample B2*. In this case, the D_m (metal dispersion) parameter shows an inflexion point for this loading value. This effect is not expected for such a loading percentage. We should expect a gradual decreasing of the metal dispersion when increasing the metal loading, due to the slight increase of the platinum nanoclusters size. The strong variation shown for *sample B2* can be explained for the presence of wide distribution of nanocluster sizes. If we observe the size distribution histogram for *sample B2* nanoclusters in *figure 4.47.b*, we can notice the high wideness of the FWHM in comparison with the rest of sample histograms. The HRTEM analysis performed to the sample, as shown in *figure 4.18*, evidences the existence of platinum surface clusters with sizes bigger than those expected at this loading percentage. The presence of such a big platinum clusters is responsible of the important fall of the dispersion value. We suggest that in this case, an anomaly could happen during sample preparation, leading to this non-uniformity of platinum dispersion evolution. Nevertheless, the aim of this work is not the

4. Superficial Clustering

improvement of technology, but the use of effective analytical tools in order to evaluate the samples characteristics and properties.

In the former discussion we have suggested that the best sample found from the ones studied is that with the higher platinum loading. One could think that the more loading percentage, better results obtained. This is not completely true, because when a higher amount of metal is loaded to the sample, the cluster sizes become bigger, and eventually merge when metal reaches a critical percentage. In this point it can be almost said that a thin layer of metal covers the support particles, as suggested by Dickinson et al. in their study of Pd growth over TiO₂ substrates [60]. We have estimated the critical nominal platinum percentage necessary for the merge of the platinum clusters. At this point we would obtain close conduction circuits through metal clusters losing the sensing characteristics of our SGS device. In this way, we have found an expression depending on the metal loading percentage that shows the evolution of the metal covering on TiO₂ surface (*figure 4.53*). Thus, in general terms, the function produce the correct approximate shape for the loading dependence. It is not intended that this be a quantitative fit since several factors have been ignored in this treatment and some assumptions have been performed. These factors and assumptions are:

- (i) We assume that our platinum clusters adopt quasi-spherical shapes.
- (ii) We consider that the area occupied for a cluster is the corresponding to the central circumference included in the sphere determined for the mean diameter.
- (iii) We assume that TiO₂ nanoparticles mean area value is not influenced by the metal loading percentage. We have taken a mean area value of $1.4 \cdot 10^{-9} \text{ cm}^2$.
- (iv) As a consequence of the preceding assumptions the particles all touch (merge) at exactly the same loading, at which point function mean TiO₂ nanoparticles area coincides with the sum of the areas of all nanoclusters included in titania nanograin.

- (v) For $N(x)$ and $d(x)$ fittings we have used the experimental points obtained in our samples. Three points are not enough in a precise fitting, but as we wanted to obtain an approximated result, it will be enough in our case.

We could include all these factors mathematically, but we would then have too many floating parameters, such that a very good fit to the data would be obtained, but from which little additional information would be derived.

The final function considered is shown below,

$$f(x) = N(x) * 4p \left(\frac{d(x)}{2} \right)^2 - A \tag{4.22}$$

where $f(x)$ is the corresponding function model depending on x (nominal Pt wt.%). $N(x)$ is the number of platinum nanoclusters per TiO_2 nanograin. $d(x)$ is the platinum clusters mean diameter. And finally A is the mean area of a TiO_2 nanograin assumed as constant. Solving $f(x)$ we will

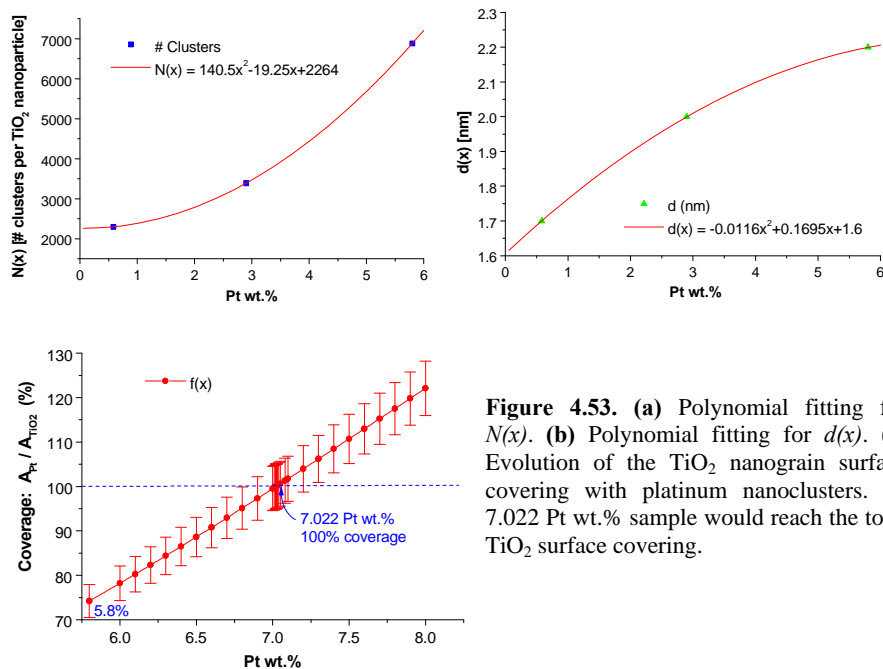


Figure 4.53. (a) Polynomial fitting for $N(x)$. (b) Polynomial fitting for $d(x)$. (c) Evolution of the TiO_2 nanograin surface covering with platinum nanoclusters. At 7.022 Pt wt.% sample would reach the total TiO_2 surface covering.

4. Superficial Clustering

obtain the platinum loading percentage for which TiO₂ nanograins surface is totally covered by platinum.

In *figure 4.53.a* we have adjusted a second order polynomial function to the $N(x)$ evolution, obtaining,

$$N(x) = 140.5x^2 - 19.25x + 2264 \quad (4.23)$$

In *figure 4.53.b*, the adjustment have been made for the $d(x)$ relation,

$$d(x) = -0.0116x^2 + 0.1695x + 1.60 \quad (4.24)$$

Finally, in *figure 4.53.c*, we present the evolution of the TiO₂ surface percentage covered by Pt clusters with metal loading increasing. As the solution obtained (7.02 ± 0.35 Pt wt.%) is not so far away from the points used for $N(x)$ and $d(x)$ fittings, we can consider that the result obtained can be considered as a good approximation.

4.4.3.3 Noble Metal Growing Modes on Semiconductor Oxide Support

Attending to the results obtained experimentally, we have found that the growing mode of the platinum loaded in our TiO₂ samples is purely three-dimensional. Platinum clusters follow the Volmer-Weber mechanism, leading to the formation of individual three-dimensional islands (clusters), describing a three-dimensional growth, where nanoclusters nucleate on surface [61].

The results found are in good agreement with those obtained by Suzuki et al. and Petsy et al. In both works, they suggested a Volmer-Weber three-dimensional growth of the Pt clusters on semiconductor support [39, 62]. In general, the more reactive the metal is towards oxygen, the more two-dimensional is the initial growth [63, 64, 65]. In the case of platinum, its low reactivity towards oxygen would suggest this 3-D growing behavior.

Mainly all authors agree with the pure three-dimensional growing mode for Pt and Pd, although this opinion is not completely unanimous so there are some authors that prefer to suggest a mixed 2D/3D model. In this way, Evans et al. [66] said that Palladium particle growth on TiO₂(110) showed similarities to Cu deposited on TiO₂(110) which grows by a Stranski-Krastanov growth and produces the Cu(111) face parallel to the

surface and aligned with the substrate unit cell. It is necessary to mention that the different growth techniques used in order to obtain the metallic deposition can dramatically influence in the posterior metal disposition due to their special characteristics.

What it is clear is that thermodynamics take an important part in metal growth. Nanocrystal shapes of clusters deposited on semiconductor supports have size-dependent energy minima that result from the interplay between strain relaxation at the facets and stress concentration at the edges [67]. In general, kinetic limitations, in the form of low surface diffusivities or high deposition rates, can roughen a film that is energetically favored to be flat or lead to the formation of many small islands (clusters) for a system in which the thermodynamically stable configuration is a single large crystallite sitting on the substrate. In the latter case, the islands are only metastable; as the growth proceeds, the smallest ones dissolve as the relatively larger ones grow. This process is known as Ostwald ripening or coarsening because both the average island size and the width of the size distribution increase with time as the density decreases [67].

However, in our case, we have to take into account other factors to the Ostwald ripening effect. In *section 4.4.2.1*, we made a complete description of the material behavior under thermal treatment. We deduced that there was a migration of Pt from big clusters that feed and increased the size of the Pt nanoclusters distributed on TiO₂ surface while increasing the thermal treatment temperature. This fact means that to the Ostwald ripening effect we should add the platinum migration from big clusters to nanoclusters placed on TiO₂ surface. In this way, the growth model found is quite more complex than the Ostwald ripening model used to explain precipitate evolution in a semiconductor matrix under annealing [58, 59]. Moreover, we should also take into account that the effective area of TiO₂ nanograins dramatically decreases due to the high increase of TiO₂ grain size. This means that even if the platinum surface percentage were kept constant, we would appreciate an increasing of nanoclusters density and size due to effective support-surface reduction. All these factors have a strong

4. Superficial Clustering

influence over platinum nanoclusters behavior in the Pt/TiO₂ system. There are too many variables in order to perform a physical model that offers good results when studying thermal treatment sample evolution. Nevertheless, it was possible to obtain a quantitative mathematical approximation that explains the platinum dispersion evolution when increasing the noble metal loading, as shown in the former *section* (see *expressions 4.22-4.24*). The model found is in good agreement with that proposed recently by Gaidi et al. [68], for Pt/SnO₂ systems. In that work, they proposed that in an initial situation, where the metal clusters are very small (mean sizes smaller than 2 nm for 3% Pt concentration), the number and size both increase up to a maximum density value from which they saturate. In their case, for Pt concentration higher than 8%, the density is kept constant, nucleation sites are all occupied and the additional Pt atoms agglomerate to already existing particles, making them bigger. In our case, the platinum clusters evolve growing in size and number for all examples. However, it has also been found that the cases analyzed have a platinum percentage lower than that considered by Gaidi et al. as the maximum value from which they saturate. This maximum value depends strongly on the semiconductor surface total area available, as this parameter is related with the number of nucleation sites. In our case, and according to our calculations made in the former *section*, the maximum density value obtained has a value of approximately 7%.

4.4.3.4 Decrease of Platinum Mass Concentration vs. Nominal Value

In all samples there was a slight decrease of Pt total mass compared with nominal value. This variation was also reported in some of our previous works [1, 2], and it is indeed 10 to 25% of the nominal value depending on the sample studied. We should point out that Pt is introduced in sample by platinum chloride impregnation, as PtCl₄:

On one hand, PtCl₄ compounds can be easily hydrolyzed. This fact could make us estimate an erroneous Pt nominal mass, since the precursor mass measured would include H₂O molecules not taken into account in our

calculus. This could be the cause of the lower Pt total mass obtained by ICP with respect to that calculated for the nominal value.

On the other hand, catalysts prepared using metal chloride salts or complexes present Cl centers all over sensing material before thermal treatment [69]. During calcination process, Pt precipitates over TiO_2 surface in metallic phase, while Cl is evaporated. We suggest that part of this Pt could be also evaporated during calcination in a chloride or oxide form, explaining the slight variation of platinum in samples [70]. This last point is supported on the catalysis literature, normally sceptic to the use of Pt chlorides due to the volatility of the PtCl_2 compounds, which is easily detected in the cold parts of the calcination systems used [71].

However, it is not clear yet if the variation of platinum atoms is due to PtCl_2 evaporation, to some other platinum oxide compounds evaporation or to the precursor hydrolyzation.

What it is clear is that there is a mass variation in the precursor with respect to the nominal value, and that some other introduction methods could be tried out in order to improve and control the efficiency of platinum introduction. A good possibility could be the use of platinum nitrides or other complexes instead of chlorides to avoid the possible evaporation or the use of a previously dried up precursor. Nevertheless, the results obtained in our samples, such as good Pt nanocluster dispersion and high percentage of metal active atoms suggest that we have widely reached the objectives proposed.

4.5. Conclusions

In this *Chapter* we have analyzed the properties of the superficial metal clustering in SGS nanopowders, taking as an example the platinum loaded on TiO₂ by the impregnation method. The investigation has included the analysis of the Pt structure and morphology performing a rigorous TEM analysis, and a complete statistical study of the noble metal dispersion. The main conclusions obtained will be reported in the following:

We have obtained that the main part of TiO₂ nanopowders has adopted the TiO₂ rutile stable phase after thermal treatment. The anatase phase was rarely found in TiO₂ nanoparticles when using HRTEM. TiO₂ rutile peaks appear clearly in XRD spectra and there is not data that referred to the anatase phase. Results obtained suggest that the thermal treatment used to stabilize our TiO₂ samples in the rutile stable phase has been highly effective. Moreover, Pt loading seems not to affect phase transition temperatures.

The effects of grinding process in our samples have had different influence depending on the position in which it was applied, before or after thermal treatment. On one hand, when grinding was applied to the last step of the preparation (*set A samples*), TiO₂ nanograins showed irregular faceted borders at low magnification, whereas those nanometric grains exhibited a polycrystalline structure under higher magnifications. The grinding process is shown to break small parts of the original TiO₂ particles creating the facets observed while the snatched crystals may be stucked to the bigger particles surface. On the other hand, the application of grinding before the final thermal treatment (*set B samples*) allowed us to obtain quasi-spherical TiO₂ nanoparticles with defined borders. Higher magnifications showed monocrystalline TiO₂ nanograins.

Platinum nucleated as cuboctahedral nanoclusters for diameter sizes smaller than 3 nm (cuboctahedrons with triangular and square faces) and in non-regular faceted shapes, which tended to be spherical, for bigger diameter sizes (≥ 3 nm, ≥ 561 -atoms clusters). Those morphologies were found independently of the grinding process (before or after sample stabilization), although configuration for *set A* made difficult the statistics. Moreover, both geometries, cuboctahedral and spherical, have been found to show facets on the interface with the semiconductor oxide. In the models proposed, the clusters were truncated at more or less $\frac{1}{4}$ of the cluster volume, remaining $\frac{3}{4}$ of the cluster volume morphology.

We have pointed out the existence of two epitaxial relationships: $[11\bar{1}](011)_{\text{Pt}} \parallel [200](052)_{\text{TiO}_2}$ and $[001](020)_{\text{Pt}} \parallel [210](\bar{1}20)_{\text{TiO}_2}$. Although these relationships can be considered representative of some of the sample metal clusters studied in this work, we do not exclude the existence of some others.

Although platinum shows a good distribution over titania nanopowders surface as metal nanoclusters, part of the metal loaded remains out of surface as platinum macro-agglomerated clusters (MAC). These MAC can be as big as TiO_2 grains decreasing the platinum effective area involved in gas reactions. An empirical quantitative method has been developed in order to determine the Pt dispersion variation and differentiate the Pt/ TiO_2 mass ratio involved in big cluster formation from that involved in Pt nanoclusters embedded on TiO_2 surface.

We found that in order to select the a priori best sample for SGS implementation, we should reach a compromise between the amount of Pt on TiO_2 surface forming nanoclusters, nanoclusters size (related to the Pt active atoms ratio) and quantity of these nanoclusters per TiO_2 grain. Taking in account the former considerations, the best sample for gas sensing would be that obtained at medium treatment temperature (~ 900 °C).

Surface Platinum wt.% increases with increasing the noble metal loading. *Sample B4* (with 5.8 nominal Pt wt.%) has been selected as the best candidates in order to implement a SGS device. Firstly, the sample has been

4. Superficial Clustering

treated at the optimum temperature (900°C). Secondly, the metal loading percentage used presents the highest number of surface nanoclusters per TiO₂ grain, moreover, although 70% of the platinum loaded is included in MAC, the percentage of platinum remaining in surface clusters is also higher with respect to the samples with lower loadings. Furthermore, dispersion of the platinum on the sample is > 50 %.

We have estimated the critical nominal platinum percentage necessary for the merge of the platinum clusters on TiO₂ particles surface. The percentage corresponds to 7.02 ± 0.35 Pt wt.%. For loading values close to the calculated, the electronic transport in our sensor would be mainly through metal clusters losing the sensing characteristics of our device.

The growing mode of the platinum loaded in our TiO₂ samples is purely three-dimensional. Platinum clusters follow the Volmer-Weber mechanism, leading to the formation of individual three-dimensional clusters, describing a three-dimensional growth.

A variation of platinum mass with respect to the nominal mass value during first stages of the preparation method has been reported. Nevertheless, the results obtained in our samples, such as good Pt nanocluster dispersion and high percentage of metal active atoms suggest that we have widely reached the objectives proposed.

Equally, we have demonstrated that the nanoscopic methods applied for the analysis (HRTEM), data processing (DIP) and corroboration of the obtained results through the structural models simulation (CIS), are indispensable if we want to perform a rigorous study of our SGS materials sensing characteristics at the atomic level.

References

1. J. Arbiol, A. Ruiz, A. Cirera, F. Peiró, A. Cornet, J. R. Morante, A. Alimoussa and M.- J. Casanove, Analysis of Pt-Nanoparticles Embedded on Crystalline TiO₂ studied by Transmission Electron Microscopy, *MRS FALL 2000 Proceedings*, Boston (2000).
2. J. Arbiol, A. Ruiz, A. Cirera, F. Peiró, A. Cornet, J. R. Morante, A. Alimoussa and M.- J. Casanove, Platinum nanoclusters dispersion in TiO₂ nanopowders, submitted to *Journal of Materials Research*.
3. U. Kirner, K. D. Schierbaum, W. Göpel, B. Leibold, N. Nicoloso, W. Weppner, D. Fischer and W. F. Chu, Low and High Temperature TiO₂ Oxygen Sensors, *Sensors and Actuators B*, **1**, 103-107 (1990).
4. H. Lin, The study of oxygen spillover and back spillover on Pt/TiO₂ by a potential dynamic sweep method, *Journal of Molecular Catalysis A: Chemical*, **144**, 189–197 (1999).
5. J. Sheng, N. Yoshida, J. Karasawa and T. Fukami, Platinum doped titania film oxygen sensor integrated with temperature compensating thermistor, *Sensors and Actuators B*, **41**, 131-136 (1997).
6. M. Englisch, A. Jentys and J. A. Lercher, Structure Sensitivity of the Hydrogenation of Crotonaldehyde over Pt/SiO₂ and Pt/TiO₂, *Journal of Catalysis*, **166**, 25–35 (1997).
7. Y. Zhu, L. Zhang, W. Yao and L. Cao, The chemical states and properties of doped TiO₂ film photocatalyst prepared using the Sol-Gel method with TiCl₄ as a precursor, *Applied Surface Science*, **158**, 32–37 (2000).
8. J. R. McBride, G. W. Graham, C. R. Peters and W. H. Weber, Growth and characterization of reactively sputtered thin-film platinum oxides, *Journal of Applied Physics*, **69** (3), 1596-1604 (1991).
9. *JCPDS*, 43-1100 (1997).
10. Andrew D. Polli, T. Wagner, T. Gemming and M. Rühle, Growth of platinum on TiO₂- and SrO₂-terminated SrTiO₃(100), *Surface Science*, **448**, 279-289 (2000).

4. Superficial Clustering

11. J. Arbiol, F. Peiró, A. Cornet, K. Michelakis i A. Georgakilas. Temperature-graded InAlAs buffers applied on InGaAs/InAlAs/InP high electron mobility transistor heterostructures, *Journal of Vacuum Science and Technology B*, **17(6)**, 2540-2544 (1999).
12. J. Arbiol, F. Peiró, A. Cornet i A. Christou, Growth characterisation of InAlAs/InGaAs structures on InP non_(001) index substrates, *Inst. Phys. Conf. Ser.* **164**, 193-196, (1999).
13. M. Tsujimoto, S. Moriguchi, S. Isoda, T. Kobayashi and T. Komatsu, TEM analysis of Pt-particles embedded on TiO₂ exhibiting high photocatalytic activity, *Journal of Electron Microscopy*, **48 (4)**, 361-366 (1999).
14. A. Cabot, J. Arbiol, J. R. Morante, U. Weimar, N. Bârsan and W. Göpel, Analysis of the noble metal catalytic additives introduced by impregnation of as obtained SnO₂ sol-gel nanocrystals for gas sensors, *Sensors and Actuators B*, **70**, 87-100 (2000).
15. *JCPDS*, 21-1276 (1997).
16. G. Cerrato, L. Marchese and C. Morterra, Structural and morphological modifications of sintering microcrystalline TiO₂: an XRD, HRTEM and FTIR study, *Applied Surface Science*, **70/71**, 200-205 (1993).
17. Y. G. Borodko, L. Ioffe, T. Halachev, P. Bosch, A. Cuan, I. N. Ivleva and Y. M. Shulga, Interaction of Pt/TiO₂ samples with H₂ and O₂: magnetic and structural properties, *Materials Chemistry and Physics*, **58**, 199-203 (1999).
18. A. Diéguez, Structural Analysis for the improvement of SnO₂-Based Gas Sensors, *PhD. Thesis*, Universitat de Barcelona, Barcelona (1999).
19. T. D. Shen, C. C. Koch, T. L. McCormick, R. J. Nemanich, J. Y. Huang and J. G. Hunag, The structure and property characteristics of amorphous/nanocrystalline silicon produced by ball milling, *Journal of Materials Research*, **10 (1)**, 139-148 (1995).
20. J. Z. Jiang, R. Lin, S. Morup, K. Nielsen, F. W. Poulsen, F. J. Berry and R. Clasen, Mechanical alloying of an immiscible α -Fe₂O₃-SnO₂ ceramic, *Physical Review B*, **55 (1)**, 11-14 (1997).
21. T. D. Shen, I. Shmagin, R. M. Kolbas, Y. Fahmy, L. Bergman, R. J. Nemanich, M. T. McClure, Z. Sitar and M. X. Quan, Photoluminescence from mechanically milled Si and SiO₂ powders, *Physical Review B*, **55 (12)**, 7615-7623 (1997).
22. J.- O. Malm and M. A. O'keefe, Deceptive "lattice spacings" in high-resolution micrographs of metal nanoparticles, *Ultramicroscopy*, **68**, 13-23 (1997).

23. S. Bernal, F. J. Botana, J. J. Calvino, C. López, J. A. Pérez-Omil and J. M. Rodríguez-Izquierdo, High-resolution electron microscopy investigation of metal-support interactions in Rh/TiO₂, *Journal of the Chemical Society, Faraday Trans.*, **92 (15)**, 2799-2809 (1996).
24. S. Bernal, J. J. Calvino, M. A. Cauqui, J. A. Pérez Omil, J. M. Pintado and J. M. Rodríguez-Izquierdo, Image simulation and experimental HREM study of the metal dispersion in Rh/CeO₂ catalysts. Influence of the reduction/reoxidation conditions, *Applied Catalysis B: Environmental*, **16**, 127-138 (1998).
25. M. Flueli, Thesis No 769, Ecole Polytechnique Federale de Lausanne, Switzerland (1989).
26. F. Dassenoy, Nanoparticules mono- et bi-metalliques a base de platine, cobalt et ruthenium. Etude structurale par microscopie electronique a haute resolution et diffusion des rayons X aux grans angles, *Ph.D. Thesis*, Université Paul Sabatier, Toulouse (1999).
27. M.- J. Casanove, P. Lecante, E. Snoeck, A. Mosset and C. Roucau, HREM and WAXS Study of the Structure of Metallic Nanoparticles, *Journal of Physics III France*, **7**, 505-515 (1997).
28. S. Ino, Stability of multiply twinned particles, *Journal of the Physical Society Jpn*, **27**, 941 (1969).
29. L. D. Marks, Surface structure and energetics of multiply twinned particles, *Philosophical Magazine A*, **49**, 81 (1984).
30. A. Howie and L. D. Marks, Elastic strains and the energy balance for multiply twinned particles, *Philosophical Magazine A*, **49**, 95 (1984).
31. K. Ebitani, Y. Fujie and K. Kaneda, Immobilization of a Ligand-Preserved Giant Palladium Cluster on a Metal Oxide Surface and Its Nobel Heterogeneous Catalysis for Oxidation of Allylic Alcohols in the Presence of Molecular Oxygen, *Langmuir*, **15**, 3557-3562 (1999).
32. P.- A. Buffat, M. Flüeli, R. Sopycher, P. Stadelmenn and J.- P. Borel, Crystallographic Structure of Small Gold Particles studied by High-resolution Electron Microscopy, *Faraday Discussions*, **92**, 173-187 (1991).
33. S. Giorgio, C. Chapon, C. R. Henry, G. Mihoul and J. M. Penisson, High-resolution transmission electron microscopy study of gold particles (greater than 1 nm), epitaxially grown on clean MgO microtubes, *Philosophical Magazine A*, **64**, 87-96 (1991).

4. Superficial Clustering

34. J. Schneider, C. Wambach, B. Pennemann and K. Wandelt, Scanning Tunneling Microscopy and Scanning Tunneling Spectroscopy Studies of Powdery Palladium/Graphite Model Catalysts, *Langmuir*, **15**, 5765-5772 (1999).
35. C. Barreteau, M. C. Desjonquères and D. Spanjaard, Theoretical study of the icosahedral to cuboctahedral structural transitions in Rh and Pd clusters, *The European Physical Journal D*, **11**, 395-402 (2000).
36. M. R. Hoare and P. Pal, Statistics and stabilization of small assemblies of atoms, *Journal of Crystal Growth*, **17**, 77-96 (1972).
37. P. L. Gai, M. J. Goringe and J. C. Barry, HREM image contrast from supported small metal particles, *Journal of Microscopy*, **142**, 9-24 (1986).
38. M. A. Marcus, M. P. Andrews and J. Zegenhagen, Structure and vibrations of chemically produced Au₅₅ clusters, *Physical Review B*, **42**, 3312 (1990).
39. T. Suzuki and R. Souda, The encapsulation of Pd by the supporting TiO₂ (110) surface induced by strong metal-support interactions, *Surface Science*, **448**, 33-39 (2000).
40. S. Bernal, F. J. Botana, J. J. Calvino, C. López, J. A. Pérez-Omil and J. M. Rodríguez-Izquierdo, High-resolution electron microscopy investigation of metal-support interactions in Rh/TiO₂, *Journal of the Chemical Society, Faraday Trans.*, **92 (15)**, 2799-2809 (1996).
41. *JCPDS*, 04-0802 (1997).
42. *JCPDS*, 34-1101 (1997).
43. C. Boudias and D. Monceau, *CARINE 3.1 Data Basis*, (1989-1998).
44. M. Tsujimoto, S. Moriguchi, S. Isoda, T. Kobayashi and T. Komatsu, TEM analysis of Pt-particles embedded on TiO₂ exhibiting high photocatalytic activity, *Journal of Electron Microscopy*, **48 (4)**, 361-366 (1999).
45. A. K. Singh, N. K. Pande and A. T. Bell, *Journal of Catalysis*, **94**, 422 (1985).
46. Y. Zhu, L. Zhang, W. Yao and L. Cao, The chemical states and properties of doped TiO₂ film photocatalyst prepared using the Sol-Gel method with TiCl₄ as a precursor, *Applied Surface Science*, **158**, 32-37 (2000).
47. J. C. Kennedy III and A. K. Datye, Photothermal Heterogeneous Oxidation of Ethanol over Pt/TiO₂, *Journal of Catalysis* **179**, 375-389 (1998).
48. I. Hayakawaa, Y. Iwamotoa, K. Kikutab and S. Hiranob, Gas sensing properties of platinum dispersed-TiO₂ thin film derived from precursor, *Sensors and Actuators B*, **62**, 55-60 (2000).

49. P. J. Collier, J. A. Iggo and R. Whyman, Preparation and characterization of solvent-stabilized nanoparticulate platinum and palladium and their catalytic behavior towards the enantioselective hydrogenation of ethyl pyruvate, *Journal of Molecular Catalysis A: Chemical*, **146**, 149-157 (1999).
50. B. J. Kip, F. B. M. Duivenvoorden, D. C. Koningsberger and R. Prins, Determination of Metal Particle Size of Highly Dispersed Rh, Ir, and Pt Catalysts by Hydrogen Chemisorption and EXAFS, *Journal of Catalysis*, **105**, 26-38 (1987).
51. K. Ebitani, Y. Fujie and K. Kaneda, Immobilization of a Ligand-Preserved Giant Palladium Cluster on a Metal Oxide Surface and Its Nobel Heterogeneous Catalysis for Oxidation of Allylic Alcohols in the Presence of Molecular Oxygen, *Langmuir*, **15**, 3557-3562 (1999).
52. R. Ukropec, B. F. M. Kuster, J. C. Schouten and R. A. van Santen, Low temperature oxidation of ammonia to nitrogen in liquid phase, *Applied Catalysis B: Environmental*, **23**, 45-57 (1999).
53. G. Schmid (Ed.), Clusters and Colloids: From Theory to Applications, *VCH*, Weinheim (1994).
54. T. P. Martin, Shells of atoms, *Physics Reports*, **273**, 199-241 (1996).
55. R. Van Hardeveld and F. Hartog, The Statistics of Surface Atoms and Surface Sites on Metal Crystals, *Surface Science*, **15**, 189-230 (1969).
56. C. López-Cartes, Aspectos Nanoestructurales de los Fenómenos de Interacción Metal-Soporte en los Catalizadores Modelo Metal/Óxido de Cerio, *PhD. Thesis*, Universidad de Cádiz, (2000).
57. M. H. Madhusudhana Reddy and A. N. Chandorkar, E-Beam deposited SnO₂, Pt-SnO₂ and Pd-Sno thin films for LPG detection, *Thin Solid Films*, **349**, 260-265 (1999).
58. C. Bonafos, B. Garrido, M. Lopez, A. Perez-Rodriguez, J. R. Morante, Y. Khin, G. Ben Assayag and A. Claverie, An electron microscopy study of the growth of Ge nanoparticles in SiO₂, *Applied Physics Letters*, **76 (26)**, 3962-3964 (2000).
59. C. Bonafos, B. Colombeau, A. Altibelli, M. Carrada, G. Ben Assayag, B. Garrido, M. Lopez, A. Perez-Rodriguez, J. R. Morante and A. Claverie, Kinetic study of group IV nanoparticles ion beam synthesized in SiO₂, E-MRS Strasbourg (2000), invited paper, to be published in NIMB.
60. A. Dickinson, D. James, N. Perkins, T. Cassidy and M. Bowker, The photocatalytic reforming of methanol, *Journal of Molecular Catalysis A: Chemical*, **146**, 211-221 (1999).

4. Superficial Clustering

61. B. Joyce, Self-organization yields quantum-dot devices, *Vacuum Solutions*, **17**, 11-14 (2000).
62. F. Petsy, H-P. Steinrück and T. E. Madey, Thermal stability of Pt films on TiO₂(110): evidence for encapsulation, *Surface Science*, **339**, 83-95 (1995).
63. J.- M. Pan, B. L. Maschhoff, U. Diebold and T. E. Madey, Structural study of ultrathin metal films on TiO₂ using LEED, ARXPS and MEED, *Surface Science*, **291**, 381-394 (1993).
64. U. Diebold, J.-M. Pan and T. E. Madey, Growth mode of ultrathin copper overlayers on TiO₂(110), *Physical Review B*, **47 (7)**, 3868-3876 (1993).
65. J.- M. Pan and T. E. Madey, Ultrathin Fe films on TiO₂(110): Growth and reactivity, *Journal of Vacuum Science and Technology A*, **11(4)**, 1667-1674 (1993).
66. J. Evans, B.E. Hayden and G. Lu, The adsorption of carbon monoxide on TiO₂(110) supported palladium, *Surface Science*, **360**, 61-73 (1996).
67. G. Medeiros-Ribero, A. M. Bratkovski, T. I. Kamins, D. A. A. Douglas and R. S. Williams, Shape Transition of Germanium Nanocrystals on silicon (001) Surface from Pyramids to Domes, *Science*, **279**, 353-355 (1998).
68. M. Gaidi, J. L. Hazemann, I. Matko, B. Chenevier, M. Romyantseva, A. Gaskov and M. Labeau, Role of Pt Aggregates in Pt/SnO₂ Thin Films Used as Gas Sensors Investigations of the Catalytic Effect, *Journal of The Electrochemical Society*, **147 (8)**, 3131-3138 (2000).
69. J. Soria, A. Martínez-Arias, J. C. Conesa, G. Munuera and A. R. González-Elipé, Effect of chlorine impurities on the properties of CeO₂, *Surface Science*, **251/252**, 990-994 (1991).
70. A. Cabot, A. Diéguez, A. Romano-Rodríguez, J. R. Morante and N. Bàrsan, Influence of the catalytic introduction procedure on the nano-SnO₂ gas sensor performances. Where and how stay the catalytic atoms?, *In press Sensors and Actuators B*.
71. K. Fogger and H. Jaeger, The Effect of Chlorine Treatment on the Dispersion of Platinum Metal Particles Supported on Silica and γ -Alumina, *Journal of Catalysis*, **92**, 64-78 (1985).

